



저작자표시-비영리-변경금지 2.0 대한민국

이용자는 아래의 조건을 따르는 경우에 한하여 자유롭게

- 이 저작물을 복제, 배포, 전송, 전시, 공연 및 방송할 수 있습니다.

다음과 같은 조건을 따라야 합니다:



저작자표시. 귀하는 원저작자를 표시하여야 합니다.



비영리. 귀하는 이 저작물을 영리 목적으로 이용할 수 없습니다.



변경금지. 귀하는 이 저작물을 개작, 변형 또는 가공할 수 없습니다.

- 귀하는, 이 저작물의 재이용이나 배포의 경우, 이 저작물에 적용된 이용허락조건을 명확하게 나타내어야 합니다.
- 저작권자로부터 별도의 허가를 받으면 이러한 조건들은 적용되지 않습니다.

저작권법에 따른 이용자의 권리는 위의 내용에 의하여 영향을 받지 않습니다.

이것은 [이용허락규약\(Legal Code\)](#)을 이해하기 쉽게 요약한 것입니다.

[Disclaimer](#)

공학박사 학위논문

직류 마이크로그리드에서 고품질 전력  
기반 분산전원 전력분배

**A Study on Power Sharing Techniques with  
Enhanced Power Quality in DC Microgrid**

울산대학교 대학원

전기공학부

DAM DUY HUNG

공학박사 학위논문

직류 마이크로그리드에서 고품질 전력  
기반 분산전원 전력분배

**A Study on Power Sharing Techniques with  
Enhanced Power Quality in DC Microgrid**

지도교수 이흥희

이 논문을 공학박사 학위논문으로 제출함

2019년 12월

울산대학교 대학원

전기공학부

DAM DUY HUNG



DAM DUY HUNG 의 공학박사 학위논문을 인준함

심사위원장

전태원



심사위원

이흥희



심사위원

최성진



심사위원

이동춘



심사위원

정의현



울산대학교 대학원

2019년 12월



UNIVERSITY OF ULSAN

# **A Study on Power Sharing Techniques with Enhanced Power Quality in DC Microgrid**

by

DAM DUY HUNG

Supervisor: Professor Hong-Hee Lee

A dissertation  
submitted in partial fulfillment  
for the degree of Doctor of Philosophy  
in  
School of Electrical Engineering  
University of Ulsan

December, 2019

This certifies that the doctoral dissertation of DAM DUY HUNG is approved by:

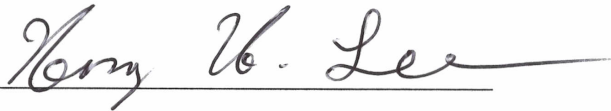
1. Committee Chair: **Professor Tae-Won Chun**

Signature:



2. Committee Member: **Professor Hong-Hee Lee**

Signature:



3. Committee Member: **Professor Sung-Jin Choi**

Signature:



4. Committee Member: **Professor Dong-Choon Lee**

Signature:



5. Committee Member: **Doctor Eui-Heon Jung**

Signature:



School of Electrical Engineering

University of Ulsan

Ulsan, Korea

December, 2019

*... to my father, Dam Van Hoe, who passed away  
before he was able to see this dissertation completion ...*

# Abstract

Recently, DC microgrid receives more attention in these days as it has no issues with reactive power flow and frequency regulation, which results in a notably less complex in control system. As droop control method is used to cooperate with various type of sources in microgrid, the DC bus voltage is swing according to the load power. Moreover, the line impedance affects the power sharing among distributed generations (DGs) in the system. In DC microgrid, there are many renewable energy resources, and their output power strictly depend on the resource condition. In order to utilize the DG sources effectively in DC microgrid, many kinds of power management methods are developed to improve the power quality and achieve accurate power sharing for DG microgrid system. In this thesis, the power sharing with enhanced power quality is studied for DC Microgrid based on the battery energy storage system including the supercapacitor (SC).

Firstly, this thesis introduces a new power distributed control method for a DC microgrid. This method is developed to share the load power proportionally to the rating of DG and restore the DC bus voltage when the load changes. For this purpose, a shifted voltage technique is developed based on the power rating and the instantaneous power of DGs. By adding the shifted voltage, the voltage drop caused by the droop controller is effectively compensated so that the DC bus voltage is constantly regulated regardless of the load change. To realize the proposed method, all the required information to determine the reference voltage is transmitted through a low-bandwidth communication link. The controller design process is presented in detail along with a system stability analysis in this thesis.

Secondly, this thesis presents a new control method for SC to compensate the transient for the DG in DC microgrid. The SC unit is controlled by modeling the SC as a constant voltage source in series with paralleled capacitor-resistor. The value of the resistor is adjusted according to the level of the SC voltage; it becomes negative to charge the SC when the SC voltage is lower than its nominal value; and become positive to discharge the SC when the SC voltage is higher than its nominal value. The power sharing between SC units is ensured by means of virtual impedance control method.

Thirdly, this thesis presents a new control method for the SC to compensate the transient load current and support the system under the pulsed load condition. Moreover, the

cooperation of the multiple SC units in DC microgrid is also ensured by proportionally sharing the supporting current between the SC units. The current sharing between the SC units is achieved by means of the droop control. The conventional droop control is modified so that it can adaptively change its operation mode and parameters in order to compensate the load transient current and regulate the state of charge of the SC.

Fourth, this thesis presents a new configuration of a hybrid energy storage system (HESS) called a battery-inductor-supercapacitor HESS (BLSC-HESS), which is easily implemented to integrate the SC into DC microgrid. It splits the power between a battery and SC, and can operate in parallel. The power sharing is achieved between the battery and the supercapacitor by combining an internal battery resistor and output LSC filter, which consists of a SC and an inductor. The battery current is smoothed to supply and receive only the low-frequency current component under any disturbances and load conditions through cooperation with the SC. Complete guideline to design the parameters of the BLSC-HESS is also presented.

All proposed control methods and configuration are demonstrated by simulation and experiment with DC microgrid prototype in laboratory. Proper comparisons and discussion are provided to show its effectiveness of the improved power management techniques in DC microgrid.

# Acknowledgments

First and foremost, I want to thank my supervisor, Professor Hong-Hee Lee for his support, encouragement, and helpful advice for me to proceed through the doctoral program and complete my PhD thesis at University of Ulsan. He has been a strong and supportive advisor to me throughout my graduate school career. Without his supervision, this thesis would never been successfully completed.

Special thanks to all Professors in Committee Members: Professor Tae-Won Chun, Professor Dong-Choon Lee, Professor Sung-Jin Choi, and Dr. Eui-Heon Jung for their valuable time, guidance and helpful suggestions on my PhD thesis. Also, I would like to express my sincere gratitude to all Professors in School of Electrical Engineering, University of Ulsan (UOU) for their lectures, supports and giving me knowledge.

I also would like to thank NARC (Network-based Automation Research Center) and BK (Brain Korea) 21+ program in UOU for their financial supports. A big thank goes to University of Ulsan for giving me a good opportunity to complete my Ph.D degree successfully.

All former and current members in Industrial Networks and Power Electronics Laboratory also deserve my sincerest thanks, their friendship and assistance has meant more to me than I could ever express. I could not complete my work without their invaluable assistance. I also would like to thank my great friends for helping me defeat the difficult time that I faced during my Ph.D course.

Last but not least, I would like to thank my parents and my brother for for their constant support, encourage, patience, and unconditional love. I love you all dearly.

Ulsan, December 2019

Duy-Hung Dam

# Contents

<b>Abstract</b>	<b>i</b>
<b>Acknowledgments</b>	<b>iii</b>
<b>Abbreviations</b>	<b>xi</b>
<b>Nomenclature</b>	<b>xii</b>
<b>1 Introduction</b>	<b>1</b>
1.1 DC Microgrid . . . . .	1
1.2 Review of DC Microgrid Power Quality . . . . .	2
1.2.1 Power sharing between DGs . . . . .	2
1.2.2 DC bus voltage quality . . . . .	3
1.2.3 Transient current and pulsed load condition . . . . .	4
1.3 Objectives . . . . .	4
1.4 Contribution . . . . .	8
1.5 Outline . . . . .	9
<b>2 DC Microgrid Control Principles and Power Management</b>	<b>11</b>
2.1 Local control in DC microgrid . . . . .	11
2.2 Coordinated control in DC microgrid . . . . .	13
2.2.1 Decentralized Control . . . . .	13
2.2.2 Centralized Control . . . . .	15
2.2.3 Distributed Control . . . . .	16
2.3 DC Microgrid Power Quality Problems . . . . .	17
2.3.1 Power Sharing and Voltage Drop of Droop Controller . . . . .	17
2.3.2 Current Transient and Pulsed Load in DC Microgrid . . . . .	18
<b>3 Accurate Power Sharing and Restored DC Bus Voltage</b>	<b>20</b>
3.1 Distributed Control Method for Proportional Load Power Sharing and Bus Voltage Restoration . . . . .	20
3.1.1 Droop Control . . . . .	21

3.1.2	Distributed Controller . . . . .	22
3.2	Implementation of Controller and Stability Analysis . . . . .	24
3.2.1	Voltage and Current Control Loop . . . . .	24
3.2.2	Droop and Distributed Controller . . . . .	26
3.2.3	Stability Analysis . . . . .	29
3.3	Simulation Results . . . . .	31
3.4	Experimental Results . . . . .	34
3.5	Summary . . . . .	37
<b>4</b>	<b>Dynamic Power Sharing for Transient Current</b>	<b>38</b>
4.1	Adaptive Virtual Impedance Control Method for Supercapacitor . . . . .	39
4.1.1	System Configuration and Conventional Virtual Capacitance Control Method . . . . .	39
4.1.2	Proposed Adaptive Virtual Impedance Control Method . . . . .	40
4.1.3	Simulation Results . . . . .	42
4.1.4	Conclusion . . . . .	45
4.2	Compensate the Pulsed Load Current by Using Supercapacitor . . . . .	48
4.2.1	System Configuration and Conventional Control Method . . . . .	49
4.2.2	Proposed Droop Based Controller for Supercapacitor Unit . . . . .	50
4.2.3	Small Signal Modeling and Controller Design . . . . .	52
4.2.4	Simulation Results . . . . .	56
4.2.5	Experimental Results . . . . .	59
4.2.6	Conclusion . . . . .	62
4.3	Summary . . . . .	63
<b>5</b>	<b>Hybrid Energy Storage System for Power Quality Improvement</b>	<b>64</b>
5.1	System Description . . . . .	65
5.1.1	Cooperation in a DC Microgrid . . . . .	66
5.1.2	Battery and Supercapacitor Models . . . . .	67
5.2	Proposed BLSC-HESS Configuration . . . . .	67
5.2.1	BLSC-HESS Parameters . . . . .	68
5.2.2	Supercapacitor $C_{sc}$ . . . . .	69
5.2.3	The Battery's Internal Resistance $R_b$ . . . . .	70
5.2.4	Inductance $L_1$ . . . . .	71
5.2.5	SC Voltage . . . . .	72
5.2.6	Settling Time . . . . .	72
5.2.7	HESS Control Scheme . . . . .	74



5.2.8 HESS Size and Efficiency Discussion . . . . .	75
5.3 Simulation Results . . . . .	75
5.4 Experimental Results . . . . .	81
5.5 Summary . . . . .	86
<b>6 Conclusions and Future Works</b>	<b>87</b>
6.1 Conclusions . . . . .	87
6.2 Future works . . . . .	89
<b>Bibliography</b>	<b>89</b>
<b>Appendix A - Experimental Setup</b>	<b>98</b>
<b>Appendix B - Publications</b>	<b>101</b>
Journal Articles . . . . .	101
Conferences . . . . .	101

# List of Figures

1.1	Typical configuration of DC microgrid. . . . .	2
1.2	Power of DG units under unbalanced load sharing. . . . .	3
2.1	Droop control method (a) power based, (b) current based. . . . .	12
2.2	A basic diagram of local controller. . . . .	13
2.3	Control principles (a) Decentralized, (b) Centralized, (c) Distributed. . . . .	13
2.4	An example of DC bus signaling control method. . . . .	14
2.5	An example of centralized control method. . . . .	15
2.6	Example of distributed communication network configurations. . . . .	17
2.7	DC microgrid modeling with (a) a droop controller modeled as a DC source and virtual impedance, (b) equivalent circuit of the line impedance. . . . .	18
2.8	SC unit supporting in DC microgrid (a) . . . . .	19
3.1	Droop characteristic after applying a distributed controller. . . . .	21
3.2	Control diagram of proposed distributed control method. . . . .	21
3.3	Control flowchart of proposed distributed controller. . . . .	23
3.4	Control diagram of a single converter. . . . .	24
3.5	Bode diagram of closed voltage and current control loop. . . . .	26
3.6	Simplified control diagram of droop control. . . . .	27
3.7	Simplified control diagram of distributed controller: (a) first term, (b) second term. . . . .	28
3.8	Output and input impedance model of the system. . . . .	28
3.9	Maximum allowable power of CPL with the change of $\alpha$ . . . . .	30
3.10	DC microgrid used in the simulation. . . . .	30
3.11	Performance of proposed method. (a) Power per unit. (b) First term of shifted voltage. (c) Output voltage of DGs. (d) Second term of shifted voltage. . . . .	31
3.12	Dynamic responses for load changes with proposed method. (a) Output currents of DGs. (b) Power per units of DGs. (c) Output voltages of DGs and load voltage. . . . .	32

3.13	Rated power change response of proposed method. (a) Power per unit. (b) First term of shifted voltage. (c) Output voltage of DGs. (d) Second term of shifted voltage. . . . .	33
3.14	DC microgrid used in experiment. . . . .	34
3.15	Dynamic performance of proposed method - DG outputs. . . . .	35
3.16	Dynamic performance of proposed method - DG shifted voltage and load 1 voltage. . . . .	35
3.17	Performance of proposed method in case of load change - DG outputs. . . . .	36
3.18	Performance of proposed method in case of load change - DG shifted voltage terms and load 1 voltage. . . . .	36
4.1	Typical configuration of a DC microgrid including SC units. . . . .	38
4.2	Equivalent circuit of DC microgrid with VCM. . . . .	39
4.3	Proposed control method (a) Equivalent circuit, (b) Virtual resistance lookup curve. . . . .	40
4.4	Bode diagram of virtual impedance of proposed method. . . . .	41
4.5	Control diagram of proposed method. . . . .	41
4.6	Simulation result - two SC units have same parameters. . . . .	43
4.7	Simulation result - two SC units have different SC capacity and $R_{v1min} = R_{v2min} = 0.5$ . . . . .	44
4.8	Simulation result - two SC units have different SC capacity and $R_{v1min} = 1, R_{v2min} = 0.5$ . . . . .	45
4.9	Simulation result - two SC units have different initial SC voltage. . . . .	46
4.10	Simulation result - under continuously load changed. . . . .	47
4.11	Typical configuration of a DC microgrid. . . . .	48
4.12	DC microgrid modeling when VCM control method is used for SC unit. . . . .	48
4.13	Proposed control method (a) DC microgrid equivalent circuit and (b) droop curve. . . . .	51
4.14	(a) Bidirectional Buck-Boost Converter, (b) State 1 – Q1 ON and Q2 OFF, and (c) State 2 – Q1 OFF and Q2 ON. . . . .	52
4.15	Control diagram of proposed method. . . . .	54
4.16	Bode diagram of the inner current control loop. . . . .	55
4.17	Bode diagram of the inner voltage control loop. . . . .	56
4.18	Bode diagram of the SC voltage control loop. . . . .	57
4.19	Simulation result of conventional VC method under pulsed load. . . . .	58
4.20	Simulation result of proposed method under pulsed load. . . . .	59
4.21	Proposed method with different SC voltage loop gains. . . . .	60

4.22	Experimental results – different SC voltage gains. . . . .	61
4.23	Experimental results – different SC droop coefficients. . . . .	62
4.24	Experimental results – different SC initial voltages. . . . .	63
5.1	Typical HESS configurations. . . . .	65
5.2	Typical configuration of DC microgrid with HESS. . . . .	66
5.3	Battery and SC models (a) impedance-based model (b) simple model and (c) SC model. . . . .	66
5.4	Proposed HESS Configuration. . . . .	67
5.5	Bode diagram of $G_{i_{BLSC}}(s)$ (solid lines) and $G_{i_{BSC}}(s)$ (dotted line) accord- ing to $C_{sc}$ with $L_1 = 0.5 \text{ mH}$ , $R_{SC} = 15 \text{ m}\Omega$ , and $R_b = 0.1 \Omega$ . . . . .	70
5.6	Bode diagram of $G_{i_{BLSC}}(s)$ (solid lines) and $G_{i_{BSC}}(s)$ (dotted line) accord- ing to $R_b$ while $L_1 = 0.5 \text{ mH}$ , $R_{SC} = 15 \text{ m}\Omega$ , and $C_{sc} = 28 \text{ F}$ . . . . .	71
5.7	Bode diagram of $G_{i_{BLSC}}(s)$ (solid lines) and $G_{i_{BSC}}(s)$ (dotted line) accord- ing to $L_1$ with $R_b = 0.1 \Omega$ , $R_{SC} = 15 \text{ m}\Omega$ , and $C_{sc} = 28 \text{ F}$ . . . . .	72
5.8	Ratio between settling time and $C_{sc}(R_{bat} + R_{sc})$ . . . . .	73
5.9	Control diagram of BLSC-HESS. . . . .	74
5.10	Case I: Performance simulation result of a single HESS. . . . .	77
5.11	Case II: Impacts of SC capacity $C_{sc}$ and battery internal resistance $R_b$ on simulation results. . . . .	78
5.12	Case II: Impact of the inductance $L_1$ on simulation results. (a) Without $L_1$ , (b) $L_1 = 0.12 \text{ mH}$ , (c) $L_1 = 0.47 \text{ mH}$ . . . . .	79
5.13	Case III: Simulation result of cooperation of two HESSs in the system. . . . .	80
5.14	Case I: Experimental results with single HESS in system. . . . .	82
5.15	Case II: Impacts of SC capacity $C_{sc}$ and battery internal resistance $R_b$ on experimental results. . . . .	83
5.16	Case II: Impact of the inductance $L_1$ on experimental results. (a) Without $L_1$ , (b) $L_1 = 0.47 \text{ mH}$ , (c) $L_1 = 1.12 \text{ mH}$ . . . . .	84
5.17	Case III: Experimental result of cooperation of two HESSs in the system. . . . .	85

# List of Tables

3.1	DC Microgrid Parameters Used in Simulation. . . . .	27
3.2	Load change sequences. . . . .	33
4.1	Parameters used in simulation . . . . .	42
4.2	Parameters used in simulation . . . . .	57
5.1	Comparison between HESS Configurations . . . . .	75
5.2	Parameters used in simulation and experiment. . . . .	76

# Abbreviations

AC	Alternating Current
AVCM	Adaptive Virtual Control Method
BESS	Battery Energy Storage System
CPL	Constant Power Load
DC	Direct Current
DCL	Data Communication Link
DSP	Digital Signal Processor
DG	Distributed Generation
ESS	Energy Storage System
HESS	Hybrid Energy Storage System
MPPT	Maximum Power Point Tracking
SC	Supercapacitor
SoC	State of Charge
PI	Proportional–Integral
PV	Photo-voltaic
VCM	Virtual Capacitance Method

# Nomenclature

$i_{BATi}$	Output current of $i^{\text{th}}$ Battery
$i_{DGi}$	Output current of $i^{\text{th}}$ Distributed Generation
$i_{HESSi}$	Output current of $i^{\text{th}}$ Hybrid Energy Storage System
$i_{out}$	Output current
$i_{SCi}$	Output current of $i^{\text{th}}$ Supercapacitor
$r_d$	Droop coefficient
$V_{load}$	Load voltage
$V_{min}$	Minimum voltage of droop control
$V_{nom}$	Nominal voltage of droop control
$v_{out}$	Output voltage
$v_{SCi}$	Supercapacitor voltage of $i^{\text{th}}$ unit

# Chapter 1

## Introduction

### 1.1 DC Microgrid

To integrate various renewable energy sources and supply power to a remote area, the concept of microgrid has been introduced as an effective solution by Laseter *et al.* [1]. The microgrid is an aggregated entity to integrate the distributed generators (DGs) including the wind turbine, photo-voltaic (PV), and energy storage systems. There are two three type of microgrid: AC microgrid, DC microgrid and Hybrid AC-DC microgrid. The AC microgrid is developed to integrate the AC source from tradition grid such as AC generator and AC loads. When DC coupled renewable energy resources such as the PVs and the energy storage systems are integrated into the AC grid, some additional DC-AC converter is necessary, so that it increases the cost and reduces the system efficiency. To overcome these problems, the DC microgrid has been focused on significantly in these days [2–8]. Besides, the DC microgrid has no issues with reactive power flow and frequency regulation, which results in a notably less complex control system.

The typical DC microgrid system is shown in Fig. 1.1, where all the DGs and loads are connected to a common DC bus. To achieve cooperative control for various sources in microgrid, droop control method has been generally used [8–15]. This method is based on adding a virtual resistance control on top of inner voltage-current control loop. However, it has some drawbacks such as: drop voltage on the DC bus due to the load demand, inaccuracy power sharing due to the different line impedance. In [9], because a small zone DC system is considered, the effect of line impedance is neglected. Nevertheless, this effect becomes significant for a low-voltage DC system, which leads to the different load sharing in distributed source. This problem in the droop control can be solved by a secondary control which can be accomplished by the data communication link (DCL) between DGs [16–19]. In secondary control, there are three categories such as decentralized control [12,13], centralized control [20–23] and distributed control [19,21,24–26]. With advantages



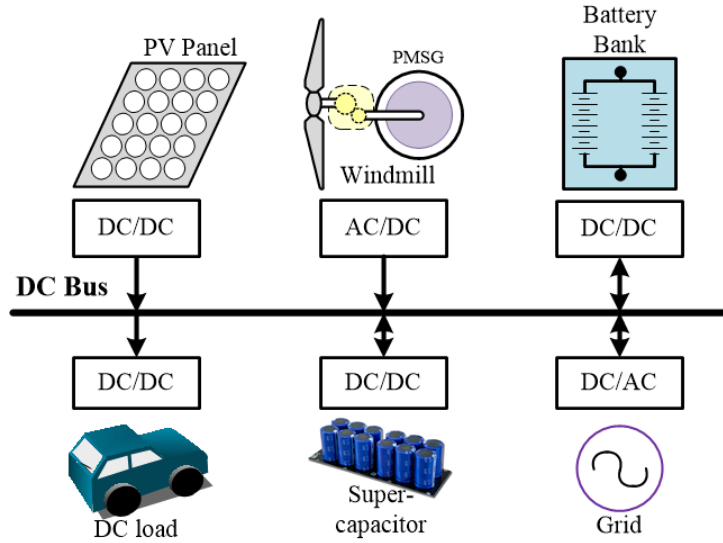


Figure 1.1: Typical configuration of DC microgrid.

of flexible in communication and reality, the distributed control gets noticed.

In order to stabilize the energy in DC microgrid, the battery energy storage system (BESS) is one of the most promising solutions. So, the BESS should has an ability to quickly provide the mismatch power between the load demand power and the harvested power with high power density and energy density. However, none of the recent BESS technology can provide high power density together with high energy density. Fortunately, the supercapacitor has high power density which can be used to compensate the fluctuation of the loads and source currents. To improve the performance of BESS, SC is used to compensate the mismatch current caused by the limitation of BESS power density [27,28].

## 1.2 Review of DC Microgrid Power Quality

### 1.2.1 Power sharing between DGs

In DC microgrid, when unbalanced sharing condition is happened, there will be a source supply higher power than others, which leads it to an overload condition. Therefore, the accuracy sharing current is very importance task in DC microgrid. This problem could happen when there is different in line impedance.

For accurate load sharing, there are two main methods: 1) Adjust the virtual impedance or droop coefficient of droop control [11, 25, 29], 2) Average current method [21]. By increasing the virtual impedance of droop control, S. Anand *et al.* in [25] can reduce the error of sharing the load power but not precisely. Furthermore, this method can increase the output impedance of DG's converter, which leads system become unstable and degrade

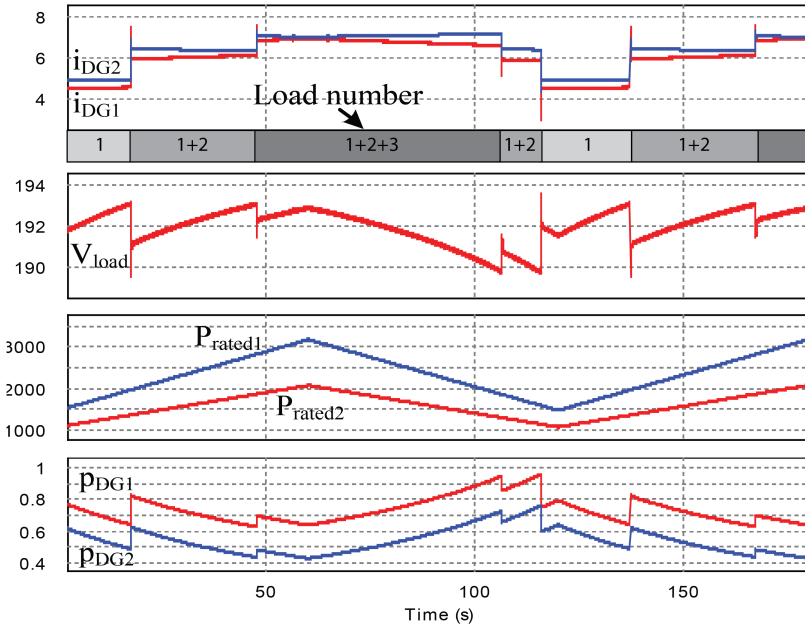


Figure 1.2: Power of DG units under unbalanced load sharing.

the output power of the DGs. In [11,29], the authors adjust the virtual impedance of droop control to adapt the difference line impedance for achieving the correct power sharing. By this way, the total output impedance of all DGs are the same so that the balanced sharing power is ensured. However, this method may affect the stability of the system due to the changes of droop characteristic. Inspire of that, the average current method used in [21] compensate the error of power sharing by adding “shifted voltage” to the reference voltage. This “shifted voltage” is calculated by the error between the output current of each DG to the average current of all DGs. This method does not change the virtual impedance of droop control which makes sure the stability of the system.

### 1.2.2 DC bus voltage quality

Generally, the DC microgrid source is controlled by droop controller to sharing the load power when operating in parallel. However, as a characteristic of droop controller, the output voltage is drop according to the load power condition. As shown in Fig. 1.2, the DC bus voltage when the load changes is swing according to the output power.

Considering the bus voltage quality with the droop control, its drop level depends on the load demand. For bus voltage restoration, the authors in [11, 21, 29, 30] used average voltage to compensate the dropped voltage which made by droop controller. By using DCL, the information of output voltage of DGs is sharing among all DGs; then all DGs output voltage are shifted to make sure the average voltage of all DGs reach

nominal voltage. If the variance of all DG output voltages is small, so this method can regulate the loads voltage closed to nominal voltage. However, in low-voltage DC system, the line impedance effect becomes significant that causes a higher DGs output voltage variance. Therefore, the load voltage, which is lower than the DGs output voltage, become more depressed and cannot be maintained closed to the nominal voltage.

### 1.2.3 Transient current and pulsed load condition

To compensate the transient current and pulsed load current, the SC is used to supply the spike current as it has high power density compare with battery. Generally, the SC is connected to the DC bus by a DC-DC converter. This converter is controlled by a dedicated controller to support the battery in DC microgrid. Because SC is not a generation source, to maintain the available of operation, the voltage or SoC level of SC must be regulated at a certain level.

The recent proposed control methods for SC converter are divided into two group: 1) high-pass filter method and 2) virtual capacitance method. The high-pass filter method uses a high-pass filter to generate the reference output current [31–33]. This method is easily implemented, however, the cooperation of multiple SC units in the system is not guaranteed. To overcome this problem, the virtual capacitance method (VCM) is proposed [34–38], and it becomes popular because it has some advantages such as easy control and effective cooperation of multiple SC units. Unfortunately, both of high-pass filter method and VCM are need an additional controller to regulate the state of charge (SoC) of SC, so that the SC unit must change its operation mode from supporting the microgrid mode to regulating the SoC mode. Many methods have been presented to balance and recover the SoC of SC units, but none of them can operate seamlessly [36,39]. In low-voltage DC microgrid, the pulsed load should be considered [31,40,41]; the pulsed load such as the laser head, drill head, and motor drivers, withdraws a large amount of current in a short time. It makes the system operate under overload condition and unstable. Because of the limited power density, the BESS cannot supply and support the microgrid under the pulsed load condition, and also the recent SC control methods is hard to supply DC current in short interval to support the BESS.

## 1.3 Objectives

From above mentioned problems, this thesis develops advanced control methods for DG units and SC units in DC microgrid to compensate and improve the power quality of the system. In addition, proposed methods should be easily applied in DC microgrid and

keep a superb performance under various conditions. The power quality problems of DC microgrid is cataloged into two groups: static power quality and dynamic power quality. The static power quality is related to power sharing and DC bus voltage restoration in steady state, while the dynamic power quality is related to the response of power delivery of the sources under load changed condition.

### **Power sharing and DC bus voltage restoration**

To reduce the DC bus voltage variation and enhance the load power sharing, several improved control methods have been proposed based on secondary controllers for DC microgrids. Anand *et al.* [25] reduced the error in load power sharing by increasing the virtual impedance, which is used to determine the droop coefficient. They also added a shifted voltage to regulate the voltage variation. Huang *et al.* introduced a method to reduce the DC bus voltage variation by using an average voltage sharing control algorithm [30]. However, these methods did not consider the line voltage fluctuation caused by the load variation, so the current sharing was not accurately achieved.

To solve these problems, Xiaonan *et al.* proposed a low-bandwidth distributed control method to transmit information about the voltage, current, and current sharing ratio of each DG to achieve accurate load power sharing and keep the DC bus voltage stable [21]. Even though they considered the line impedance to share the load power, the power sharing would not be achieved correctly when the load was changed because the line voltage drop due to the load variation was not considered. Moreover, the system can be unstable if the virtual impedance of a DG is not controlled properly.

Recently, a new control method based on a consensus protocol was proposed to overcome DCL failures [11]. The average voltage and current information were used to adjust the droop coefficient and shift the DG output voltages to balance the power sharing and for voltage restoration. However, the DG output voltages change linearly according to the line impedance to balance power sharing, so the output voltage of DGs becomes an outlying nominal voltage due to the significant voltage drop across the line impedance, especially in a low-voltage system. Therefore, the load voltage becomes more depressed and it is difficult to maintain the nominal voltage.

*In order to solve the un-proportional power sharing problem, a shifted voltage method is introduced by considering the line impedance [42]. However, the DC bus voltage is not effectively regulated to its nominal voltage because the DG output voltage drop due to the virtual resistance is not taken into account. In this thesis, we propose a power distributed control method to achieve proportional power sharing and improve the DC bus voltage regulation. This is achieved by directly controlling the output power and the*

*output voltage simultaneously. The average power method was used to control each output power proportionally to the power capacity. A control method called maximum voltage drop compensation is proposed to compensate the voltage drop of all DGs, such that the DG with the lowest output voltage is controlled to reach its nominal voltage. Therefore, the loads voltage in the DC microgrid is optimally restored without adjusting the droop controller coefficient which depends on the rated current of the DG converter. Moreover, with the low sampling frequency of the distributed controller, the proposed method can be implemented with low-cost communication link and simple microprocessor.*

### **Compensate the transient current for DG units**

The bulky and high-cost DC-DC converter used to connect the supercapacitor and battery is another obstacle to integration of the supercapacitor into systems such as electric vehicles and small residential buildings. A passive solution where the battery and supercapacitor are connected in parallel is widely used in electric vehicles because of the low cost, low maintenance, and small volume. Moreover, the passive solution can operate without considering the supercapacitor voltage or SoC. However, when the HESS is used as an input source for a DC-DC converter to increase the power quality of the system, the switching noise and ripple current from the DC-DC converter cannot be filtered out by a conventional parallel battery-supercapacitor configuration. It also has a limitation in that the high-frequency current component leaks to the battery side, which decreases the battery life time.

*To solve this problem, this thesis proposes a battery-inductor-supercapacitor HESS (BLSC-HESS), which we developed by analyzing the HESS and DC-DC converter individually. The BLSC-HESS can be easily connected to any DC-DC converter in a DC microgrid with a simple droop controller. To analyze the reliability of the proposed topology, the parameters were investigated, including the capacitance of supercapacitor, inductance, and internal resistance of the battery.*

As the limitation of the BESS, the SC is used to compensate the current transient for the BESS unit in DC microgrid. The recent proposed control methods for SC converter are divided into two group: 1) high-pass filter method and 2) virtual capacitance method. The high-pass filter method uses a high-pass filter to generate the reference output current [31–33]. This method is easily implemented, however, the cooperation of multiple SC units in the system is not guaranteed. To overcome this problem, the virtual capacitance method (VCM) is proposed [34–36], and it becomes popular because it has some advantages such as easy control and effective cooperation of multiple SC units. Unfortunately, both of high-pass filter method and VCM are need an additional controller to regulate the state

of charge (SoC) of SC, so that the SC unit must change its operation mode from supporting the microgrid mode to regulating the SoC mode. Many methods have been presented to balance and recover the SoC of SC units, but none of them can operate seamlessly [36].

*To compensate the transient current and regulate the SC voltage seamlessly, this thesis proposed a new adaptive virtual impedance control method for SC unit. By adjusting the virtual impedance according to the SC voltage level, the proposed method can seamlessly restore the SC voltage while supporting to compensate the transient current in DC microgrid. The control method is easily implemented by modeling the SC unit as a voltage source in serial with a parallel capacitor and resistor. The performance of proposed method is superb as it can compensate the transient current as well as conventional virtual impedance control method and seamlessly restore the SC voltage.*

The pulsed load such as the laser head, drill head, and motor drivers, withdraws a large amount of current in a short time. It makes the system operate under overload condition and unstable. Because of the limited power density, the BESS cannot supply and support the microgrid under the pulsed load condition; moreover, the recent SC control methods is hard to supply DC current in short interval to support the BESS. There are not many researches to control the microgrid under pulsed load condition [31, 40, 43–46]. Authors in [31] proposed a real-time energy management algorithm for hybrid AC/DC microgrid to minimized the effect of pulsed load on the system stability. However, this control method is implemented in higher level of control, which is hardly achieved in practical. Proposed a controller in [43] actively charges the energy to a super capacitor and rapidly utilized it. This method effectively compensates the peak current of the pulsed load; however, the parallel operation is not considered. The method in [40, 45, 46] can improve the performance of microgrid under pulsed load condition. However, this control method does not compensate the transient current for DGs. A control method that can compensate the transient current for DGs and support current for DGs under pulsed loads condition has not been implemented.

*A droop based controller for SC is proposed to cooperate multiple SC unit and compensate the pulsed load current in DC microgrid [47]. However, the work only shows the controller concept, further studies need to be carried such as detailed design process and stability analysis. In this thesis, we expand the works for analysis the proposed droop-based control method to compensate the transient load current for the pulsed load, and to seamlessly regulate the SoC of SC without any interruption. According to the SoC of SC and load condition, the nominal voltage of droop control is adjusted, and it helps SC converter to change its operation mode and provide the current to compensate the load variation and regulate the SoC at the same time.*

## 1.4 Contribution

From the research objectives presented above, theoretical analysis and experimental implementation for the DC microgrid to tackle various power quality problems such as unbalanced power sharing, DC bus voltage drop, current transient, and pulsed load condition have been investigated in this thesis to demonstrate advanced features of proposed control methods. From view points of the author, main contributions of the thesis are:

- Introduce the basic theory of controlling a DC microgrid from private controller to secondary controller. The power quality problems are pointed out with a theory analysis in detail. Beside that, the recent researches on DC microgrid power quality is reviewed. Based on these analysis, the thesis proposed appropriate control method to compensate and overcome these problems.
- Developed a control method for DG to proportionally sharing the load power and restore the DC bus voltage by only used a low bandwidth communication network. The proposed control method precisely shares the load power despite the load changes and different line impedance. The DC bus voltage is restored by using a shifted-voltage technique, which is regulated by secondary controller in a distributed control concept. A prototype of 2.8kW test bed DC microgrid is implemented and controlled by proposed method.
- Developed an adaptive virtual impedance control method for SC unit to compensate the transient current for DGs in DC microgrid. The virtual impedance is adjusted according to the SC voltage level, so that the output current of SC unit is changed to regulate the SC voltage to reach its nominal value. The SC voltage is restored without any additional controller.
- Developed a droop based control method for SC unit to compensate the transient current and support the DC microgrid under pulsed load condition. The proposed method effectively compensate the transient current as well as conventional virtual capacitance method. Moreover, during the pulsed load is connected, it can support very well the DGs by supplying an amount of DC current by using droop controller. Therefore, the sharing current between SC units is ensured by the mean of droop controller. The effectiveness of proposed method is verified by a DC microgrid prototype controlled by TMS320F28379D.
- Developed a simple and compact HESS configuration to utilize the battery and SC units in DC microgrid. By adding a serial inductor between battery and SC, the

output current of HESS is decoupled into low and high frequency components. The low frequency component is handled by battery, meanwhile the high frequency is handle by the SC. The proposed deliveries a excellent performance in a compact size.

## 1.5 Outline

- **Chapter 1** introduces the basic of DC microgrid and and its power quality problems. In addition, a brief review of recent research is presented regarding to power sharing, DC bus voltage restoration, current transient, and pulsed load problems. Then, the research objectives and contributions are outlined.
- **Chapter 2** presents conventional control method in DC microgrid including the hierarchical control. Beside that, the power quality problems related to the power sharing, DC bus voltage variation, current transient and pulsed load is reviewed.
- **Chapter 3** introduces a new power distributed control method for DC microgrid. This method was developed to share the load power proportionally to the DG rated powers and restore the DC bus voltage. The controller design process is presented in detail along with the system stability analysis. The effectiveness of the method was verified by simulation and experiments, which were carried out using a 2.8-kW prototype of a DC microgrid.
- **Chapter 4** firstly presents an adaptive virtual impedance control method for SC to compensate the transient current in DC microgrid is also presented. The discussion of controller parameters and simulation is carried out to show the effectiveness of proposed control method. Secondly, this chapter presents a new control method for Supercapacitor (SC) to compensate the transient load current and support the system under the pulsed load. The effectiveness of the proposed method is investigated and evaluated by an experimental DC microgrid prototype. The simulation and experimental results prove that the proposed methods can achieve high performance and seamless control.
- **Chapter 5** presents a new configuration of a hybrid energy storage system (HESS) called a battery-inductor-supercapacitor HESS (BLSC-HESS) is presented to effectively compensate the transient current for the battery. Complete guideline to design the parameters of the BLSC-HESS is also presented. Simulation and experimental results prove that the proposed BLSC-HESS configuration achieves high stability performance and lower cost, and it is easily applied to a DC microgrid.



- **Chapter 6** concludes the works in this thesis. In addition, the future works are mentioned to open some new topics on the DC microgrid and its applications.
- **Appendix** shows the experimental setup and used parameters for DC microgrid and SC units.

## Chapter 2

# DC Microgrid Control Principles and Power Management

This chapter presents the basic principles of control methods in DC microgrid and its power quality problems. In general, microgrid consists of a number of parallel converters that operate in harmony. Local control loop handles the functions of: 1) output current-voltage of converter, 2) source function such as MPPT, 3) output signal for upper level control. For secondary control loop, a communication link is necessary to implement the additional functions such as voltage restoration, state-of-charge balancing and current sharing balancing . It can be divided into three groups:

1. *Decentralized control*: Communication link do not exist and power lines are used as the only channel of communication.
2. *Centralized control*: A central controller collects all data from all units and send the control signal to each via communication link.
3. *Distributed control*: A communication link is used between units and an additional control method is operated locally.

The static and dynamic power quality in DC microgrid related to the distribution line impedance, transient current and pulsed load are reviewed in this chapter.

### 2.1 Local control in DC microgrid

In this section, the local control is presented in detail. A basic local controller should include droop control loop and inner voltage-current control loop. Droop control is commonly installed on the top of inner voltage-current loops for current or power sharing purposes. Fig. 2.1 shows the principle of the droop control method based on power or

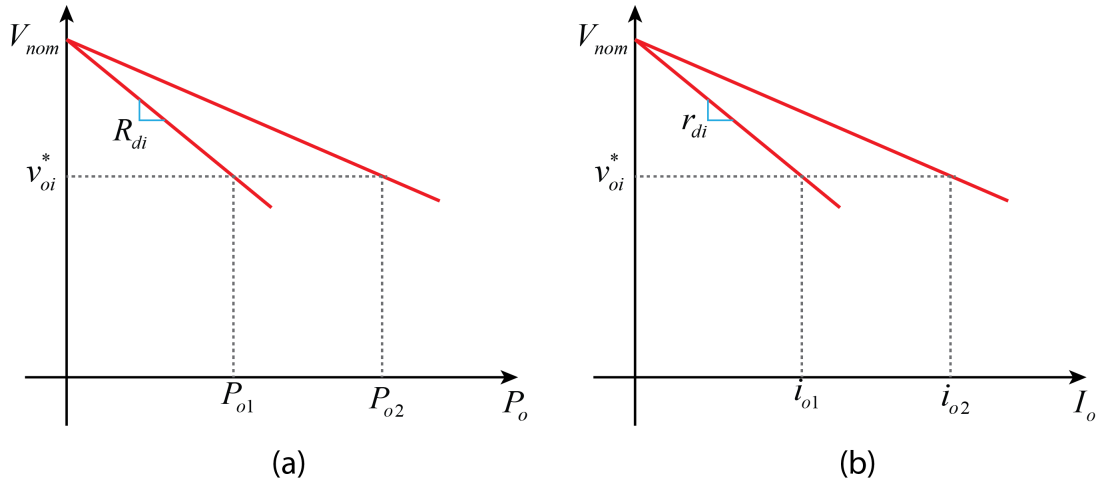


Figure 2.1: Droop control method (a) power based, (b) current based.

current. For the power based droop control, the output voltage reference of  $i^{\text{th}}$  unit can be calculated as

$$V_{oi}^* = V_{nom} - R_{di}P_{oi} \quad (2.1)$$

where  $V_{oi}^*$  is output reference voltage,  $R_{di}$  is power droop coefficient,  $P_{oi}$  is output power of unit  $i^{\text{th}}$ , and  $V_{nom}$  is nominal voltage of DC bus. For the current based droop control, the output voltage of  $i^{\text{th}}$  unit can be calculated as

$$V_{oi}^* = V_{nom} - r_{di}i_{oi} \quad (2.2)$$

where  $r_{di}$  is current droop coefficient of  $i^{\text{th}}$  unit. The droop coefficients have importance effect on the sharing accuracy and stability. The higher droop coefficient, the sharing error is smaller but result in higher DC bus voltage deviation.

To control the converter, a double loop voltage-current control is implemented with the output voltage reference is calculated in (2.1) or (2.2). The control diagram of inner voltage-current loop coordinating with droop controller is shown in Fig. 2.2. Generally, a PI controller is used to control the voltage or current; other advanced controller such as fuzzy, PID can be utilized [48–50].

Finally, the operation mode of the converter can be changed according to the level of DC bus voltage by meaning of droop control method. By adjusting droop parameters, the operation modes of each unit in the system can be managed and changed according to a scheduled scenario. Additional function of local control such as MPPT or charging algorithm are not cover in this thesis.

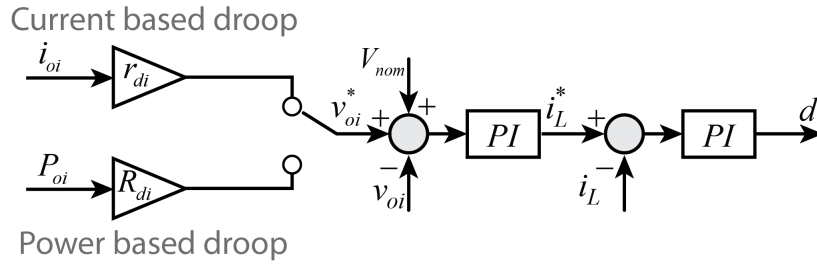


Figure 2.2: A basic diagram of local controller.

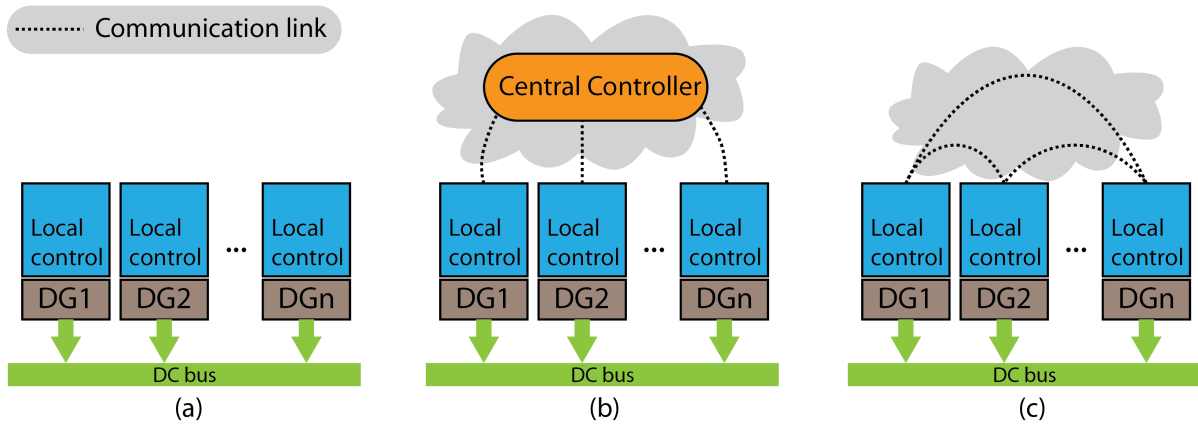


Figure 2.3: Control principles (a) Decentralized, (b) Centralized, (c) Distributed.

## 2.2 Coordinated control in DC microgrid

As discussed, depending on the configuration communication between the units in the DC microgrid, it can be realized either by using decentralized, centralized, or distributed control.

### 2.2.1 Decentralized Control

Decentralized coordination strategies are achieved exclusively by local controller as shown in Fig. 2.3(a). The most common way to implement the decentralized coordination method is using DC bus signaling, adaptive adjustment of droop coefficients, and power line signaling. Without using a communication network, the advantage of decentralized control is independence from digital communication technology. However, due to lack of information from other units, its performance has some limitations. Moreover, these methods use DC bus voltage as a signal to determine the operation mode of each unit, the accuracy of voltage sensors impacts their effectiveness and reliability.

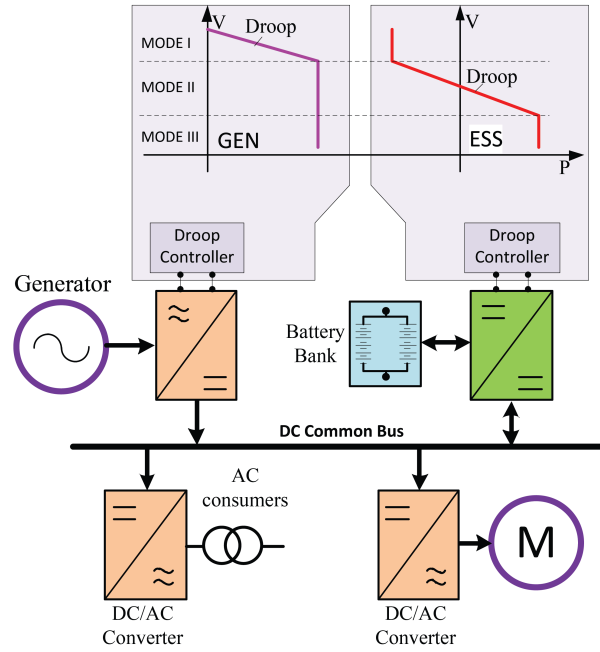


Figure 2.4: An example of DC bus signaling control method.

The methods in [24, 51] used DC bus voltage level to coordinate the operation of each unit on DC microgrid. An example of DC bus signaling method is illustrated in Fig. 2.4, and the operation has three modes:

- Mode I: When load demand is low, the ESS is in charging mode with maximum charging current. The generator is controlled by droop controller to balance the DC bus voltage in order to balance the power. When the load demand increases, the DC bus voltage will reduce as characteristic of droop controller, the system will moves to Mode II.
- Mode II: When the load demand increase, the generator operates in maximum power supplying mode, meanwhile the ESS is controlled by droop controller to maintain the DC bus voltage in order to support the generator in supplying to the load. When load demand reach maximum of supplying capacity of generator and ESS, the system will operate in Mode III.
- Mode III: In this mode, the DC bus voltage keep drop if load demand keep increasing. This means that the system is under overload condition. Some protection methods need to be consider in this mode i.e. load shedding, under-voltage protection.

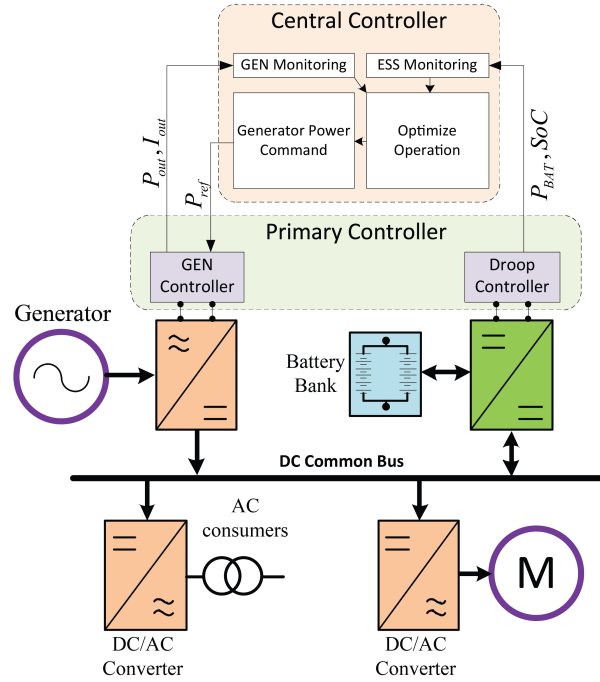


Figure 2.5: An example of centralized control method.

## 2.2.2 Centralized Control

Centralized control can be implemented in DC microgrid by employing a central controller and communication network to connect all the units in the system as shown in Fig. 2.3(b). Centralized control has advantage of implementing advanced control methods since all relevant data can be collected and processed in a single controller. However, the most disadvantage of this strategy is that if a single point of failure appears on the communication network, the whole system will be failure. For a critical applications, redundancy communication network is necessary but it increases the system cost. Many recent researches is presented [20, 23, 52, 53] with advanced functions as multi operation modes, optimal decision, and coordinating and optimal operation.

An example of centralized control is illustrated in Fig. 2.5. In this control method, the generator power is controlled by central controller to obtain optimized operation cost either ESS life time. The ESS is controlled by droop controller to maintain the DC bus voltage; with fast power responding time, the ESS can support the system actively when it operates under peak load. Some advanced functions can be implemented in the central controller such as:

- **Generator and ESS monitoring:** These functions of central controller help to monitor the operation of the system. It also collects the global information of the system.

- **Optimize Operation:** By using collected information of the system and optimization algorithm, the operation cost and life time of ESS is a cost function to optimize the operation of the system. The output power of the generator is the final output of optimization algorithm.
- **Generator Power Command:** Based on the optimized operation information, the central controller can command the operation of generator in order to optimize the system operation.

### 2.2.3 Distributed Control

Distributed control indicates the control principle where central control unit does not exist and LCs communicate only among themselves through dedicated DCLs, as shown in Fig. 2.3(c). The main advantage of this method is that the system can override the single point failure of communication links and maintain fully functional. In order to implement distributed control method, the information between units should be appropriately processed. The local controller only have accessibility to its neighbor units. To overcome this problem, a consensus algorithm can be used. The consensus can be described as

$$\dot{x}_i(t) = \sum_{j \in N_i} [x_i(t) - x_j(t)] + b_i(t) \quad (2.3)$$

where  $x_i(t)$  and  $x_j(t)$  are the value of related variables used in distributed control of  $i^{\text{th}}$  and  $j^{\text{th}}$  unit,  $N_i$  is the set of the neighbors of  $i^{\text{th}}$  unit. The collective dynamics of communication system realized via consensus protocol can be represented by the following equation:

$$\dot{x}(t) = -\Theta x(t) \quad (2.4)$$

where  $\Theta = [\theta_{ij}]$  is the graph Laplacian of the network, which its elements are defined as

$$\theta_{ij} = \begin{cases} -1, & j \in N_i \\ |N_i| & j = i \end{cases} \quad (2.5)$$

where  $|N_i|$  denotes the number of neighbors of unit  $i^{\text{th}}$ . Recently, the consensus is used in many research of microgrid application [54–56].

Distributed control can achieve additional functions such as current sharing, voltage restoration, global efficiency enhancement, SoC balancing, and others can be easily realized. Therefore, distributed control offers much wider functionalities than decentralized control with ride through single point of failure capability. Two examples of distributed

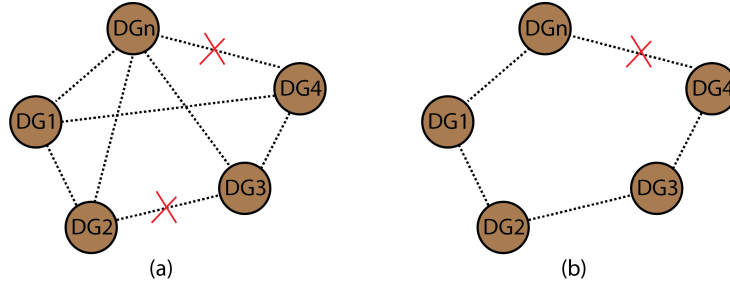


Figure 2.6: Example of distributed communication network configurations.

communication networks is shown in Fig. 2.6. The 1st network configuration in Fig. 2.6(a) has higher redundancy capability more than the one in Fig. 2.6(b).

## 2.3 DC Microgrid Power Quality Problems

The power quality in DC microgrid is cataloged into two types: static power quality and dynamic power quality. The static power quality is considered as the power sharing and DC bus voltage quality in steady state of the system. The dynamic power quality is regarded as the quality of supplying power under load changes. The transient current in this case is compensated to improve the dynamic power quality in DC microgrid.

### 2.3.1 Power Sharing and Voltage Drop of Droop Controller

For a simple analysis, a DC microgrid including two DGs and two loads is considered, as shown in Fig. 2.7(a). The droop controlled DG sources can be modeled with the same voltage magnitude  $V_{dc1} = V_{dc2} = V_{dc}$ , and their virtual impedances  $r_{d1}, r_{d2}, r_{line1}, r_{line2}$  and  $r_{line3}$  are the line impedances, while  $r_{load1}$  and  $r_{load2}$  are the loads. The equivalent load  $\bar{r}_{load}$  and the equivalent line impedances  $r'_{line1}$  and  $r'_{line2}$  are obtained from (1) by applying the delta-star transformation.

$$r'_{line1} = r_{line1} + \frac{r_{line2}r_{load1}}{r_{line2} + r_{load1} + r_{load2}} \quad (2.6)$$

$$r'_{line2} = r_{line2} + \frac{r_{line2}r_{load2}}{r_{line2} + r_{load1} + r_{load2}} \quad (2.7)$$

$$\bar{r}_{load} = \frac{r_{load1}r_{load2}}{r_{line2} + r_{load1} + r_{load2}} \quad (2.8)$$

By using (2.6)(2.7) and (2.8), Fig. 2.7(a) is simplified similarly to Fig. 2.7(b), and the



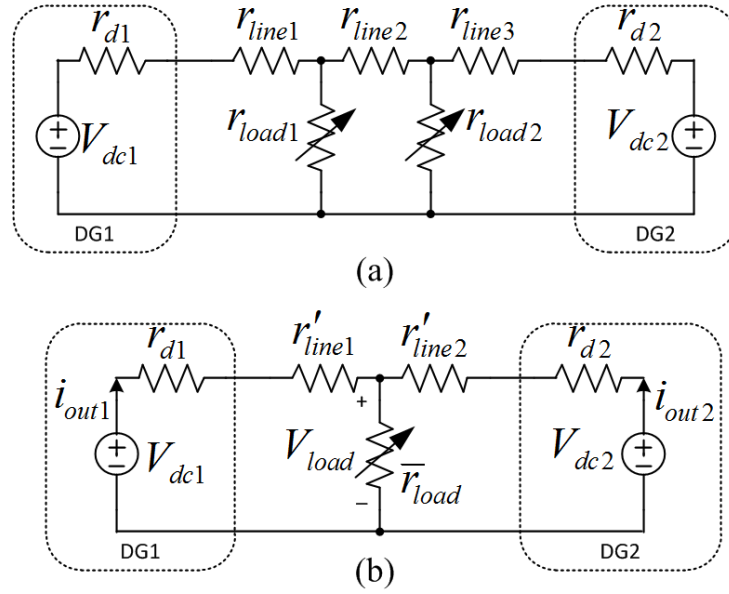


Figure 2.7: DC microgrid modeling with (a) a droop controller modeled as a DC source and virtual impedance, (b) equivalent circuit of the line impedance.

ratio of the output power of the two DGs can be derived as follows:

$$\frac{P_1}{P_2} = \frac{(\bar{r}_{load} + r'_{line1})i_{out1}^2}{(\bar{r}_{load} + r'_{line2})i_{out2}^2} = \frac{V_{dc}i_{out1} - r_{d1}i_{out1}^2}{V_{dc}i_{out2} - r_{d2}i_{out2}^2} \quad (2.9)$$

From (2.6)(2.7)(2.8) and (2.9), if the load is changed, the equivalent line impedance and the power sharing of DGs also change, which makes the load power sharing disproportional. However, if  $V_{dc}$  is adjusted properly, the power sharing can be achieved despite the load change.

From Fig. 2.7(b), the voltage drop is calculated as:

$$V_{load} = V_{dc} - i_{out1}r_{d1} - i_{out1}r'_{line1} \quad (2.10)$$

$$= V_{dc} - i_{out2}r_{d2} - i_{out1}r'_{line2} \quad (2.11)$$

From (2.10) and (2.11), the voltage on the load is drop because of the line impedance and the virtual impedance of the droop controllers.

### 2.3.2 Current Transient and Pulsed Load in DC Microgrid

In DC microgrid, there are various types of loads such as pulsed power loads, propulsion load, dedicated high power loads [57]. Among them, the pulsed power loads such as radars, sonars, and electromagnetic weapons are loads that draw large amount of power

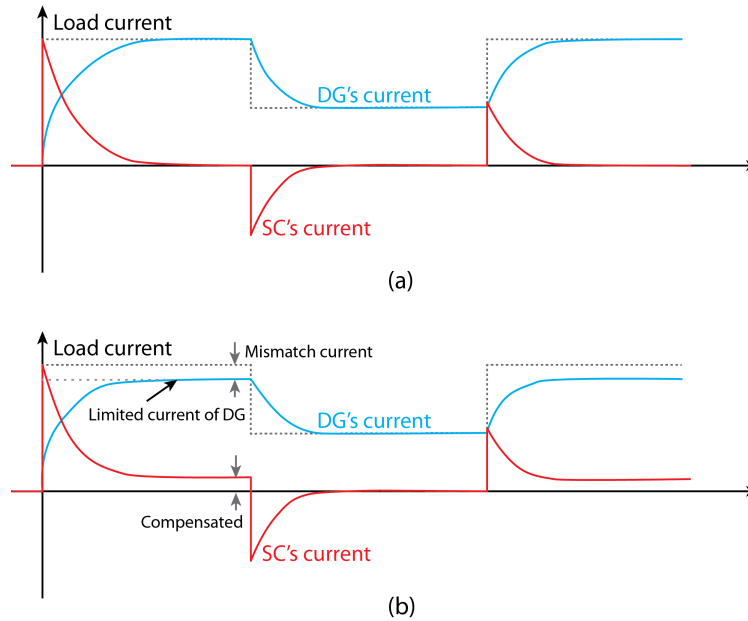


Figure 2.8: SC unit supporting in DC microgrid (a) .

in a short interval from the system. It makes the system operates under overload condition and unstable. Because of the limited power density, the BESS cannot supply and support the microgrid under the pulsed load condition, and also the recent SC control methods is hard to supply DC current in short interval to support the BESS.

The droop control is generally used in DC microgrid to share the current between DGs. Therefore, the output currents of DGs are quickly follow the load demand as droop characteristic. However, the output power of the renewable resource cannot quickly change follow the load demand. To compensate the mismatch between DGs and the load, the SC is used to supply the spike current as shown in Fig. 2.8(a). In this case the SC only can supply the spike current but not a DC current. Recent researches are focus on coordinating the SC unit and DG in DC microgrid and power sharing between SC units and DG units [36, 37, 47, 58–61]. Moreover, the SC voltage level or SOC maintaining of SC also importance task to keep the SC unit can operate continuously.

For above control methods, as the SC cannot supply the DC current component, the SC cannot support the system under pulsed load, which power demand is higher than the DG rated power. As shown in Fig. 2.8(b), the SC unit must supply an amount of DC current as DG meet its limitation of output power to compensate the load demand power. For this problem, there is not a effective method can support the pulsed load and operate in parallel at the same time.

# Chapter 3

## Accurate Power Sharing and Restored DC Bus Voltage

This chapter introduces a new power distributed control method for a DC microgrid to improve power sharing and DC bus voltage quality in steady state. This method was developed to share the load power proportionally to the distributed power source ratings and restore the DC bus voltage when the load changes. To achieve this effectively, a shifted voltage technique was developed based on the power rating and the instantaneous power of distributed generators. By adding the shifted voltage, the voltage drop caused by the droop controller is effectively compensated such that the DC bus voltage is constantly regulated regardless of the load change. To realize the method, all the required information to determine the reference voltage is transmitted through low-bandwidth communication. The controller design process is presented in detail along with a system stability analysis. The effectiveness of the method was verified by simulation and experiments, which were carried out using a 2.8-kW prototype of a DC microgrid.

### 3.1 Distributed Control Method for Proportional Load Power Sharing and Bus Voltage Restoration

Fig. 3.1 shows the droop control characteristics of the proposed method in the frame of the output voltage and output power per unit. Initially, the operation points of two DGs are A1 and A2 for DG1 and DG2, respectively. In this study, both the power sharing and the voltage restoring are achieved by adding two additional voltages called the shifted voltage. The first term of the shifted voltage ( $\Delta V_{d[i]}$ ) is added to each DG to achieve the balanced power per unit (point B1). The second term of the shifted voltage ( $\Delta V_s$ ) is then added to restore the DC bus voltage (the load voltage at point B2). Because these operations are processed simultaneously, the operating points A1 and A2 move directly to

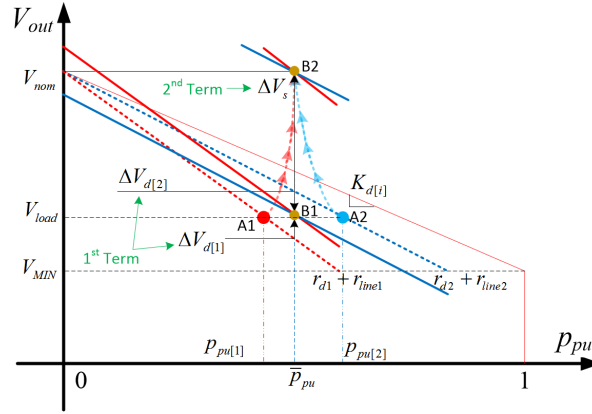


Figure 3.1: Droop characteristic after applying a distributed controller.

B2, as shown in Fig. 3.1. The proposed distributed control diagram is illustrated in Fig. 3.2, which contains three main parts: the droop controller, the distributed controller, and the inner voltage and current controller. Moreover, communication is needed to share information between the DGs for the distributed controller operation.

### 3.1.1 Droop Control

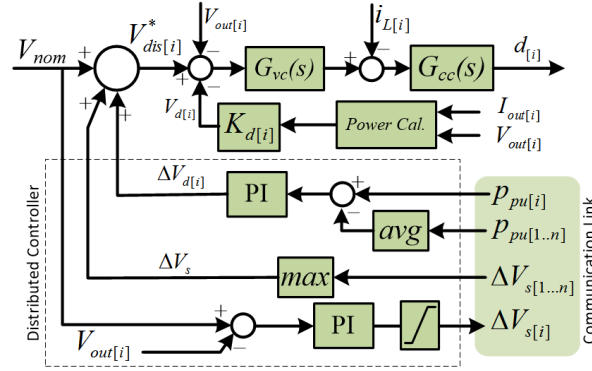


Figure 3.2: Control diagram of proposed distributed control method.

The droop controller determines the virtual voltage drop across the virtual impedance for each DG. The virtual voltage drop is determined by the droop coefficient in Fig. 3.2. To minimize the line voltage drop on the DC bus, the droop control coefficient for all DGs is given by (3.1):

$$K_{d[i]} = \frac{V_{nom} - V_{min}}{P_{rated[i]}} \quad (3.1)$$

where  $K_{d[i]}$  is the droop coefficient of the  $i^{\text{th}}$  DG droop control,  $P_{rated[i]}$  denotes the rated power of  $i^{\text{th}}$  DG, and  $V_{nom}$  and  $V_{min}$  are the nominal and minimum voltages of the DC

bus, respectively. The virtual voltage drop on the  $i^{\text{th}}$  DG is represented by (3.2), where  $P_{[i]}$  and  $p_{pu[i]}$  are the output power and output power per unit of the  $i^{\text{th}}$  DG, respectively.

$$V_{d[i]} = K_{d[i]}P_{[i]} = p_{pu[i]}(V_{nom} - V_{min}) \quad (3.2)$$

From (3.2), the power per unit is proportional to the virtual voltage droop since  $K_{d[i]}$  is constant. If we assume that the proposed control method works properly, the power per unit of all the DGs are balanced, and the virtual voltage drop on all the DGs are the same.

### 3.1.2 Distributed Controller

To obtain the proportional load power sharing for each DG, the first term of the shifted voltage is added to the reference output voltage, which is illustrated in Fig. 3.2. In order to determine the shifted voltage, the output power per unit of each DG is identified through low-bandwidth communication. Then, the average power supply of all DGs is obtained by (3.3).

$$\bar{p}_{pu} = \left( \sum_{i=1}^n p_{pu[i]} \right) / n, \quad p_{pu[i]} = \frac{P_{[i]}}{P_{rated[i]}} \quad (3.3)$$

where  $\bar{p}_{pu}$  is the average power supply of all DGs. The first term of shifted voltage of the droop control for each DG becomes as follows:

$$\Delta V_{d[i]} = \left( k_P^d + \frac{k_I^d}{s} \right) (\bar{p}_{pu} - p_{pu[i]}) \quad (3.4)$$

where  $k_P^d$  and  $k_I^d$  are the gains of proportional–integral (PI) controller for the first term.

Due to the line voltage drop and the virtual voltage drop, the voltage at the load is much lower than its nominal value as shown in Fig. 3.1. Therefore, the reference voltage of the DG should be boosted to restore the DC bus voltage to the nominal value. In order to regulate the DC bus voltage, the estimated voltage drop of the  $i^{\text{th}}$  DG  $\Delta V_{s[i]}$  in (3.5) is calculated based on the level of all the DGs.

$$\Delta V_{s[i]} = \left( k_P^s + \frac{k_I^s}{s} \right) (V_{nom} - V_{out[i]}) \quad (3.5)$$

where  $k_P^s$  and  $k_I^s$  are the PI controller gains of the second shifted voltage for each DG.  $\Delta V_{s[i]}$  is calculated locally in the  $i^{\text{th}}$  DG, and this value is shared with other DGs to select the second term. The largest voltage drop in (3.5) is selected as the second shifted voltage

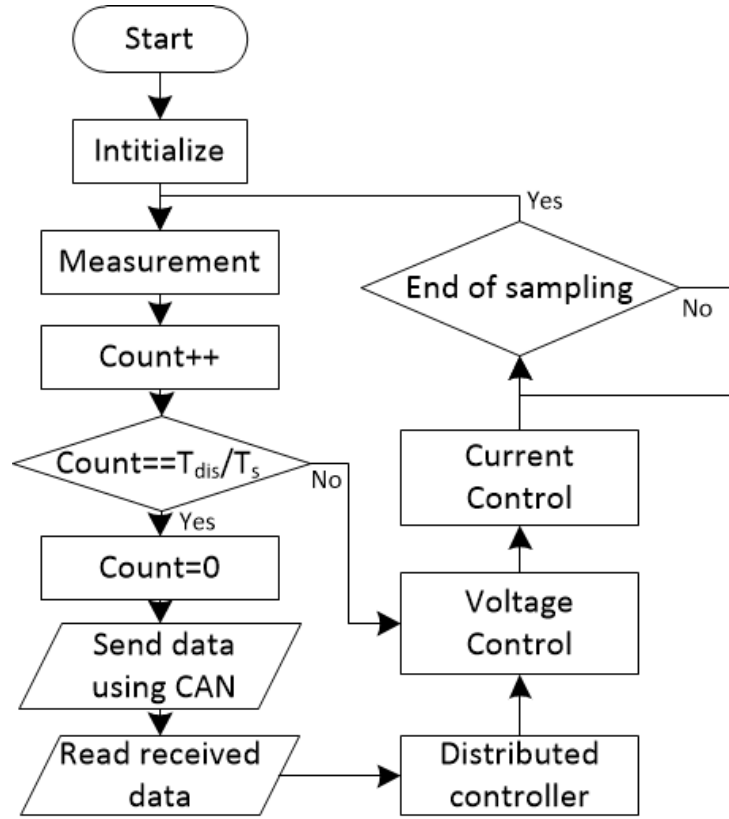


Figure 3.3: Control flowchart of proposed distributed controller.

term in order to compensate the voltage drop at the load effectively:

$$\Delta V_s = \max_{i=1..n} (\Delta V_{s[i]}) = \Delta V_{s[m]} \quad (1 \leq m \leq n) \quad (3.6)$$

where  $\Delta V_{s[m]}$  is the voltage drop of the  $m^{\text{th}}$  DG that is largest among the voltage drops obtained from (3.5). Finally, the reference voltage of the  $i$ th DG becomes the following:

$$V_{[i]}^* = V_{nom} - V_{d[i]} + \Delta V_{d[i]} + \Delta V_s \quad (i = 1..n) \quad (3.7)$$

The output voltage reference in (3.7) is obtained from only a PI controllers in (3.5) and a simple comparison to find maximum value in (3.6). Therefore, the calculation burden of distributed controller is much reduced.

A flowchart of the data flow is shown in Fig. 3.3, where the control loop is executed every 20ms after sending or receiving data to and from the other DGs,  $T_{dis}$  is the period of sending or receiving data, and  $T_s$  is the sampling period of the DG controller. The inner voltage and current controllers are much faster than the droop and distributed controllers, so the output voltage and current of the DG reach the reference values before

the next distributed control cycle. By substituting (3.5) and (3.6) into (3.7), the following is obtained:

$$V_{[i]}^* = V_{nom} - V_{d[i]} + \Delta V_{d[i]} + \left( k_P^s + \frac{k_I^s}{s} \right) (V_{nom} - V_{out[m]}) \quad (i = 1 \dots n) \quad (3.8)$$

Equation (3.8) shows that the reference voltages of the remaining DGs are calculated with the second term from the  $m^{\text{th}}$  DG in (3.6) and the first term in (3.4). At steady state,  $\Delta V_{s[m]}$  reaches a constant value when the output voltage of the  $m^{\text{th}}$  DG is equal to the nominal voltage, and  $\Delta V_{d[i]}$  is controlled by a PI controller in (3.4) to adjust the output power to the average value. In addition, the load voltage is calculated from (3.9):

$$\begin{aligned} V_{load} &= V_{out[m]} - i_{out[m]} r'_{line[m]} \\ &= V_{nom} - i_{out[m]} r'_{line[m]} \end{aligned} \quad (3.9)$$

Because the equivalent line impedance  $r'_{line[m]}$  is small in practical applications, the load voltage can be kept at the almost nominal voltage in spite of the load current variation.

## 3.2 Implementation of Controller and Stability Analysis

### 3.2.1 Voltage and Current Control Loop

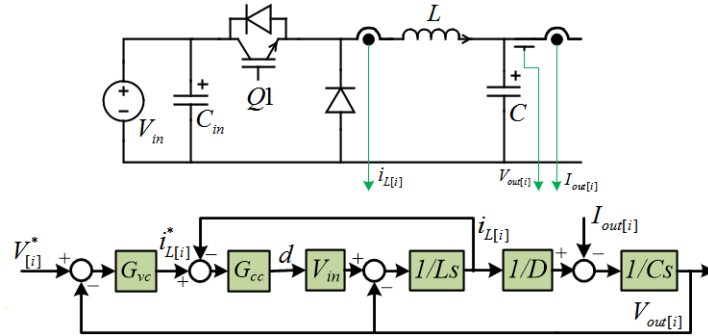


Figure 3.4: Control diagram of a single converter.

A DG converter in microgrid is implemented based on a Buck converter. As shown in Fig. 3.4, a double loop controller is employed for each DG converter with the reference voltage calculated from (3.8). To coordinate the inner control loop, the current controller should have high bandwidth. The inner current control loop is derived as:

$$\left[ G_{cc}(s) (i_{L[i]} - i_{L[i]}^*) V_{in} - V_{out[i]} \right] \frac{1}{Ls} = i_{L[i]} \quad (3.10)$$

Next, the open loop and closed loop transfer functions of the current controller are obtained as (3.11) and (3.12), respectively:

$$T_{CO} = V_{in}G_{cc}(s)\frac{1}{Ls} \quad (3.11)$$

$$T_{CC} = \frac{V_{in}G_{cc}(s)}{V_{in}G_{cc}(s) + Ls} \quad (3.12)$$

where the PI regulator of the current controller is expressed as:

$$G_{cc} = k_{Pc[i]} + \frac{k_{Ic[i]}}{s} \quad (3.13)$$

The cut-off frequency  $f_{cc}$  of the current control loop is chosen as 1/20 of the switching frequency  $f_s$ . The phase margin of the current loop should be greater than  $\pi/4$ , and the PI controller parameters are designed based on (3.14) and (3.15).

$$T_{CO}(j\omega_{cc}) = \left| V_{in} \left( k_{Pc[i]} + \frac{k_{Ic[i]}}{j\omega_{cc}} \right) \frac{1}{j\omega_{cc}L} \right| = 1 \quad (3.14)$$

$$\angle T_{CO}(j\omega_{cc}) \geq -\frac{3}{4}\pi, \quad (3.15)$$

where  $\omega_{cc} = 2\pi f_{cc} \cdot k_{Pc[i]}$  and  $k_{Ic[i]}$  are then obtained from (19):

$$\begin{cases} k_{Pc[i]} = \omega_{cc}L/V_{in} \\ \frac{k_{Ic[i]}}{k_{Pc[i]}} = \lambda_c\omega_{cc} \end{cases}, \quad (3.16)$$

where  $\lambda_c$  is a value between 0.1 and 1 to ensure that the phase margin satisfies (3.15), and it is chosen as 0.2 to have a good damping ratio of the closed-loop  $T_{CC}$ .

The voltage control loop is expressed as:

$$\left[ (V_{[i]}^* - V_{out[i]}) G_{vc}(s)T_{CC}(s)\frac{1}{D} - I_{out[i]} \right] \frac{1}{Cs} = V_{out[i]}. \quad (3.17)$$

The open loop and closed loop transfer functions of the voltage controller are given in (3.18) and (3.19), respectively:

$$T_{VO} = G_{vc}(s)T_{CC}(s)\frac{1}{DCs} \quad (3.18)$$

$$T_{VC} = \frac{G_{vc}(s)T_{CC}(s)}{G_{vc}(s)T_{CC}(s) + DCs}, \quad (3.19)$$



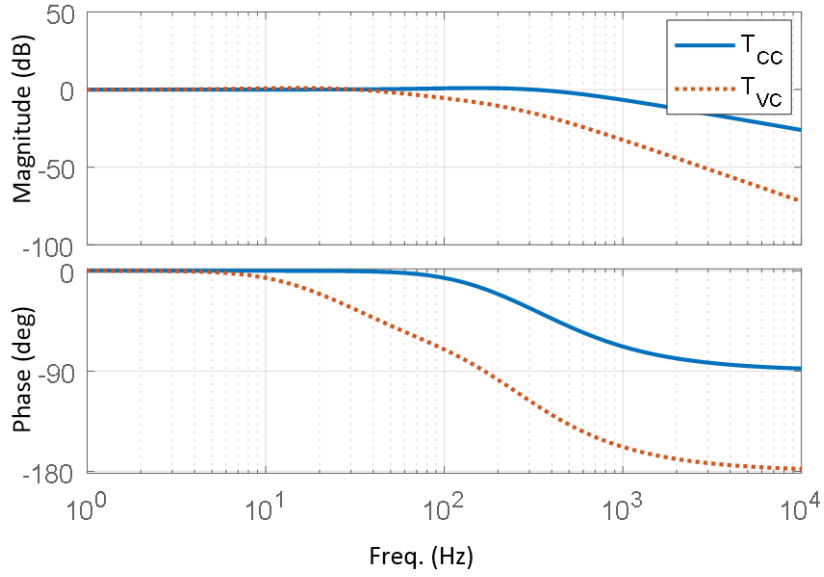


Figure 3.5: Bode diagram of closed voltage and current control loop.

where the PI regulator to control the output voltage  $G_{vc}$  is expressed as:

$$G_{vc} = k_{Pv[i]} + \frac{k_{Iv[i]}}{s} \quad (3.20)$$

The cut-off frequency  $f_{cc}$  of the current control loop is much higher than that of the voltage control loop ( $f_{vc}$ ), so the current closed loop gain is regarded as unity in the frequency range in which the outer voltage control loop is designed. Next, using a similar procedure to that used for the current loop design, the parameters and of the PI regulator of the voltage controller are obtained as follows:

$$\begin{cases} k_{pv[i]} = DC\omega_{vc} \\ \frac{k_{Iv[i]}}{k_{Pv[i]}} = \lambda_v\omega_{vc} \end{cases} \quad (3.21)$$

where  $\omega_{vc} = 2\pi f_{vc}$ , and  $\lambda_v$  is a value between 0.1 and 1 to maintain an ideal phase margin that is chosen as 0.2 to have a good damping ratio of the closed loop  $T_{VC}$ . With the parameters in table 3.1, the Bode diagrams for the current and voltage closed loops are shown in Fig. 3.5.

### 3.2.2 Droop and Distributed Controller

Fig. 3.6 shows the simplified control diagram of the droop controller using parameters calculated from (3.1). In Fig. 3.6,  $V_{dis[i]}^*$  is the reference voltage obtained after the

Table 3.1: DC Microgrid Parameters Used in Simulation.

Parameters	Symbol	Value
<b>DC Microgrid Parameters</b>		
Bus Voltage	$V_{nom}$	200V
	$V_{MIN}$	190V
Rated Powers	$P_{rated[1],[2],[3]}$	0.7, 1.5, 1.5 kW
Line Impedances	$r_{line}$	0.1 $\Omega$
Load 1, 2, 3		22, 66, 132 $\Omega$
<b>DC-DC Converter Parameters</b>		
Output Capacitor	$C$	2200 $\mu F$
Inductor	$L$	0.5mH
Input Voltage	$V_{in}$	3300V

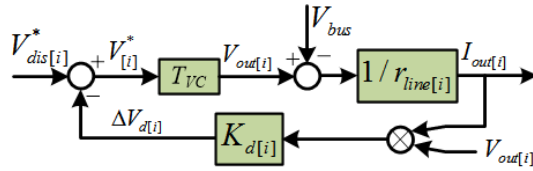


Figure 3.6: Simplified control diagram of droop control.

distributed controller, as shown in Fig. 3.2. The output voltage of the  $i^{\text{th}}$  DG is described as:

$$\begin{aligned}
 V_{out[i]} &= (V_{dis[i]}^* - K_{d[i]} V_{out[i]} I_{out[i]}) T_{VC} \\
 &= V_{dis[i]}^* T_{VC} - K_{d[i]} V_{out[i]} T_{VC} I_{out[i]} \\
 &= V_{nom} - Z_{out[i]} I_{out[i]}
 \end{aligned} \tag{3.22}$$

where  $Z_{out[i]}$  is the output impedance of the  $i^{\text{th}}$  DG:

$$Z_{out[i]} = \frac{V_{nom} (1 - T_{VC}) - (\Delta V_{d[i]} + \Delta V_s) T_{VC}}{I_{out[i]}} + K_{d[i]} V_{out[i]} T_{VC} \tag{3.23}$$

The negative sign in (3.23) shows that the distributed controller helps to reduce the output impedance of DG converter.

The cut-off frequency of the distributed controller  $f_{dis}$  is much lower than that of the inner loop controllers. Thus, the inner control loop gain  $G_v(s)$  can be regarded as unity when the distributed control loop is analyzed. Hence, the distributed control diagram can be simplified as shown in Fig. 3.7. From Fig. 3.7(a), the transfer function is expressed as follows for the open control loop of the first term for equalizing the output power of each

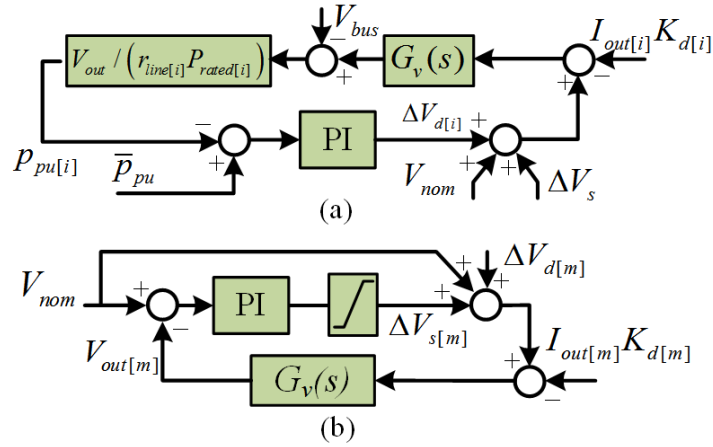


Figure 3.7: Simplified control diagram of distributed controller: (a) first term, (b) second term.

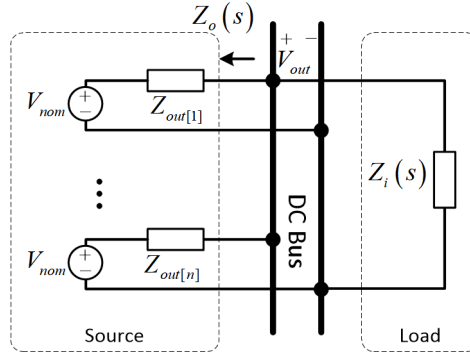


Figure 3.8: Output and input impedance model of the system.

DG unit:

$$\begin{aligned}
 T_{OD1} &= \left( k_P^d + \frac{k_I^d}{s} \right) G_v(s) \frac{V_{out}}{r_{line[i]} P_{rated[i]}} \\
 &\approx \left( k_P^d + \frac{k_I^d}{s} \right) \frac{V_{out}}{r_{line[i]} P_{rated[i]}}
 \end{aligned} \tag{3.24}$$

The PI parameters of the first term are selected as  $k_P^d = 0.1$  and  $k_I^d = 31.0$  to make the open loop cut-off frequency 5 Hz.

From Fig. 3.7(b), the open loop transfer function of the second term for the  $m^{\text{th}}$  DG is expressed as:

$$T_{OD2} = \left( k_P^s + \frac{k_I^s}{s} \right) \tag{3.25}$$

The open-loop cut-off frequency is also selected as 5Hz, and the PI parameters of the second term become  $k_P^s = 0.1$  and  $k_I^s = 31.0$  from (3.25).

### 3.2.3 Stability Analysis

A DC microgrid with  $n$  DG units as shown in Fig. 3.8 is considered for the system stability analysis under the constant power load (CPL) by means of the Middlebrook criterion in [62]. In the Middlebrook criterion, the ratio between the source output impedance and the load input impedance is defined as the minor loop gain  $T_{MLG}$ , and it is used to evaluate the system stability. To guarantee the system stability,  $T_{MLG}$  should satisfy the following condition:

$$|T_{MLG}| = \left| \frac{Z_o}{Z_i} \right| = \frac{1}{GM} < 1, \quad (3.26)$$

where  $Z_o$  is the source output impedance,  $Z_i$  is the load input impedance, and  $GM$  is the gain margin. From Fig. 3.8, the output impedance  $Z_o$  is calculated as:

$$Z_o(s) = Z_{out[1]} \parallel Z_{out[2]} \parallel \dots \parallel Z_{out[n]}, \quad (3.27)$$

where  $Z_{out[i]}$  is defined in (3.23). A CPL can be modeled as a negative resistance  $Z_{CPL}$  parallel with a constant current source  $I_{CPL}$  as follows [63]:

$$\begin{aligned} Z_i(s) = Z_{CPL}(s) &= -\frac{V_{out}^2}{P_{CPL}} \\ I_{CPL} &= 2\frac{P_{CPL}}{V_{out}} \end{aligned} \quad (3.28)$$

where  $V_{out}$  is DC bus voltage, and  $P_{CPL}$  is the power dissipated in CPL.

To simplify the stability analysis, we assume that all DGs have the same configuration and that their output impedances are the same. Then, from (3.23) and (3.27), the output impedance  $Z_o$  becomes (3.29) by assuming that  $T_{VC} = 1$ :

$$Z_o(s) = \left( -\frac{\Delta V_d + \Delta V_s}{I_{out}} + K_d V_{out} \right) \frac{1}{n} \quad (3.29)$$

After substituting (3.28) and (3.29) into (3.26), the minor loop gain becomes

$$|T_{MLG}| = \left| \frac{K_d P_{CPL}}{n V_{out}} - \frac{P_{CPL} \Delta V}{n V_{out}^2 I_{out}} \right| < 1 \quad (3.30)$$

where  $\Delta V = \Delta V_d + \Delta V_s$ . From Fig. 3.8, the load power  $P_{CPL}$  is given as follows:

$$P_{CPL} = \frac{(V_{nom} - V_{out})}{Z_o} V_{out} \quad (3.31)$$

Substituting (3.29) and (3.31) into (3.30), the minor loop gain  $|T_{MLG}| < 1$  when

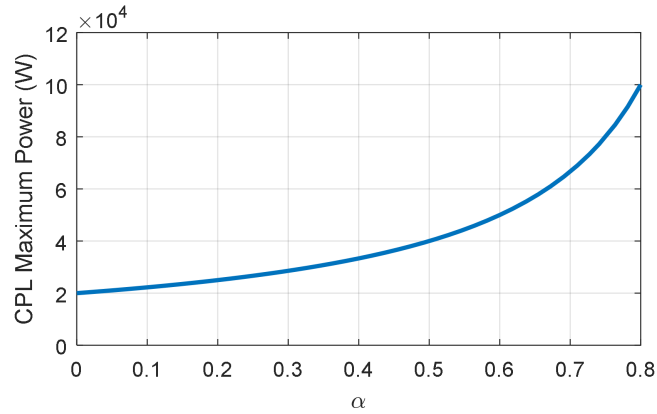
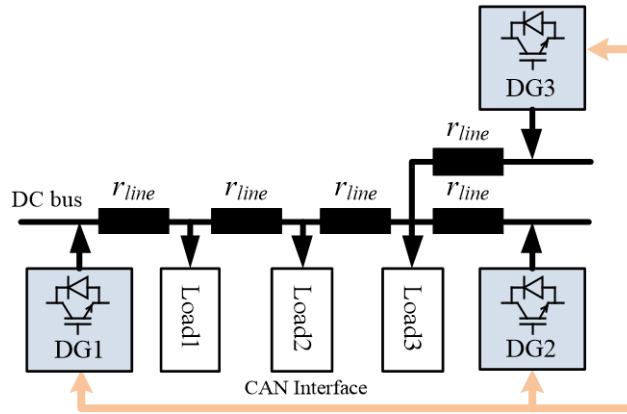

 Figure 3.9: Maximum allowable power of CPL with the change of  $\alpha$ .


Figure 3.10: DC microgrid used in the simulation.

$V_{out} > 0.5V_{nom}$ . So, the maximum allowable load power  $P_{max}$  to keep the system stable is determined when  $V_{out} = 0.5V_{nom}$ :

$$P_{max} = \frac{nP_{rated}}{\left(\frac{2V_{nom}(V_{nom}-V_{min})}{V_{nom}^2} - \frac{4\Delta V P_{rated}}{V_{nom}^2 I_{out}}\right)} \quad (3.32)$$

Fig. 3.9 shows the maximum allowable of CLP with the DC microgrid parameters in table 3.1 and  $\alpha = \Delta V/I_{out}$ . From Fig. 3.9, it is clear that the maximum allowable power of CPL is much higher than the system rated power. Therefore, the DC microgrid with the rated load power is always stable with the proposed method. When the distributed controller regulates the output impedance in (3.29) to be smaller, the minor loop gain  $T_{MLG}$  in (3.26) also becomes smaller. Therefore, the system stable margin is increased.

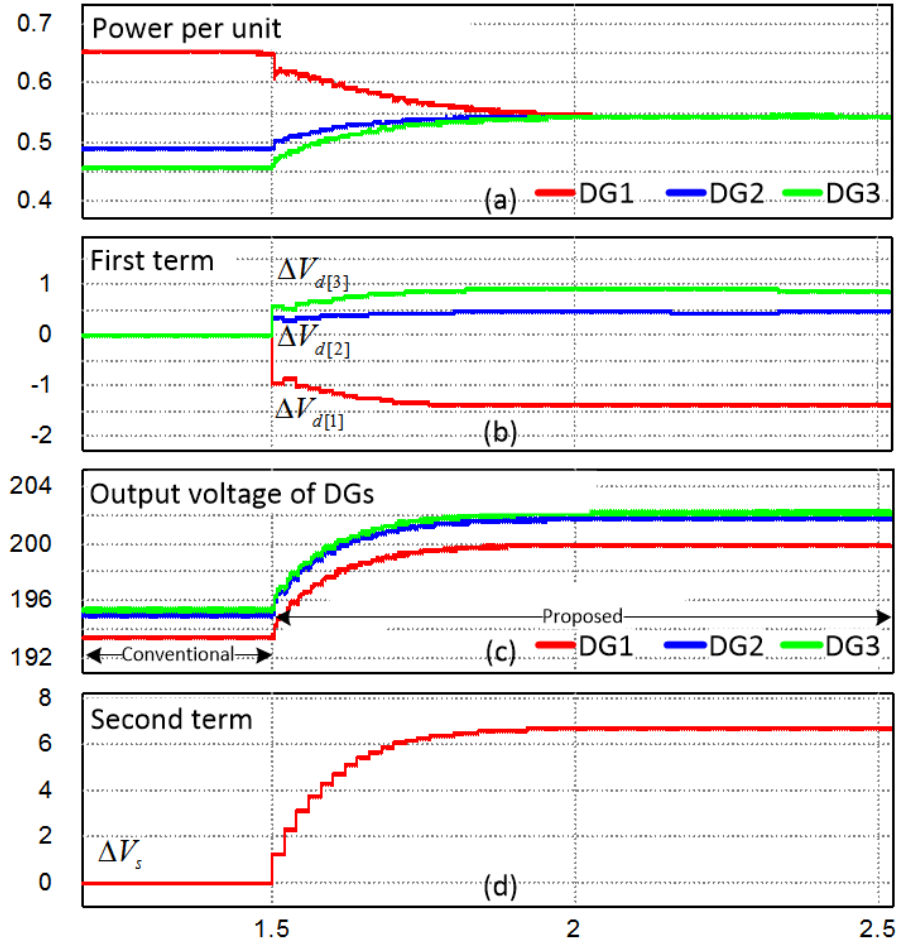


Figure 3.11: Performance of proposed method. (a) Power per unit. (b) First term of shifted voltage. (c) Output voltage of DGs. (d) Second term of shifted voltage.

### 3.3 Simulation Results

To evaluate the performance of the proposed method, a DC microgrid with three sources was simulated using PSIM 9.0.2, as shown in Fig. 3.10. The parameters used for the simulation are listed in Table 3.1. Each source is composed of a DC-DC buck converter with an inner voltage–current controller, as shown in Fig. 3.4.

Fig. 3.11 shows the performance of the proposed control method with a constant load (only load 1 is connected). The proposed control method is applied at  $t = 1.5$  s. Before this time, the output powers per unit of DG1, DG2, and DG3 are 0.65, 0.49, and 0.46, respectively. When the proposed scheme starts to operate at  $t = 1.5$  s, the output power of each DG reaches 0.54 for each unit, as shown in Fig. 12(a). This occurs by adjusting the first term,  $\Delta V_{d[i]}$ , which is plotted in Fig. 3.11(b). Fig. 3.11(c) shows that the decreased DC bus voltage is restored to the nominal value by adding the second term in

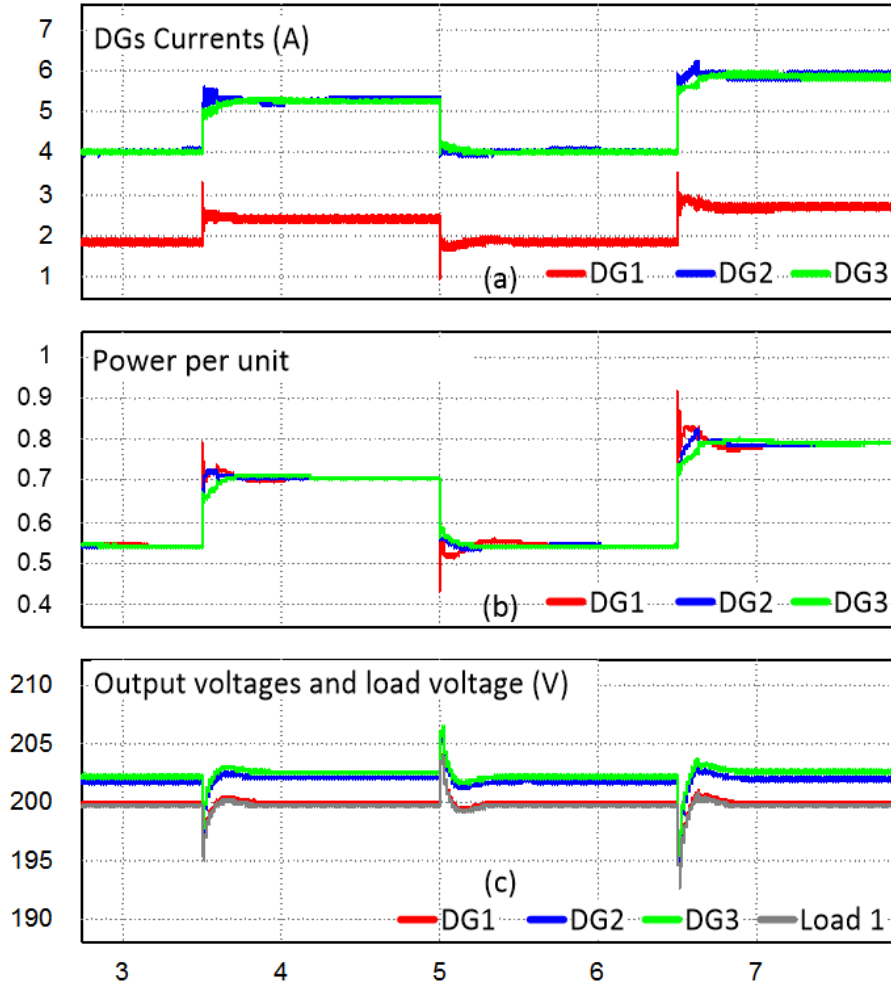


Figure 3.12: Dynamic responses for load changes with proposed method. (a) Output currents of DGs. (b) Power per units of DGs. (c) Output voltages of DGs and load voltage.

Fig. 3.11(d) to every DG's reference voltage. In this case, DG1 with the lowest output voltage is regulated to reach the nominal value of 200V, so the voltage drop at the loads is minimized.

Fig. 3.12 shows the dynamic response for the load changes with the sequence described in Table 3.2. After a short transient time, each output current of a DG in Fig. 3.12(a) becomes proportional to its rated power, the output powers per unit for all DGs become exactly the same, as shown in Fig. 3.12(b), and the lowest load voltage is restored to the nominal value of 200V, as shown in Fig. 3.12(c).

Fig. 3.13 shows the dynamic performance of the proposed method from when the rated power of a DG changes under the same load conditions. Initially, all DGs operate with the rated powers given in Table I. At  $t = 5s$ , the rated power of DG1 changes from 0.7kW to 1.5kW, and both DG2 and DG3 change from 1.5kW to 0.7kW. Fig. 3.13(a) shows

Table 3.2: Load change sequences.

Time (s)	Load connected
0 to 3.5	Load 1
3.5 to 5	Load 1+2
5 to 6.5	Load 1
6.5 to 8	Load 1+2+3

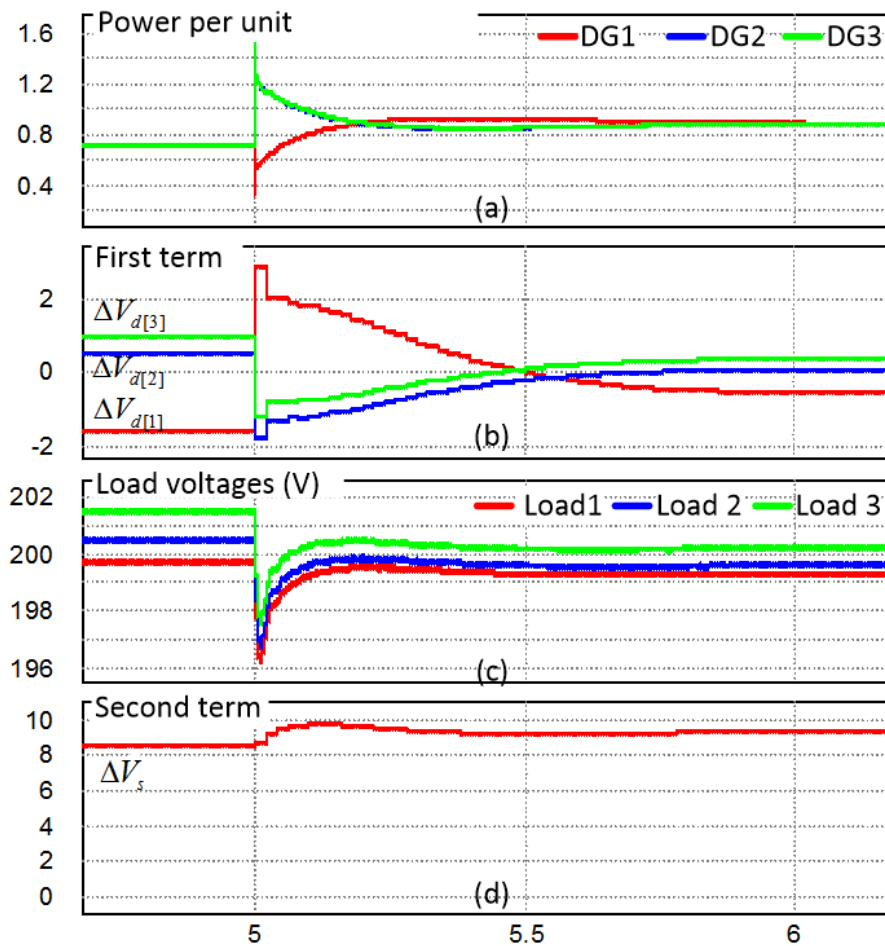


Figure 3.13: Rated power change response of proposed method. (a) Power per unit. (b) First term of shifted voltage. (c) Output voltage of DGs. (d) Second term of shifted voltage.



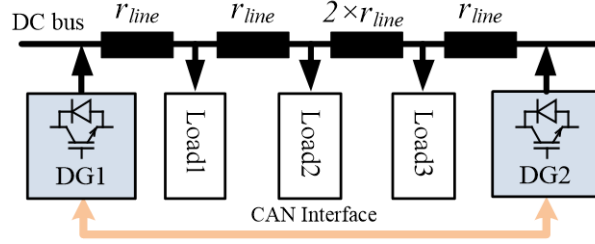


Figure 3.14: DC microgrid used in experiment.

that the powers per unit of all DGs are increased from 72% to 87% by controlling the shifted voltage  $\Delta V_{d[i]}$  plotted in Fig. 3.13(b) because of the reduced total rated power. As shown in Fig. 3.13(c), the load voltage is effectively regulated within 1% tolerance of the nominal voltage of 200V by adjusting the second term plotted in Fig. 3.13(d).

### 3.4 Experimental Results

For simple experimental verification, the DC microgrid with two DGs shown in Fig. 3.14 was used instead of the three DGs used in the simulation because DG2 and DG3 are located close together and their performance is almost the same. The parameters used in the experiment are shown in Table 3.1. DGs are controlled by two DSP TMS320F28335 microcontrollers, and a CAN interface is implemented with the built-in microcontroller CAN module. To emulate the delay time, a low frequency of 50Hz (20ms) is considered for sending and receiving data. Each DG shares its power per unit information in (3.3) and the second term of the shifted voltage in (3.6).

To investigate the performance of the proposed method, only load 1 is connected to the DC bus, and two DGs are connected with the rated power given in Table 3.1. In Fig. 3.15, after a short transient time of almost 500ms, each DG shares the load power proportionally to its power rating (in this case, the power per units are the same), and the lowest output voltage is regulated to the nominal value of 200V. Fig. 3.16 shows the first terms of the shifted voltage for the droop control ( $\Delta V_{d[1]}, \Delta V_{d[2]}$ ), the second term ( $\Delta V_s$ ), and the lowest output voltage ( $V_{DG1}$ ). In Fig. 3.16, the load voltage is constantly regulated at 200V with a small tolerance of 1V.

Fig. 3.17 shows the dynamic performance of the proposed method from when the load was sequentially connected to the DC bus with an interval of 2s. From Fig. 3.17, the lowest output voltage of DG1 is regulated to the nominal value of 200V, while the load power is proportionally shared. Fig. 3.18 shows the shifted voltage terms during the load changes. The behavior of the experimental results exactly corresponds to that of

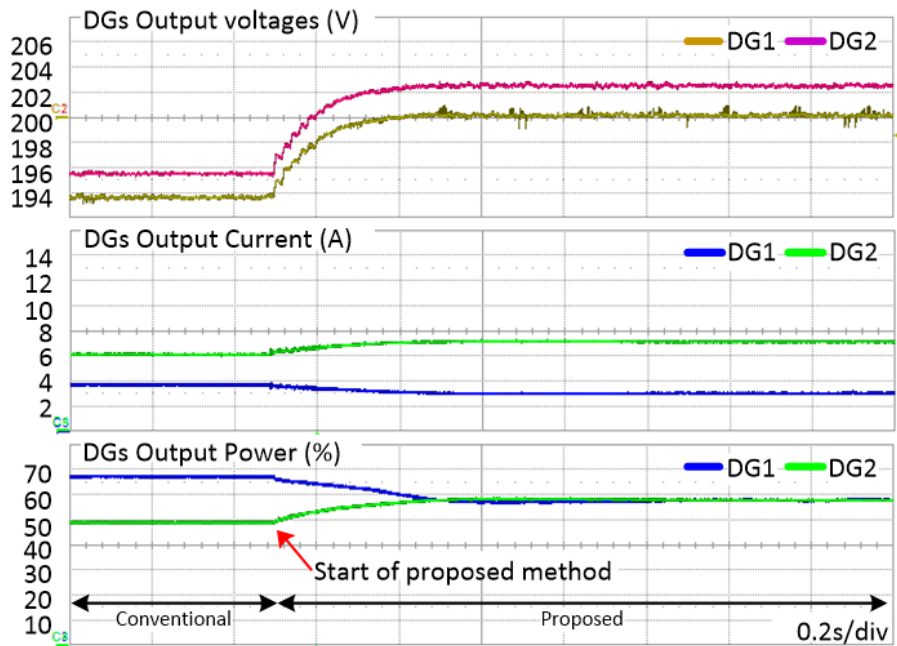


Figure 3.15: Dynamic performance of proposed method - DG outputs.

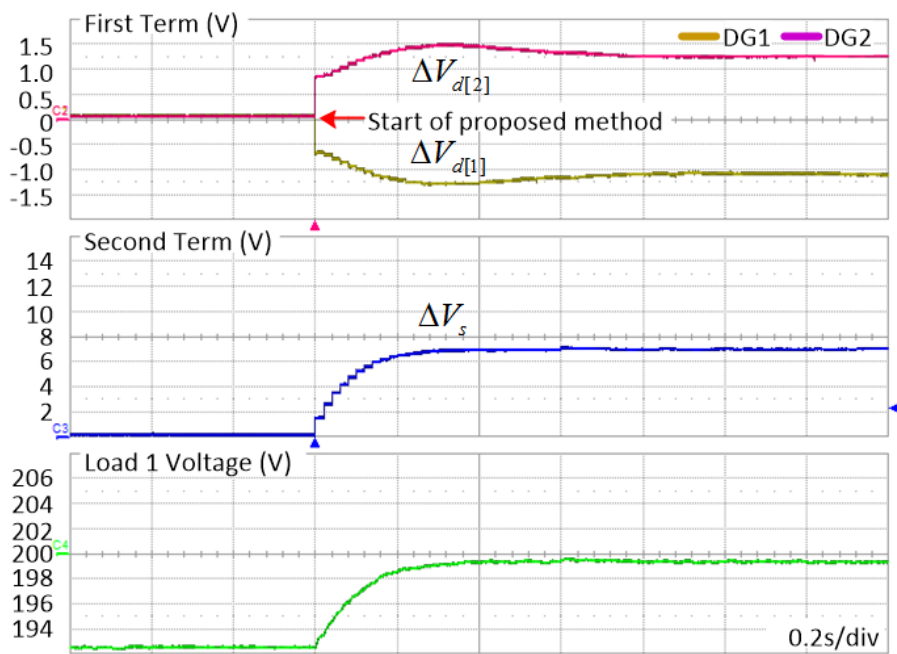


Figure 3.16: Dynamic performance of proposed method - DG shifted voltage and load 1 voltage.

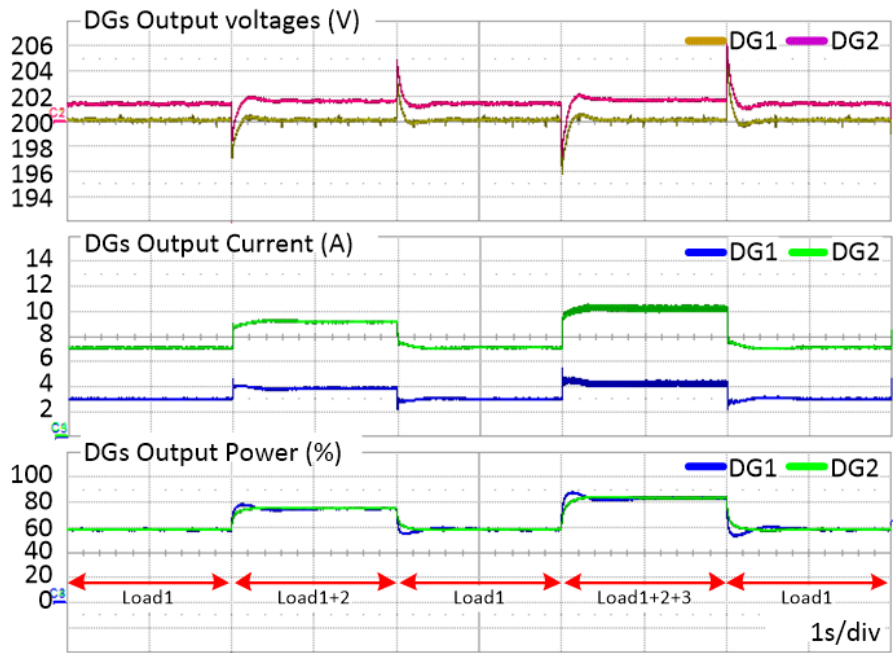


Figure 3.17: Performance of proposed method in case of load change - DG outputs.

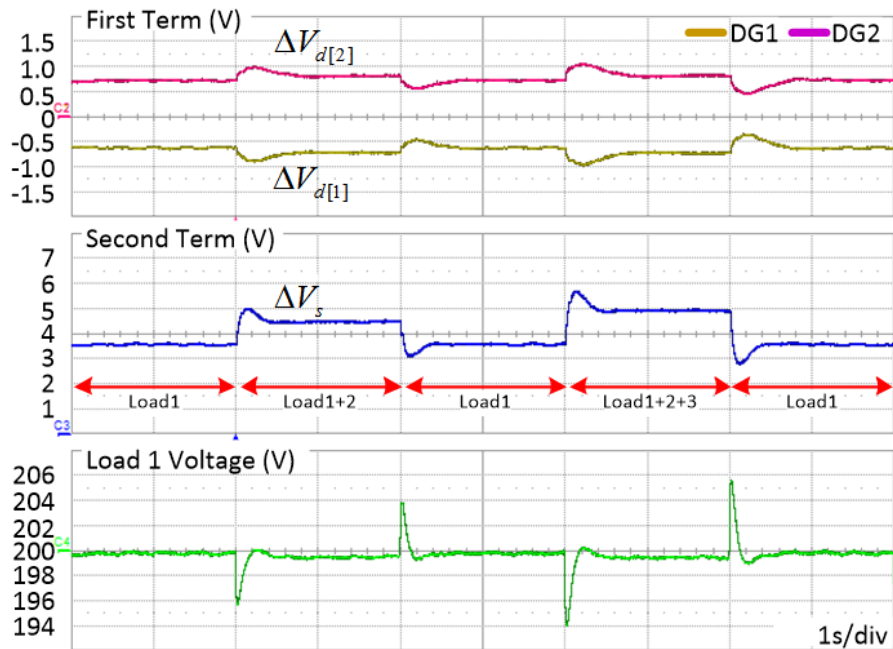


Figure 3.18: Performance of proposed method in case of load change - DG shifted voltage terms and load 1 voltage.

the simulation results. It is also clear that the proposed control method can accurately achieve proportional load power sharing and DC bus voltage restoration.

### **3.5 Summary**

In this chapter, a new voltage distributed control method was developed by introducing a novel voltage shift technique. The shifted voltages were obtained by considering the voltage drops throughout the distribution system to generate the DG's output reference voltage. By using the proposed shifted voltage technique, the voltage drop caused by the droop controller was effectively compensated to restore the DC bus voltage as well as to achieve accurate proportional load power sharing. Furthermore, the system cost is reduced because the proposed control scheme can be realized with a low-bandwidth DCL, which is used to share all information between DGs.

This chapter also offered design guidelines to implement a reliable DC microgrid system with high performance, and good power quality, as well as a system stability analysis. The effectiveness of the proposed control method was verified by simulation and an experiment with a  $2.8kW$  prototype. The simulation and experimental results verify that the DC bus voltage is restored to its nominal voltage and that proportional load power sharing is achieved regardless of the load variation.

# Chapter 4

## Dynamic Power Sharing for Transient Current

In previous chapter, the voltage deviation and power sharing problems in steady state are solved. In this chapter, the problem of transient current compensation is taken into account as dynamic power quality problem. A supercapacitor is utilized to supply or absorb the spike current within DC microgrid to improve the dynamic power quality. The local controller is controlled to share power between DGs and SC so that the SC handles the high frequency current while the DG handles the low frequency current. A typical DC microgrid with SC units is connected to common DC bus via a DC-DC converter is shown in Fig. 4.1.

In this chapter, an adaptive virtual impedance control method is proposed to control the SC converter to compensate the transient current in DC microgrid under load change condition. However, this control method cannot support the DGs under pulsed load condition. To overcome this condition, a droop based control method for SC is also proposed. By supplying the short term mismatch power between source and load, the

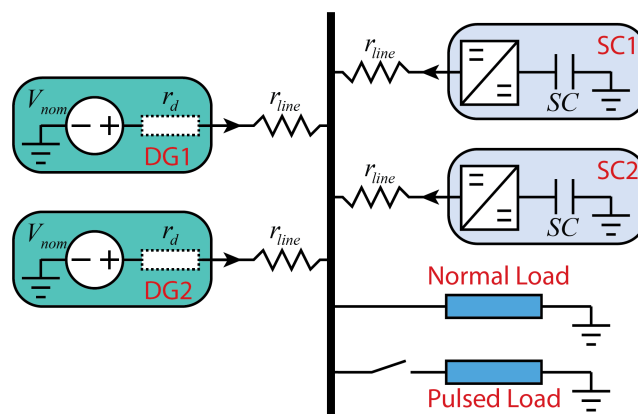


Figure 4.1: Typical configuration of a DC microgrid including SC units.

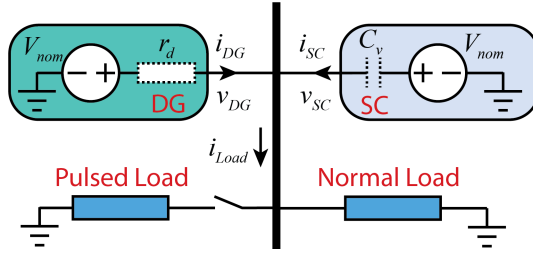


Figure 4.2: Equivalent circuit of DC microgrid with VCM.

droop based control method can compensate the pulsed load current to improve the dynamic power quality in DC microgrid.

## 4.1 Adaptive Virtual Impedance Control Method for Supercapacitor

This section presents a new control method for Supercapacitor (SC) to compensate the transient for the distributed generation in DC microgrid. The SC unit converter is controlled so that it is modeled as a constant voltage source in series with a capacitor in parallel with a resistor. The value of the resistor is adjusted according to the level of the SC voltage; it becomes negative to charge the SC when SC voltage is lower its nominal value; and become positive to discharge the SC when the SC voltage is higher its nominal value. The power sharing between SC units is ensure by the meaning of virtual impedance control method. Simulation result is carried out to show the effectiveness of proposed control method.

### 4.1.1 System Configuration and Conventional Virtual Capacitance Control Method

A typical DC microgrid including the SC units is shown in Fig. 4.1, where the sources and loads are connected to a common DC bus. The SC units are used to compensate the transient current for DG units. For SC units in microgrid, virtual capacitance control method is generally used to compensate the transient current for DGs. The DC microgrid controlled by conventional droop controller and VCM can be model as in Fig. 4.2.

As described in chapter 4.2, the relationship between output voltage and current of DG can be expressed as

$$v_{DG} = V_{nom} - r_d i_{DG}, \quad (4.1)$$

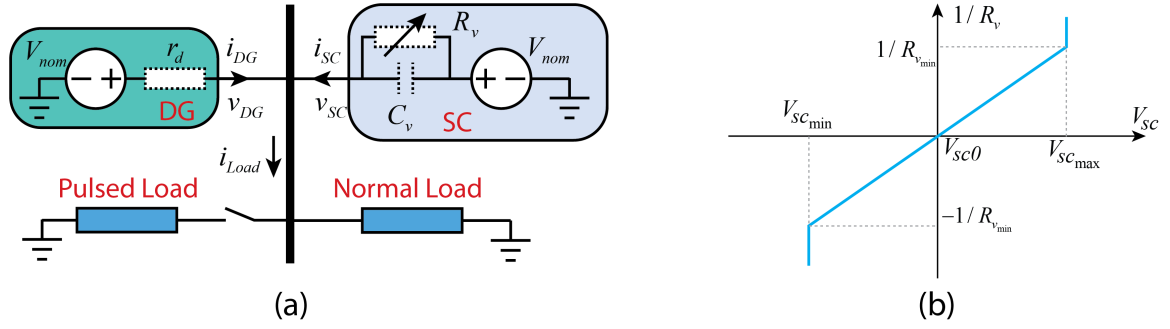


Figure 4.3: Proposed control method (a) Equivalent circuit, (b) Virtual resistance lookup curve.

and for the SC unit

$$v_{SC} = V_{nom} - \frac{1}{C_v s} i_{SC}. \quad (4.2)$$

As the load variation and power losses on the converter, the SC voltage will reduce by the time of SC unit operating. To recover the SC voltage, an additional control loop is added and the operation of SC unit is interrupted when this control loop is enable.

## 4.1.2 Proposed Adaptive Virtual Impedance Control Method

### 4.1.2.1 Proposed Control Method

As shown in Fig. 4.3(a), the proposed adaptive virtual impedance control method (AVICM) is modeled as a constant voltage source in series with a capacitor and resistor in parallel. The resistor  $R_v$  value is depend on the SC voltage level as shown in Fig. 4.3(b). When the SC voltage  $V_{sc}$  is higher than its nominal value  $V_{sc0}$ , the value of  $R_v$  becomes positive to discharge the SC. When SC voltage is lower than its nominal value, the value of  $R_v$  becomes negative to charge the SC. The value of  $R_v$  is calculated as

$$\frac{1}{R_v} = \frac{1}{R_{v_{min}}} \cdot \frac{V_{sc} - V_{sc0}}{V_{sc_{max}} - V_{sc0}} \quad (4.3)$$

where  $R_{v_{min}}$  is minimum value of  $R_v$ ,  $v_{sc_{max}}$  and  $v_{sc_{min}}$  are the maximum and minimum value of SC voltage, the nominal voltage of SC  $V_{sc0} = (V_{sc_{min}} - V_{sc_{max}})/2$ . The value of  $R_{v_{min}}$  decides the speed of SC voltage recovering. The output voltage of the SC unit converter is expressed as

$$v_{SC} = V_{nom} - i_{SC} \frac{1}{C_v s + 1/R_v}. \quad (4.4)$$

When the SC voltage reaches its nominal value, the value of  $R_v$  becomes  $1/R_v = 0$  or  $R_v = \infty$ , sot that the virtual resistor is neglected in this case. The total value of virtual

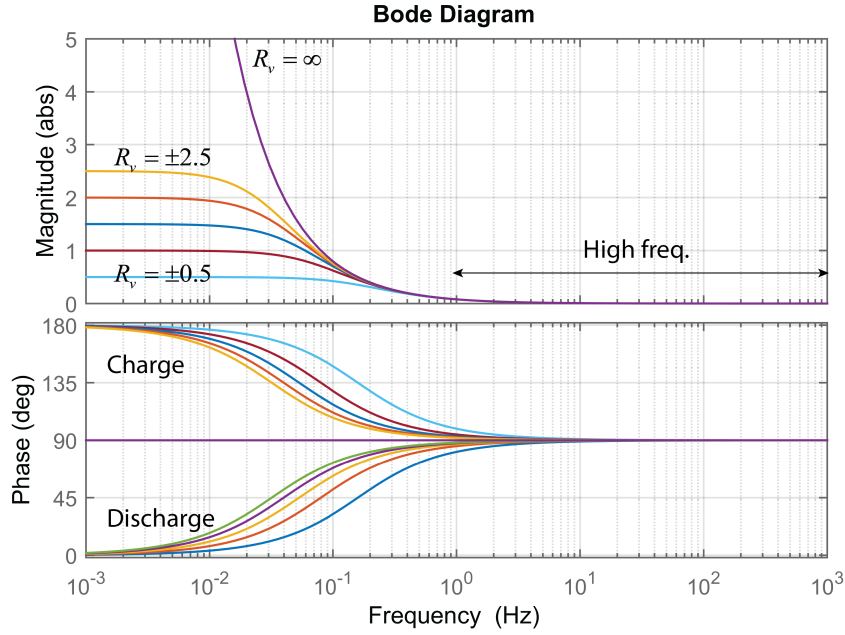


Figure 4.4: Bode diagram of virtual impedance of proposed method.

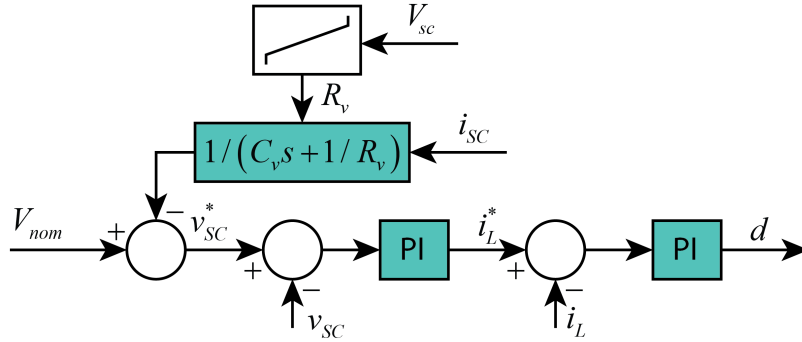


Figure 4.5: Control diagram of proposed method.

impedance is plotted as in Fig. 4.4 with the value of  $C_v = 2F$ , and  $R_v = \pm 0.5 \rightarrow \infty$ . It shows that the virtual impedance becomes  $R_v$  at low frequency range and 0 at high frequency range. As a result, the only high frequency component is absorbed by the SC unit while the low frequency component is charged or discharged to the SC by the value of virtual resistor  $R_v$  to recover its SC voltage .

#### 4.1.2.2 Controller Design

The control diagram is shown in Fig. 4.5, which consists of three control loops: inner current loop, inner voltage loop and outer SC voltage control loop. The inner current and voltage control loops design can be referred to chapter 4.2 - section 3. For the outer



adaptive virtual impedance, the value of the  $C_v$  and  $R_{v_{min}}$  must be decided. The value of the  $C_v$  decides the cut-off frequency  $\omega_c$  of the sharing current between DG and SC units. Relating to section 4.2.1, the cut-off frequency  $\omega_c$  is calculated as

$$\omega_c = \frac{1}{r_d C_v} \quad (4.5)$$

where  $r_d$  is equivalent droop coefficient of all DG. Therefore, by deciding the cut-off frequency  $\omega_c$ , the value of virtual capacitance  $C_v$  can be calculated as

$$C_v = \frac{1}{r_d \omega_c} \quad (4.6)$$

The minimum value of the  $R_{v_{min}}$  decides the maximum charging or discharging current of SC unit. It is calculated based on the rated current of the SC converter as

$$MIN(R_{v_{min}}) = \frac{V_{nom} - V_{min}}{I_{sc_{rated}}} \quad (4.7)$$

where  $I_{sc_{rated}}$  is rated current of SC converter. Therefore, the value of  $R_{v_{min}}$  cannot be smaller than the value in (4.7). More larger value of  $R_{v_{min}}$ , the slower recovery of SC voltage be.

### 4.1.3 Simulation Results

Table 4.1: Parameters used in simulation

Parameters	Symbol	Value
<i>DC Microgrid Parameters</i>		
Bus voltage	$V_{bus}$	45 – 48V
Rated current	$I_{DG}$	8A
Normal load		12Ω
Pulsed load		10Ω
<i>SC Converter</i>		
SC	$C_{sc}, R_{sc}$	2F, 4F, 0.01Ω
Output capacitor	$C_o$	4400μF
Inductor	$L$	0.3mH
Output line impedance	$R_{line}$	0.01Ω
Switching frequency	$f_s$	20kHz

A DC Microgrid as shown in Fig. 4.1 with two DG and two SC units is simulated by PSIM to verify the performance of proposed method. The parameters of DC microgrid,

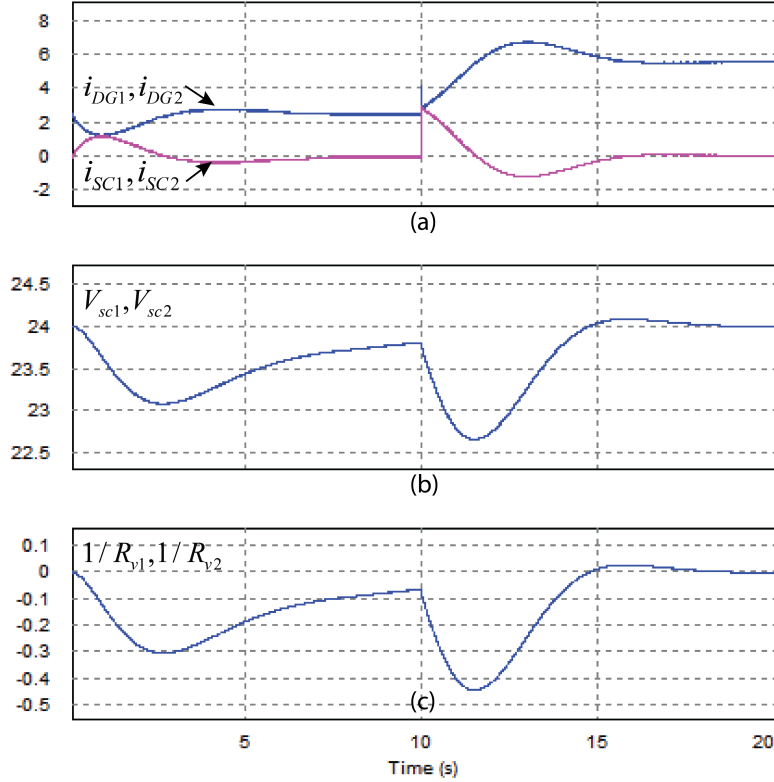


Figure 4.6: Simulation result - two SC units have same parameters.

DC-DC converters, and controllers are shown in table 4.1. A load of  $10\Omega$  is connected to DC at the moment of 10s to test the performance of the proposed method.

To verify the performance of proposed control method, two SC units are controlled and configured with same parameters as  $C_{v1} = C_{v2} = 1$ ,  $R_{v1min} = R_{v2min} = 0.5$ , the initial voltage of two SC units is 24V and they have same capacity of  $4F$ . The simulation result is shown in Fig. 4.6. Sharing current between DGs and SC units is shown in Fig. 4.6(a), it shows that the output currents of two SC units are the same. The SC voltage is reduced when the load is connected and then recovered to 24V as in Fig. 4.6(b). The value of  $1/R_{v1}$  and  $1/R_{v2}$  are adjusted according to the SC voltage as shown in Fig. 4.6(c). It becomes zero when the SC voltage reach its nominal value at 24V.

In the condition of different capacity of the SC as  $C_{sc1} = 2F, C_{sc2} = 4F$ , the performance of proposed method is verified as: case I: they have same value of minimum resistance as  $R_{v1min} = R_{v2min} = 0.5$ ; case II: the value of minimum resistance as  $R_{v1min} = 1, R_{v2min} = 0.5$ . Fig. 4.7 shows the simulation results of case I. The current sharing becomes unbalanced between SC units as shown in Fig. 4.7(a). The SC voltage restoration of SC1 have a high overshoot as shown in Fig. 4.7(b). It is the result of the different of the virtual resistance as in Fig. 4.7(c). In case II, when the minimum virtual

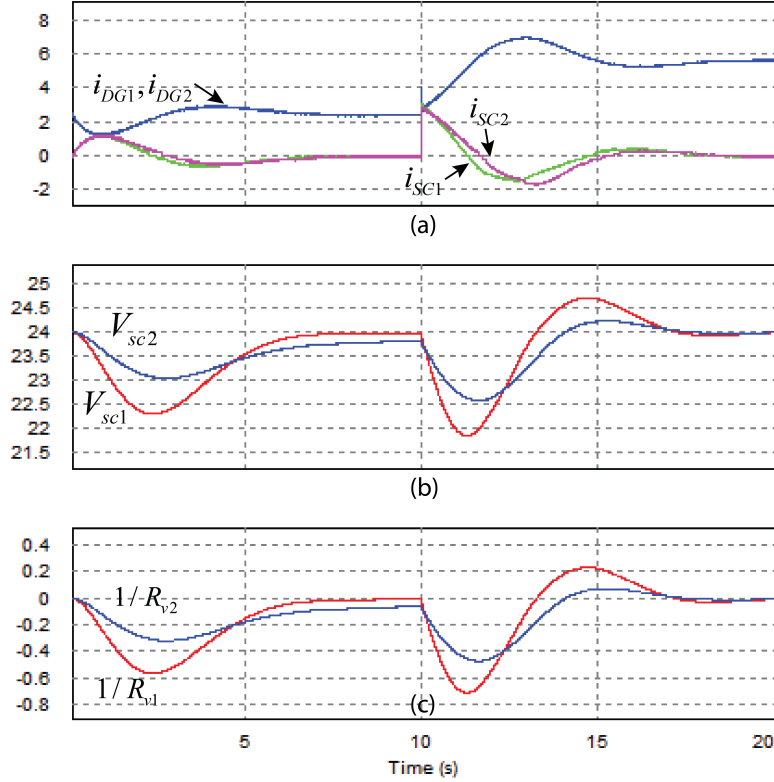


Figure 4.7: Simulation result - two SC units have different SC capacity and  $R_{v1min} = R_{v2min} = 0.5$ .

resistance is changed as  $R_{v1min} = 1, R_{v2min} = 0.5$ , the sharing current between SC is corrected as in Fig. 4.8(a) as the value of virtual resistance is identical in Fig. 4.7(c).

When the SC units have different initial SC voltage, the performance of proposed method is shown in Fig. 4.9. In the initial time, the SC2 unit has lower SC voltage, it operates in charging mode to recover its SC voltage with higher current as in Fig. 4.9(a). Finally, both SC units have same SC voltage and output current, which shows the effectiveness of proposed method in SC voltage restoration.

A final test of proposed method when the load is continuously connect and disconnect to the DC bus is carried out. The simulation results are shown in Fig. 4.10. Even though two SC units have different initial SC voltage, after a period of operating, the SC voltages of two units are recovered to nominal value and share the same amount of current in the end.

The simulation results show that the proposed method can compensate the output current of the DG at the same time with its SC voltage restoration. The proposed method also has a superior performance under different conditions such as different SC capacity, unbalance SC voltage, and continuously load changes.

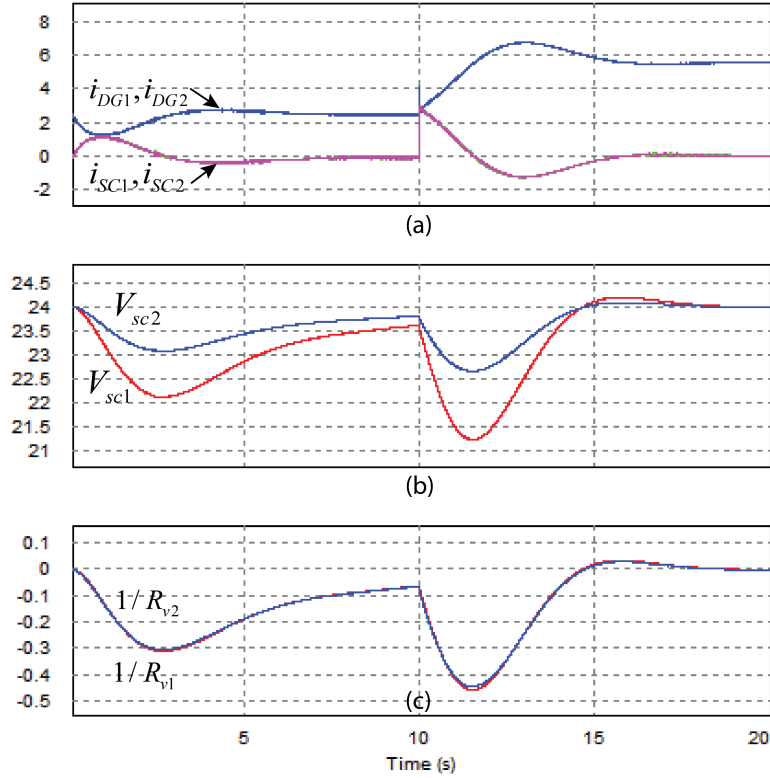


Figure 4.8: Simulation result - two SC units have different SC capacity and  $R_{v1min} = 1, R_{v2min} = 0.5$ .

#### 4.1.4 Conclusion

This section proposed an adaptive virtual impedance control method for SC unit in DC microgrid to compensate the transient current of the loads. More over, by actively adjusting the virtual impedance according to the SC voltage level, the proposed method smoothly restores the SC voltage at the same time with compensating the transient current. Based in virtual capacitance method, the SC units can operate in parallel to sharing the pulsed current; by recovering the SC voltage, the SC units in DC microgrid always have same SC voltage level to maximize the availability of the system. The proposed control method effectively operates under various condition such as different SC capacity, unbalance SC voltage, and continuously load changes. The effectiveness of the proposed method is verified by simulation results.

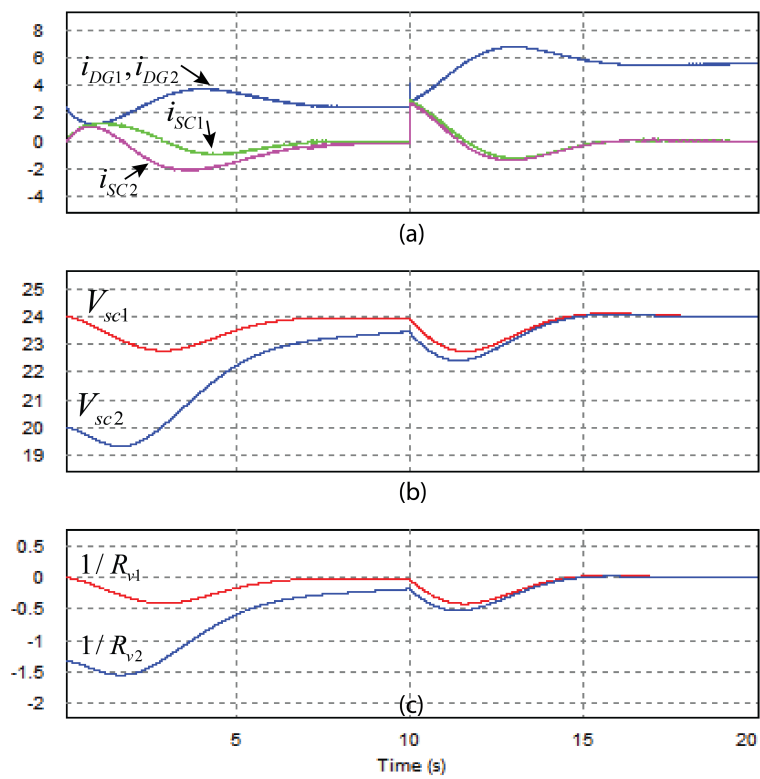


Figure 4.9: Simulation result - two SC units have different initial SC voltage.

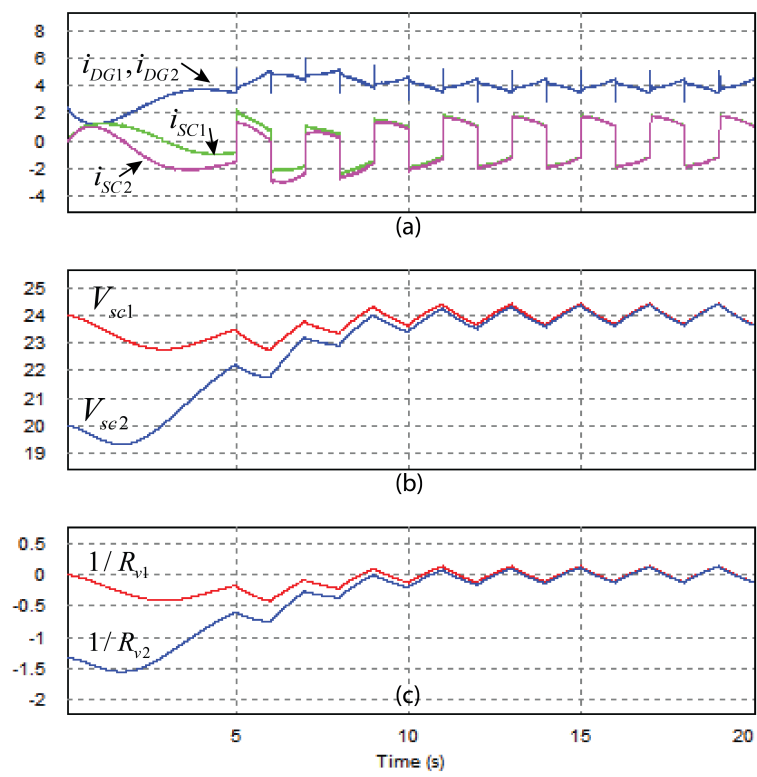


Figure 4.10: Simulation result - under continuously load changed.

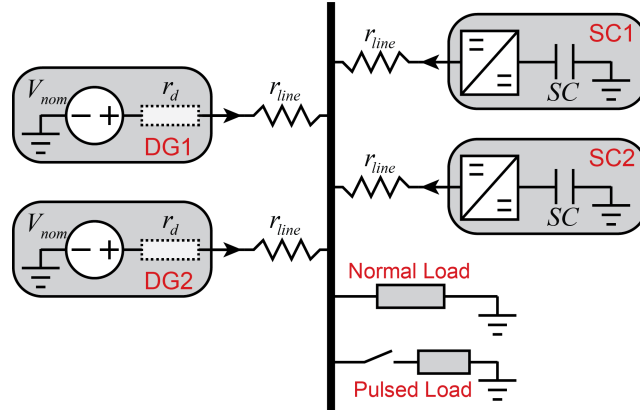


Figure 4.11: Typical configuration of a DC microgrid.

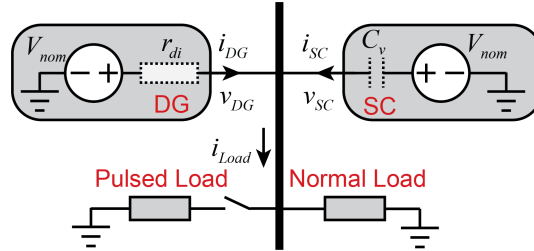


Figure 4.12: DC microgrid modeling when VCM control method is used for SC unit.

## 4.2 Compensate the Pulsed Load Current by Using Supercapacitor

In recent chapters, the pulsed load is not considered and its effect to the power quality in DC microgrid is discussed in Chapter 2. This section presents a new control method for Super-capacitor (SC) to compensate the transient load current and support the system under the pulsed load. Moreover, the cooperation of the multiple SC units in DC microgrid is also ensured by proportionally sharing the supporting current between the SC units. The current sharing between the SC units is achieved by means of the droop control concept which is innovated to adapt in SC controller. The conventional droop control is modified so that it can adaptively change its operation mode and parameters in order to compensate the load transient current and regulate the state of charge of the SC. The effectiveness of the proposed method is investigated and evaluated by an experimental DC microgrid prototype. The experimental results prove that the proposed method can achieve high performance and seamless control.

### 4.2.1 System Configuration and Conventional Control Method

A typical DC microgrid including the SC units is shown in Fig. 4.11, where the sources and loads are connected to a common DC bus. The SC units are used to compensate the mismatch current between the DGs and the loads to enhance the DC bus voltage and power supply quality. In DC microgrid, the droop control is commonly used for the load sharing among the DGs. The relationship between the output voltage and output current of a DG is expressed as:

$$v_{DG} = V_{nom} - i_{DG}r_d \quad (4.8)$$

where  $v_{DG}$  and  $i_{DG}$  are the output voltage and the current of DG, and  $r_d$  is the droop coefficient which is regarded as the virtual resistance of DG, respectively. By replacing the virtual resistance by virtual capacitance, the virtual capacitance method (VCM) is used for SC to compensate the transient current of the loads. As shown in Fig. 4.12, the conventional VCM is modeled as a voltage source connected in series with a virtual capacitor. The relationship between the output voltage and the current of SC unit is expressed as

$$v_{SC} = V_{nom} - \frac{1}{C_v s} i_{SC}, \quad (4.9)$$

where  $v_{SC}$  and  $i_{SC}$  are the output voltage and current of SC unit, and  $C_v$  is the virtual capacitance of VCM. As the droop coefficient is much higher than the line impedance, the line impedance is neglected in these following calculations. From Fig. 4.12, the output voltages and currents are expressed as

$$\begin{cases} v_{DG} &= V_{nom} - r_d i_{DG} \\ v_{SC} &= V_{nom} - \frac{1}{C_v s} i_{SC} \\ i_{Load} &= i_{DG} + i_{SC} \end{cases} \quad (4.10)$$

When the SC is used to compensate the transient loads current, the sharing currents between DGs current and SC current are obtained in (4.11) from (4.10):

$$\begin{cases} i_{DG} &= G_1(s) i_{Load} = \frac{1}{sr_d C_v + 1} i_{Load} \\ i_{SC} &= G_2(s) i_{Load} = \frac{sr_d C_v}{sr_d C_v + 1} i_{Load} \end{cases} \quad (4.11)$$

From (4.11), we can see that the loads current is shared between SC and DG by a low pass (LP) filter and a high pass (HP) filter. The low frequency component is handled by DG while the high frequency component is handled by SC. The cut-off frequency of LP



and HP filter is calculated as

$$\omega_c = \frac{1}{r_d C_v}. \quad (4.12)$$

From (4.12), the current rate change, which is affected by the cut-off frequency of LP and HP filter, depends on the droop coefficient. On other hand, the current rate change is secured by the characteristic of the DG source (such as battery, fuel cell...). However, the droop coefficient is chosen by the rated current of DG, and it can be changed by the system reconfiguration. Thus, the cut-off frequency is changed, and it affects the performance of the system.

Moreover, because the output current of the SC converter only contains the high frequency component of the load current from (4.11), the SC converter cannot supply a DC current to support the microgrid when a pulsed load is connected to the DC bus. As a result, the DC bus voltage is highly dropped because the DG converters operate under the overload condition.

In practical applications, the losses of DC-DC converters and the random connection of the loads makes the SC units operate with unbalanced power flow from the charge and discharge modes. Therefore, the SoC or SC voltage level of SC unit is not regulated after an interval of operation.

## 4.2.2 Proposed Droop Based Controller for Supercapacitor Unit

As shown in Fig. 4.13, the SC converter in our proposed method is modeled as a variable voltage source  $\tilde{V}_{SC0}$  connected in series with a resistor  $r_{dSC}$  as

$$v_{SC} = \tilde{V}_{SC0} - r_{dSC} i_{SC}. \quad (4.13)$$

The SC converter controls to compensate the load transient current and the SC state of charge (SoC) simultaneously; the objective of the proposed method is compensating the load transient current as well as regulating the SoC of SC. The droop coefficient of SC converter is chosen to be very small compared with the droop coefficient of DG converter. From Fig. 4.13(a), the output current of DG and SC are given as follows:

$$\begin{cases} i_{DG} = i_l \frac{r_{dSC}}{r_d + r_{dSC}} + \frac{V_{nom} - \tilde{V}_{SC0}}{r_d + r_{dSC}} \\ i_{SC} = i_l \frac{r_d}{r_d + r_{dSC}} - \frac{V_{nom} - \tilde{V}_{SC0}}{r_d + r_{dSC}} \end{cases} \quad (4.14)$$

where  $i_l$ ,  $i_{DG}$  and  $i_{SC}$  are the load current, DG and SC output currents, respectively. From (4.14), as  $r_{dSC}$  is very small compared with  $r_d$ , the high frequency component of  $i_l$  much reduces its effect on the DG current  $i_{DG}$  because  $r_{dSC}/(r_d + r_{dSC})$  is neglectable. Hence,

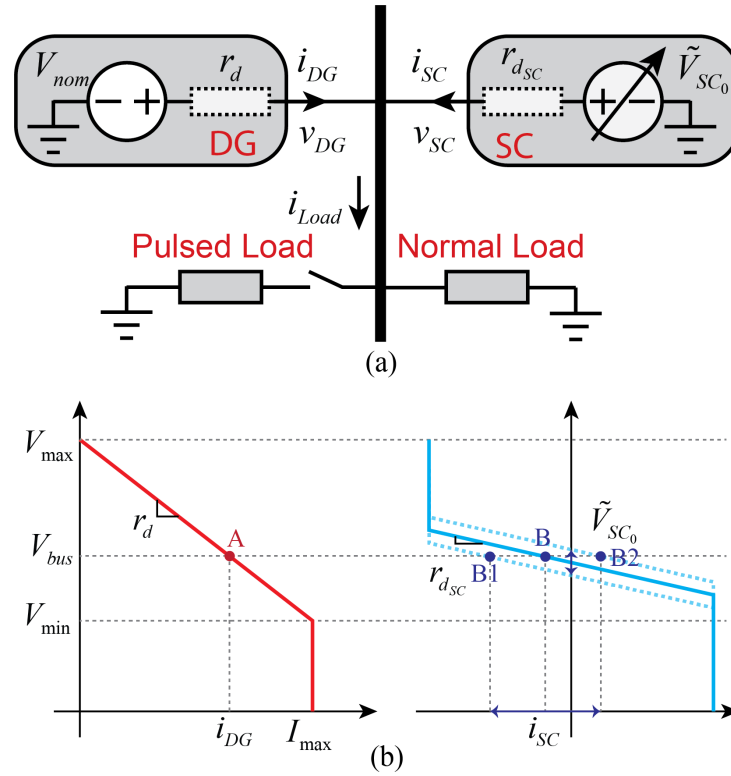


Figure 4.13: Proposed control method (a) DC microgrid equivalent circuit and (b) droop curve.

the output current of DG is dependent on the variable voltage source  $\tilde{V}_{SC_0}$ . On the other hand, the output current of the SC converter has only high frequency component of the load current  $i_l$  as the ratio  $r_d/(r_d+r_{d_{SC}})$  is approximated as unity. Therefore, by properly controlling the variable voltage  $\tilde{V}_{SC_0}$ , the load current can be shared between DG and SC based on the frequency range.

The SoC of SC is indicated by the SC voltage level. So, by regulating the SC voltage  $v_{SC}$ , the SoC of SC is also guaranteed at nominal level. In this section, the nominal operation point of SoC is 70% which is regarded as the SC voltage level at  $v_{SC}^*$ . For illustrating the operation of the proposed method, the droop curves of DG and SC converter are shown in Fig. 4.13 (b). Initial, the operation point of DG is at point A and the SC is at point B. If the SoC of the SC is higher than rated level, the value of  $\tilde{V}_{SC}$  is adjusted slowly so that the operation point of SC is changed to B2, where the SC operates at discharge mode. In vice versus, if the SoC of SC is lower than rated level, the operation point of SC is slowly changed to B1 where the SC operates in charge mode. Therefore, the SoC of SC can be automatically restored. Moreover, by using droop control, multiple SC converter can operate normally.

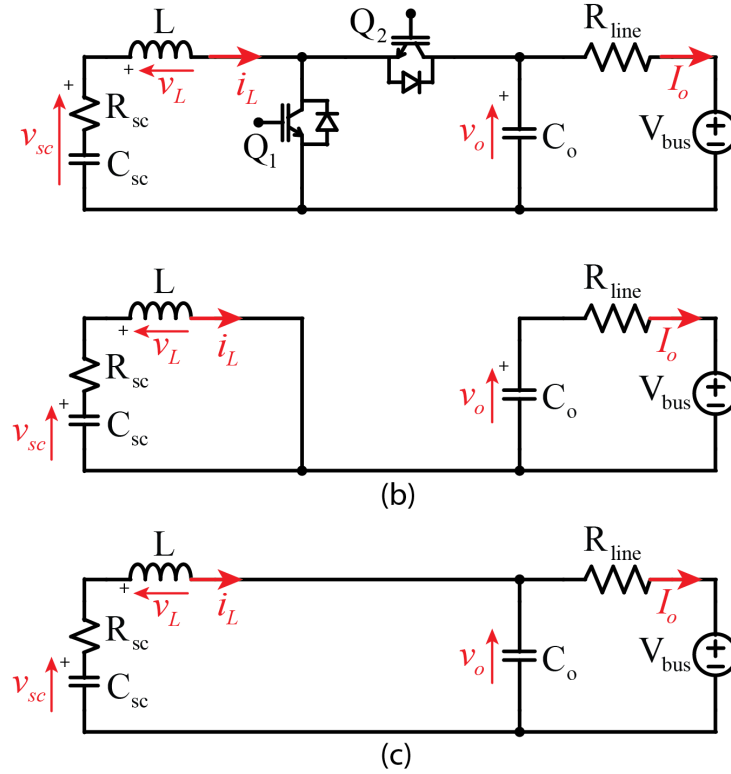


Figure 4.14: (a) Bidirectional Buck-Boost Converter, (b) State 1 – Q1 ON and Q2 OFF, and (c) State 2 – Q1 OFF and Q2 ON.

## 4.2.3 Small Signal Modeling and Controller Design

### 4.2.3.1 Converter Modeling

A bidirectional buck-boost converter (BBBC) is used to connect the SC to the DC bus as shown in Fig. 4.14(a). In a BBBC, switches  $Q_1$  and  $Q_2$  are complimentary to each other and there are only two sub-intervals of power state: State 1 ( $Q_1$  ON and  $Q_2$  OFF) and State 2 ( $Q_1$  OFF and  $Q_2$  ON) as shown in Fig. 4.14(b) and (c). From Fig. 4.14(b) of the state 1 when  $Q_1$  is ON and  $Q_2$  is OFF, the power state equations in state 1 can be expressed as

$$\frac{dv_o}{dt} = -\frac{1}{C_o} I_o = -\frac{1}{C_o R_{line}} (v_{C_o} - V_{bus}), \quad (4.15)$$

$$\frac{di_L}{dt} = \frac{v_{sc}}{L} - \frac{R_{sc}}{L} i_L, \quad (4.16)$$

$$\frac{dv_{sc}}{dt} = -\frac{i_L}{C_{sc}} \quad (4.17)$$

where  $v_{C_o}$ ,  $v_{sc}$  and  $i_L$  are output voltage, SC voltage and inductor current of the converter. The state equations in (4.15) (4.16) and (4.17) can be rewritten as (4.18).

$$\dot{X} = \begin{bmatrix} \dot{v}_o \\ \dot{v}_{sc} \\ \dot{i}_L \end{bmatrix} = \begin{bmatrix} -\frac{1}{C_{oline}} & 0 & 0 \\ 0 & 0 & -\frac{1}{C_{sc}} \\ 0 & \frac{1}{L} & -\frac{R_{sc}}{L} \end{bmatrix} \begin{bmatrix} v_o \\ v_{sc} \\ i_L \end{bmatrix} + \begin{bmatrix} \frac{1}{C_o R_{line}} \\ 0 \\ 0 \end{bmatrix} [V_{bus}]. \quad (4.18)$$

In state 2 as in Fig. 4.14(c), when Q1 is OFF and Q2 is ON, the power state equations are obtained as

$$\frac{dv_{C_o}}{dt} = \frac{1}{C_o} i_L - \frac{1}{C_o R_{line}} (v_{C_o} - V_{bus}), \quad (4.19)$$

$$\frac{di_L}{dt} = -\frac{1}{L} v_{C_o} + \frac{v_{sc}}{L} - \frac{R_{sc}}{L} i_L, \quad (4.20)$$

$$\frac{dv_{sc}}{dt} = -\frac{i_L}{C_{sc}}. \quad (4.21)$$

And they can be rewritten as (12).

$$\dot{X} = \begin{bmatrix} \dot{v}_{C_o} \\ \dot{v}_{SC} \\ \dot{i}_L \end{bmatrix} = \begin{bmatrix} -\frac{1}{C_o R_{line}} & 0 & \frac{1}{C_o} \\ 0 & 0 & -\frac{1}{C_{SC}} \\ -\frac{1}{L} & \frac{1}{L} & -\frac{R_{SC}}{L} \end{bmatrix} \begin{bmatrix} v_{C_o} \\ v_{SC} \\ i_L \end{bmatrix} + \begin{bmatrix} \frac{1}{C_o R_{line}} \\ 0 \\ 0 \end{bmatrix} [V_{bus}]. \quad (4.22)$$

By using averaged large signal model, the state of the converter can be expressed as

$$\dot{X} = \begin{bmatrix} \dot{v}_{C_o} \\ \dot{v}_{SC} \\ \dot{i}_L \end{bmatrix} = \begin{bmatrix} -\frac{1}{C_o R_{line}} & 0 & \frac{1-D}{C_o} \\ 0 & 0 & -\frac{1}{C_{SC}} \\ -\frac{1-D}{L} & \frac{1}{L} & -\frac{R_{SC}}{L} \end{bmatrix} \begin{bmatrix} v_{C_o} \\ v_{SC} \\ i_L \end{bmatrix} + \begin{bmatrix} \frac{1}{C_o R_{line}} \\ 0 \\ 0 \end{bmatrix} [V_{bus}]. \quad (4.23)$$

where  $D$  is duty cycle of the converter. For constructing small signal model, the delta terms are aggregated in (4.23) and the result is obtained as

$$\frac{\hat{X}(s)}{\hat{d}(s)} = (sI - A)^{-1} ((A_1 - A_2) \bar{X} + (B_1 - B_2) \bar{U}_i), \quad (4.24)$$

where  $\bar{X}$  is averaged value of  $X$ ,  $\bar{U}_i$  is averaged value of  $U_i$ , and

$$A = \begin{bmatrix} -\frac{1}{C_o R_{line}} & 0 & \frac{1-D}{C_o} \\ 0 & 0 & -\frac{1}{C_{SC}} \\ -\frac{1-D}{L} & \frac{1}{L} & -\frac{R_{SC}}{L} \end{bmatrix}, \quad B = \begin{bmatrix} \frac{1}{C_o R_{line}} \\ 0 \\ 0 \end{bmatrix} \quad (4.25)$$

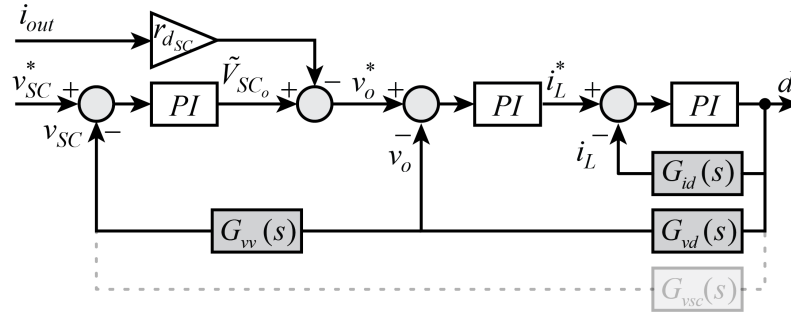


Figure 4.15: Control diagram of proposed method.

$$A_1 = \begin{bmatrix} -\frac{1}{C_o R_{line}} & 0 & 0 \\ 0 & 0 & -\frac{1}{C_{sc}} \\ 0 & \frac{1}{L} & -\frac{R_{sc}}{L} \end{bmatrix}, A_2 = \begin{bmatrix} -\frac{1}{C_o R_{line}} & 0 & \frac{1}{C_o} \\ 0 & 0 & -\frac{1}{C_{sc}} \\ -\frac{1}{L} & \frac{1}{L} & -\frac{R_{sc}}{L} \end{bmatrix} \quad (4.26)$$

$$B_1 = B_2 = \begin{bmatrix} \frac{1}{C_o R_{line}} \\ 0 \\ 0 \end{bmatrix}. \quad (4.27)$$

Note that for the SC application in DC microgrid, the  $I_o$  remains zero in steady state, the SC voltage  $v_{sc}$  should be keep in nominal value  $V_{sc0}$ . Then, the duty to inductor current  $G_{id}(s)$  and duty to output voltage  $G_{vd}(s)$  are obtained a

$$G_{id}(s) = \frac{V_{bus} C_{sc} s (C_o R_{line} s + 1)}{C_o C_{sc} L R_{line} s^3 + (C_o C_{sc} R_{line} R_{sc} + C_{sc} L) s^2 + (C_o R_{line} + C_{sc} R_{line} + C_{sc} R_{sc} + C_{sc} D^2 R_{line} - 2C_{sc} D R_{line}) s + 1}, \quad (4.28)$$

$$G_{vd}(s) = \frac{V_{bus} C_{sc} R_{line} (1 - D) s}{C_o C_{sc} L R_{line} s^3 + (C_o C_{sc} R_{line} R_{sc} + C_{sc} L) s^2 + (C_o R_{line} + C_{sc} R_{line} + C_{sc} R_{sc} + C_{sc} D^2 R_{line} - 2C_{sc} D R_{line}) s + 1}, \quad (4.29)$$

$$G_{vsc}(s) = -\frac{V_{bus} (C_o R_{line} s + 1)}{C_o C_{sc} L R_{line} s^3 + (C_o C_{sc} R_{line} R_{sc} + C_{sc} L) s^2 + (C_o R_{line} + C_{sc} R_{line} + C_{sc} R_{sc} + C_{sc} D^2 R_{line} - 2C_{sc} D R_{line}) s + 1}. \quad (4.30)$$

#### 4.2.3.2 Inner Controller Design

The calculated of the BBBC model is used to design the proposed controller in Fig. 4.15. There are four control loops: inner current loop, inner voltage loop, droop control, and SC voltage control loop.

##### *Inner inductor current control loop*

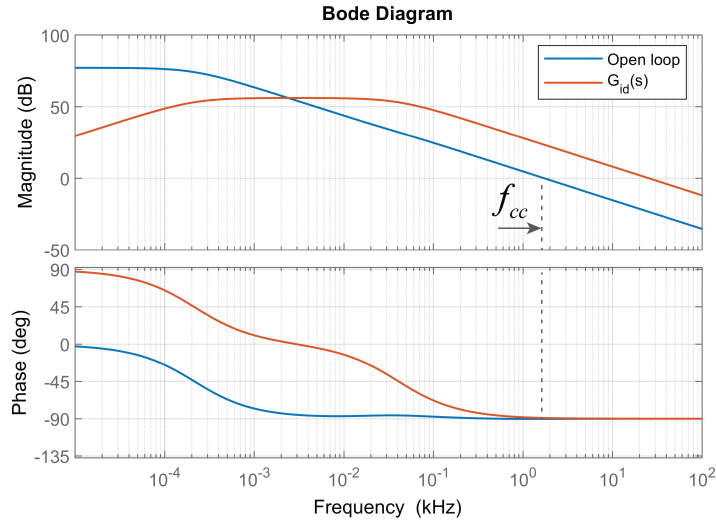


Figure 4.16: Bode diagram of the inner current control loop.

The inner inductor current loop can be expressed as

$$(i_L^* - i_L) \left( k_{Pc} + \frac{k_{Ic}}{s} \right) G_{id}(s) = i_L, \quad (4.31)$$

where  $i_L^*$  and  $i_L$  are reference and actual inductor current,  $k_{Pc}$  and  $k_{Ic}$  are PI gains of current controller. The cut-off frequency  $f_{cc}$  of the current loop is smaller than 1/10 of switching frequency  $f_s$  with infinity of gain margin and 75° of phase margin. By using SISO toolbox, the gains of the PI controller are selected as  $k_{Pc} = 0.0676$  and  $k_{Ic} = 15.031$  and the bode diagram of inner current loop is plotted in Fig. 4.16.

#### **Inner output voltage control loop**

From (4.28) and (4.29), the transfer function of voltage over inductor current  $G_{vi}(s)$  can be obtained as:

$$G_{vi}(s) = G_{vd}(s)/G_{id}(s) = \frac{R_{line}(1-D)}{R_{line}C_o s + 1} \quad (4.32)$$

From Fig. 4.15, the inner output voltage control loop can be expressed as

$$(v_o^* - v_o) \left( k_{Pv} + \frac{k_{Iv}}{s} \right) T_{CC} G_{vi} = v_o, \quad (4.33)$$

where  $v_o^*$  and  $v_o$  are reference and actual output voltage,  $k_{Pv}$  and  $k_{Iv}$  are PI gains of output voltage controller,  $T_{CC}$  is gain of closed inner inductor current control loop. To design the voltage loop controller, the gain of  $T_{CC}$  is considered as unity as its bandwidth is much higher than the voltage control loop. By using SISO toolbox, the gains of the PI controller are selected as  $k_{Pc} = 20.216$  and  $k_{Ic} = 26.955$  and the bode diagram of inner

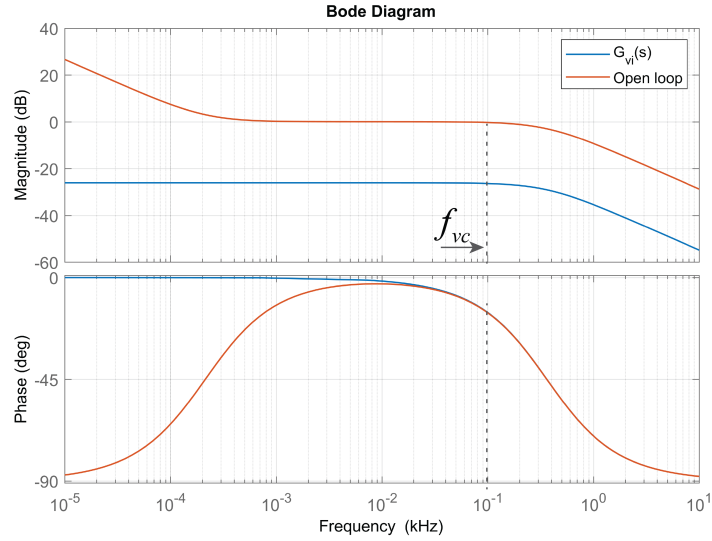


Figure 4.17: Bode diagram of the inner voltage control loop.

current loop is plotted in Fig. 4.17.

#### **Outer SC voltage control loop**

The outer SC voltage control loop is used to restore the SC voltage. The control loop can be described as

$$\left( (V_{sc}^* - v_{sc}) \left( k_{Psc} + \frac{k_{Isc}}{s} \right) - i_{out} r_{dsc} \right) T_{VC} G_{vv} = v_{sc} \quad (4.34)$$

where  $k_{Psc}$  and  $k_{Isc}$  are PI gains of the SC voltage controller,  $T_{VC}$  is closed loop gain of voltage control loop, and  $G_{vv}$  is the output voltage to SC voltage transfer function. The  $G_{vv}$  can be obtained as

$$G_{vv}(s) = \frac{G_{vsc}(s)}{G_{vd}(s)} = -\frac{C_o R_{line} s + 1}{C_{sc} R_{line} (1 - D) s} \quad (4.35)$$

The gain of  $T_{VC}$  can be seen as unity when design the SC voltage loop. The gains of PI controller can be obtained by using SISO toolbox,  $k_{Psc} = 7.912$  and  $k_{Isc} = 0.08157$  for cut-off frequency at 2.5Hz and  $90^\circ$  of phase margin. The bode diagram of SC voltage control loop is shown in Fig. 4.18.

### **4.2.4 Simulation Results**

A DC Microgrid as shown in Fig. 4.11 with one DG and two SC units is simulated by PSIM to verify the performance of proposed method. The parameters of DC microgrid, DC-DC converters, and controllers are shown in table 4.2. A pulsed load of  $8\Omega$  is connected to

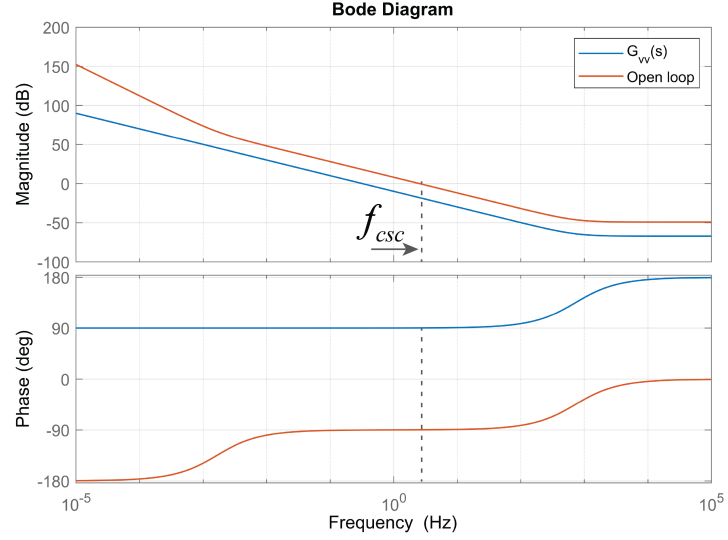


Figure 4.18: Bode diagram of the SC voltage control loop.

Table 4.2: Parameters used in simulation

Parameters	Symbol	Value
<i>DC Microgrid Parameters</i>		
Bus voltage	$V_{bus}$	45 – 48V
Rated current	$I_{DG}$	8A
Normal load		12 $\Omega$
Pulsed load		8 $\Omega$
<i>SC Converter</i>		
SC	$C_{sc}, R_{sc}$	4F, 0.01 $\Omega$
Output capacitor	$C_o$	4400 $\mu$ F
Inductor	$L$	0.3mH
Output line impedance	$R_{line}$	0.01 $\Omega$
Switching frequency	$f_s$	20kHz



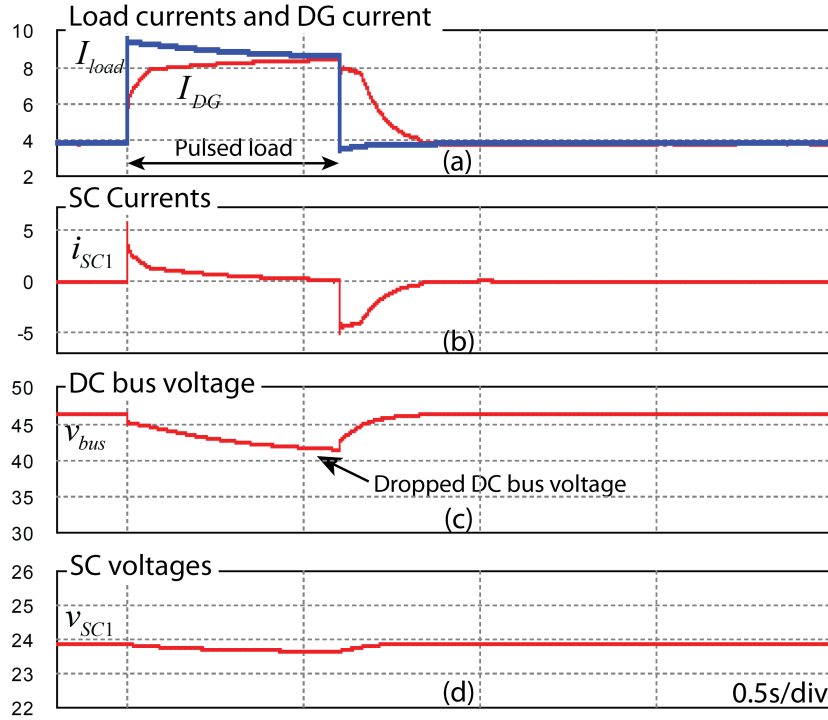


Figure 4.19: Simulation result of conventional VC method under pulsed load.

DC bus in short interval of 0.6s to verify the performance of proposed method.

To compare with conventional virtual capacitor method, one SC converter is controlled by both proposed method and conventional VC method. Fig. 4.19 and Fig. 4.20 show the simulation results of conventional VC and proposed method under pulsed load. It shows that proposed method has same performance with conventional VC method at the transient moment to cut the peak current for the DG. However, when the DG cannot supply the peak current for the pulsed load as in Fig. 4.19(a) because it cannot supply the DC current to support mismatch current of pulsed load as Fig. 4.19(b), the DC bus voltage in Fig. 4.19(c) is significantly dropped. Moreover, the DG output current is greater than 8A, which means that DG operated in overload condition in this case. By applying proposed method, the output current of DG is limited at 8A as shown in Fig. 4.20(a), the mismatched current is supplied by SC converter as in Fig. 4.20(b). As a result, the DC bus is regulated and kept within 45-48V. Moreover, the SC voltage is controlled to recover to its nominal value as shown in Fig. 4.20(d).

For evaluating parallel operation of proposed method, two SC converter is activated. Fig. 4.21 shows the performance of proposed method when the cut-off frequency of SC voltage control loop is 2.5Hz in (a) and 6.62Hz in (b). It shows that the settling time and recovery speed of SC voltage in Fig. 4.21(a) are slower than in Fig. 4.21(b). With same droop coefficient, the current sharing between two SC converters are exactly same. With

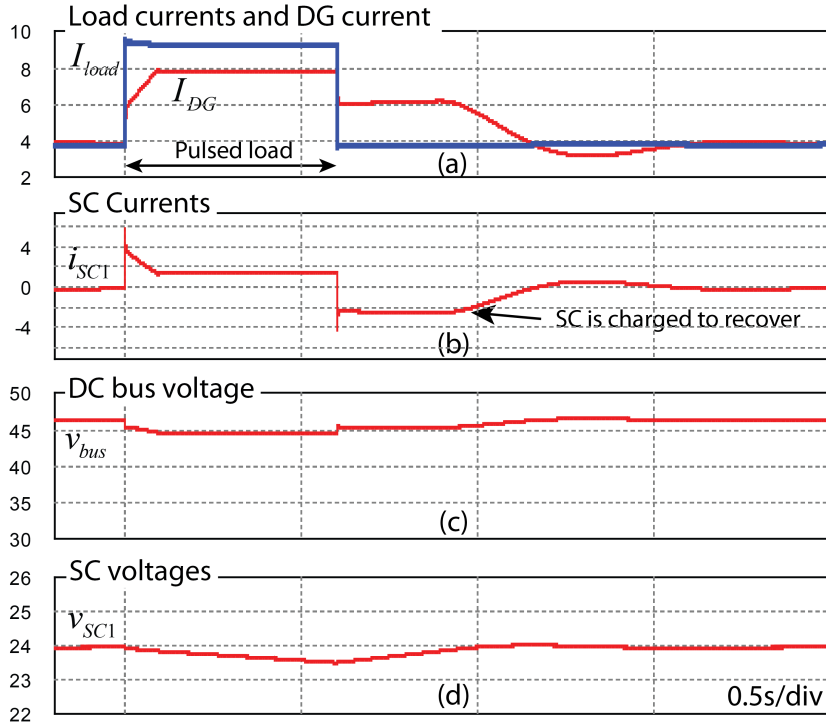


Figure 4.20: Simulation result of proposed method under pulsed load.

different droop coefficient as  $r_{dsc1} = 2r_{dsc2} = 0.1$ , the output current of SC2 is higher than SC1. However, as they have same gains of SC voltage control loop, the recovery speed of SC voltages of two SCs are the same as shown in Fig. 4.21(c).

## 4.2.5 Experimental Results

For experimental verification, a DC microgrid as shown in Fig. 4.11 is implemented with one DG and two SC converters. The parameters as same as in simulation are used except the SC capacity, the SC capacity of experiment is  $28F$  as it is available in laboratory. DG and SC converter are controlled by TMS320F28379D DSPs with sampling frequency at  $10kHz$ .

Fig. 4.22 shows the performance of proposed method with different gains of SC voltage control loop. As the capacity of the SC is  $28F$  in experiment, the gains of SC voltage control loop are calculated again as  $k_{Psc} = 3$ ,  $k_{Isc} = 7.5$  for  $f_{vsc} = 1Hz$  in Fig. 4.22(a) and as  $k_{Psc} = 1.5$ ,  $k_{Isc} = 3.75$  for  $f_{vsc} = 0.5Hz$  in Fig. 4.22(b). It shows that the settling and SC voltage recovery time if SC converter in Fig. 4.22(a) is faster than in Fig. 4.22(b). Moreover, the sharing current between SC converters is ensured by droop controller with same droop coefficient.

To evaluate the proposed method with different current sharing ratio, the  $r_{dsc1} = 0.2$

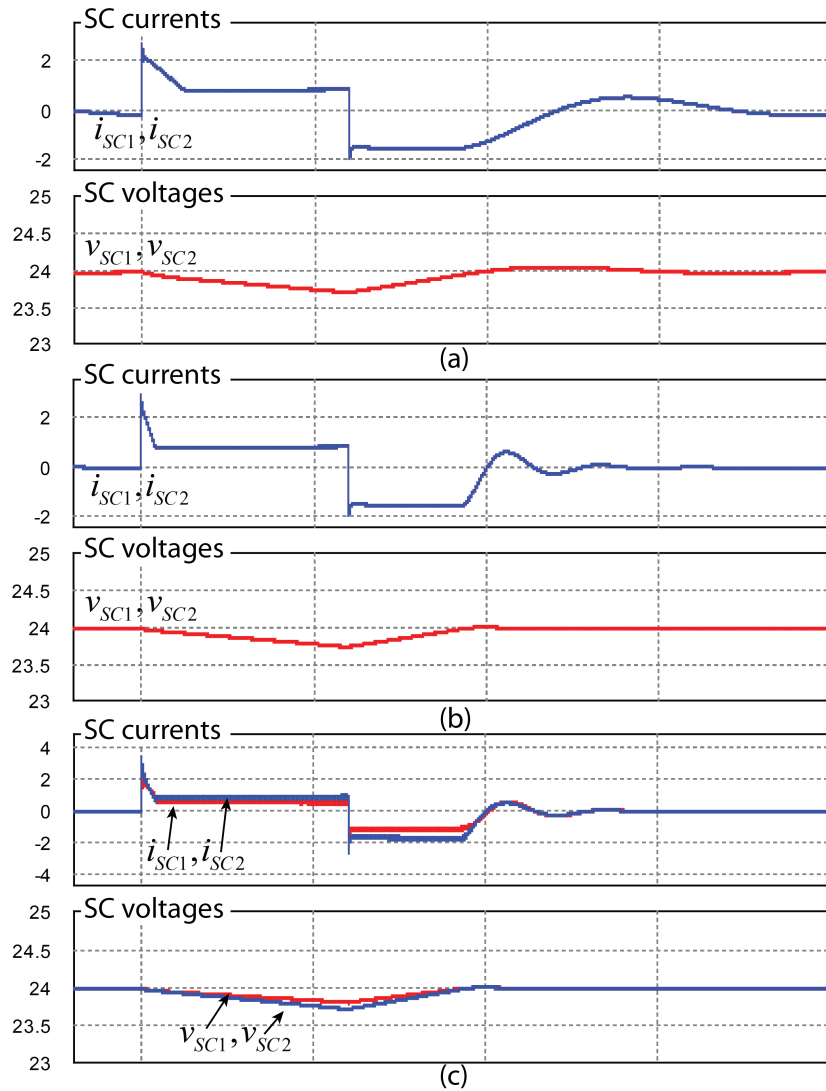


Figure 4.21: Proposed method with different SC voltage loop gains.

(a)  $r_{dsc1} = r_{dsc2} = 0.05$ ,  $k_{Psc} = -7.912$ ,  $k_{Isc} = -0.081568$

(b)  $r_{dsc1} = r_{dsc2} = 0.05$ ,  $k_{Psc} = -21.0978$ ,  $k_{Isc} = -1.1721$

(c)  $r_{dsc1} = 0.1$ ,  $r_{dsc2} = 0.05$ ,  $k_{Psc} = -21.0978$ ,  $k_{Isc} = -1.1721$

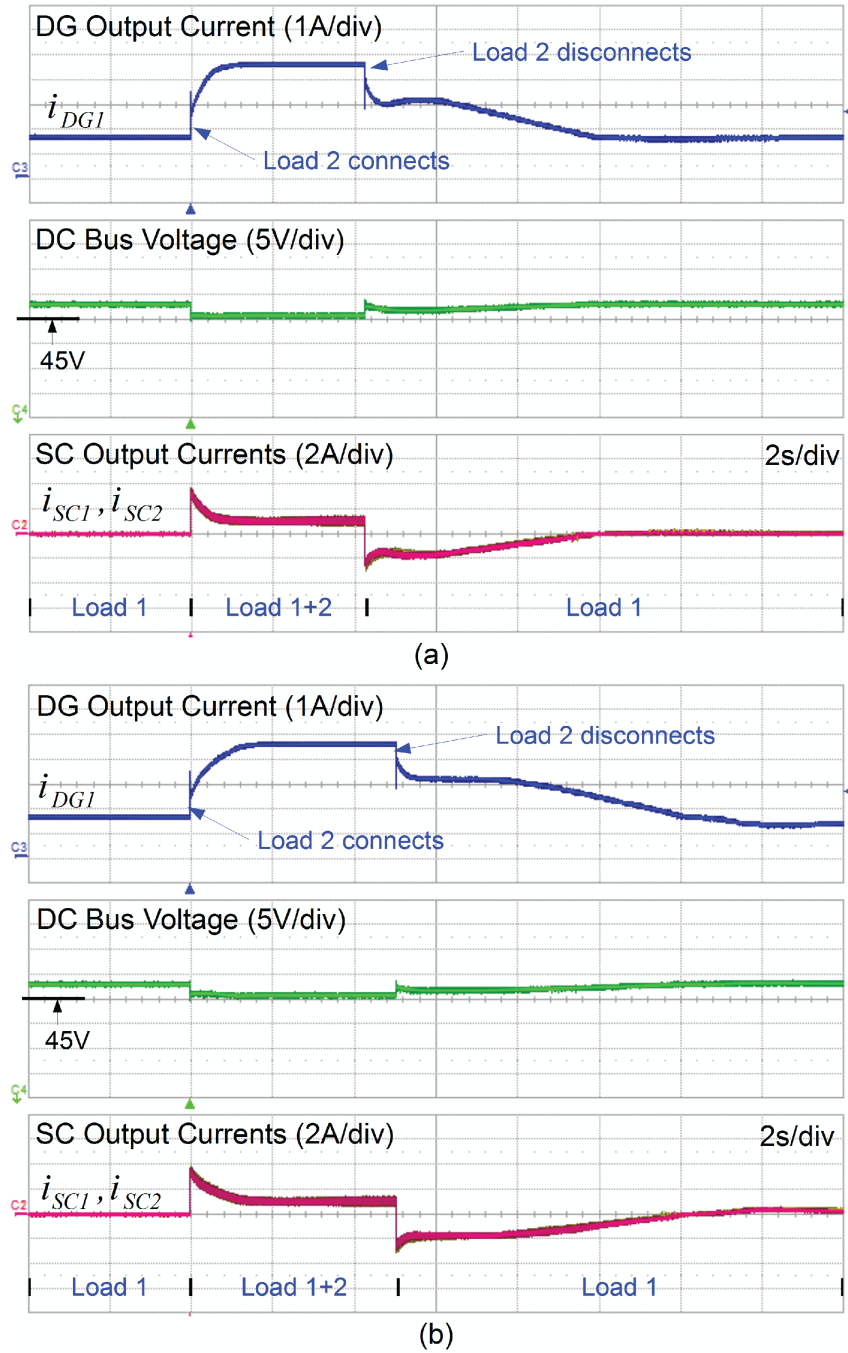


Figure 4.22: Experimental results – different SC voltage gains.

- (a)  $k_{Psc} = 3$ ,  $k_{Isc} = 7.5$  for  $f_{vsc} = 1Hz$
- (b)  $k_{Psc} = 1.5$ ,  $k_{Isc} = 3.75$  for  $f_{vsc} = 0.5Hz$

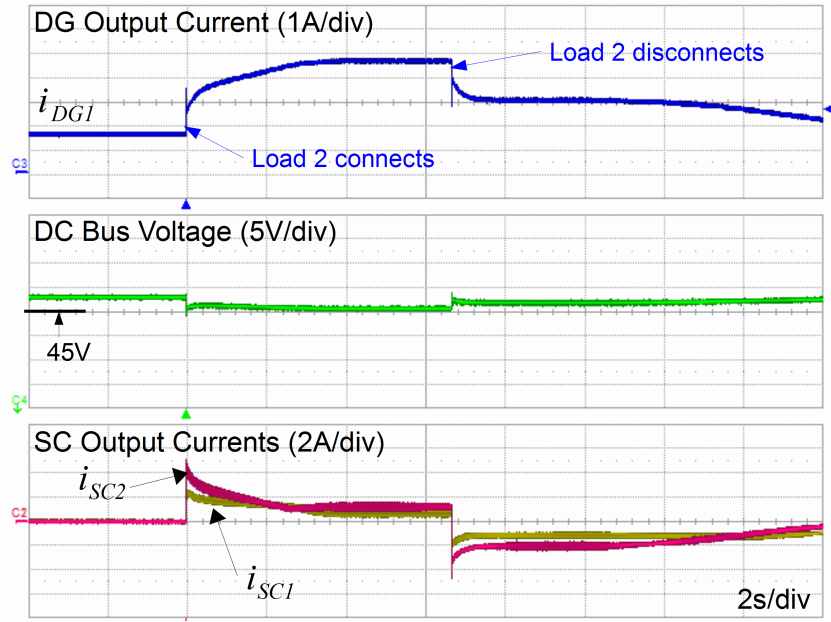


Figure 4.23: Experimental results – different SC droop coefficients.

is twice as  $r_{dsc2} = 0.1$ , the performance is shown in Fig. 4.23. It shows that the output current of SC1 is half of SC2 when the settling time is same as the gains of SC voltage control loops are identical.

The operation of the proposed method with difference of initial SC voltage values is tested and the result is shown in Fig. 4.24. In state 1, both SC1 and SC2 are charged to restore their SC voltage level. When the SC2 is fully restored, the proposed method changes to state 2; the current of SC2 reduces to zero, while SC1 increases its charging current. In state 3 when a pulsed load is connected, both SC1 and SC2 are controlled to support the DC microgrid with a same sharing ratio; at the moment that pulsed load is disconnected, both SC1 and SC2 automatically change their mode to regulate their SC voltages in state 4. When both SCs are fully charged, it changes to state 5; SC1 and SC2 reach their steady state with zero output current. So, the SC voltage of SC1 and SC2 are balanced even the initial values are different.

The experimental results show that the proposed method can effectively compensate the load current variation due to the normal load as well as the pulsed load, and also the SoC of SC is automatically regulated.

## 4.2.6 Conclusion

This section presented a droop based control method for the SC converter to compensate the transient normal load current as well as the pulsed load current together with the

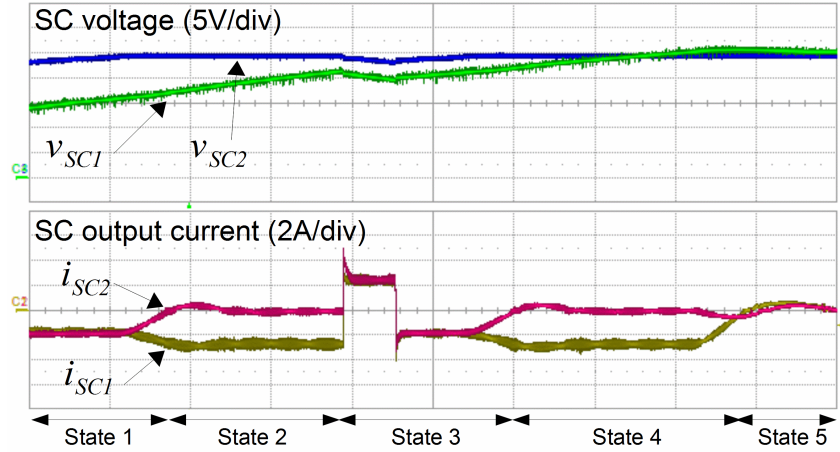


Figure 4.24: Experimental results – different SC initial voltages.

automatic SC voltage restoration. By actively adjusting the nominal voltage of the droop controller, the proposed method supplies the spike current to compensate the transient load current and support the system under the pulsed load condition. Moreover, the SoC of the SC units are automatically regulated to be balanced. By using the droop control concept, the parallel operation of multi SC units is guaranteed, and the power sharing ratio is manipulated by the droop coefficient. The performance and effectiveness of the proposed control method are verified by simulation and experimental results.

### 4.3 Summary

This chapter presented two control methods to compensate the transient current in DC microgrid by using SC. The adaptive virtual impedance control method for the SC is firstly presented. By adjusting the virtual impedance according to the SC voltage level, the proposed AVCM can compensate the transient current while regulating the SC voltage level. However, AVCM only support the sources under normal load changes but not the pulsed load, which has very high peak current in short term. To overcome this problem, the droop based control method for SC is proposed. By adjusting the droop controller parameters, the SC converter can actively compensate the transient current as well as support the source under pulsed load condition. Moreover, the SC voltage level also regulated to its nominal voltage regardless to the operation condition. The effectiveness of the proposed control methods are verified by simulation and experimental results.

## Chapter 5

# Hybrid Energy Storage System for Power Quality Improvement

In previous chapters, the power quality is improved by several control methods for DGs and Supercapacitor units. The static power quality is improved with a secondary controller. For further power quality improvement in DC Microgrid, the battery energy storage system (BESS) is used to supply the mismatch power between sources and loads. An ideal BESS has very high energy and power densities, which has not been achieved yet. Fortunately, the combination of a battery and supercapacitor could provide high energy and power densities in a hybrid energy storage system (HESS) [64].

Many HESS configurations have been studied for DC microgrids and are classified into three types, as shown in Fig. 5.1:

1. A battery and supercapacitor are connected in parallel to the DC bus through a DC-DC converter, which is the simplest configuration, as shown in Fig. 5.1(a) [27, 65]. It has advantages such as low cost and easy control, but the current sharing between the battery and supercapacitor is not controllable.
2. A battery and supercapacitor are connected to a multi-input topology converter, as shown in Fig. 5.1(b) [27, 66–68]. In this method, the line impedance between the battery and supercapacitor is neglected, which reduces the system losses. However, the control scheme of this method is hard to adapt to a DC microgrid because it needs an additional control method to cooperate with other units in the microgrid.
3. A battery and supercapacitor are connected to the DC bus through DC-DC converter, as shown in Fig. 5.1(c) [59, 69]. In this configuration, the control options are increased, but a complicated controller is needed to coordinate the operation of the supercapacitor and battery. Moreover, the line resistance between the supercapacitor and battery causes a spike in the battery current when the load changes.

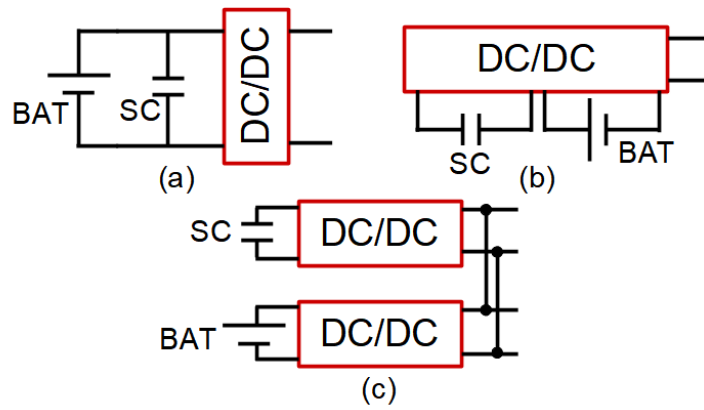


Figure 5.1: Typical HESS configurations.

To integrate a HESS into DC microgrid, a dedicated control method should be used. Recently, several coordinating methods have been adapted to integrate a battery and a supercapacitor into a system based on a high-pass filter or virtual impedance methods. Two main objectives are considered: the battery current compensation and the supercapacitor's state of charge (SoC) regulation.

This chapter presents a new configuration of a hybrid energy storage system (HESS) called a battery-inductor-supercapacitor HESS (BLSC-HESS). It splits power between a battery and supercapacitor and can operate in parallel in a DC microgrid. The power sharing is achieved between the battery and the supercapacitor by combining an internal battery resistor and output LSC filter, which consists of a supercapacitor and an inductor. The battery current is smoothed to supply and receive only the low-frequency current component under any disturbances and load conditions through cooperation with the supercapacitor. Complete guidelines to design the parameters of the BLSC-HESS are also presented. Simulation and experimental results prove that the proposed BLSC-HESS configuration achieves high stability performance and lower cost, and it is easily applied to a DC microgrid.

## 5.1 System Description

A typical DC microgrid including a HESS is shown in Fig. 5.2. The sources and loads are connected to a common DC bus. The HESS units are used to compensate the current mismatch between the RES and the load to operate the microgrid system effectively.



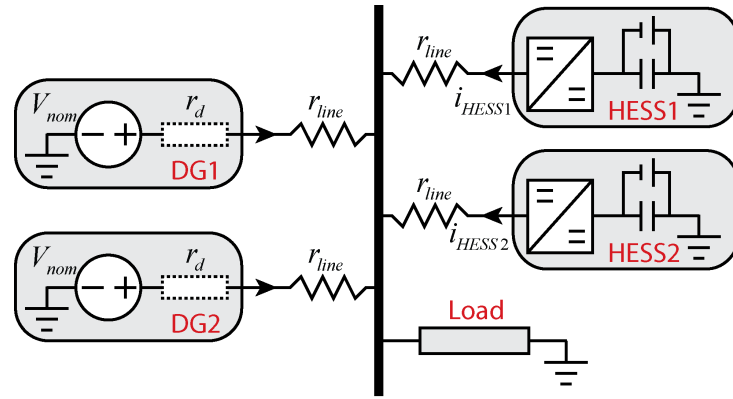


Figure 5.2: Typical configuration of DC microgrid with HESS.

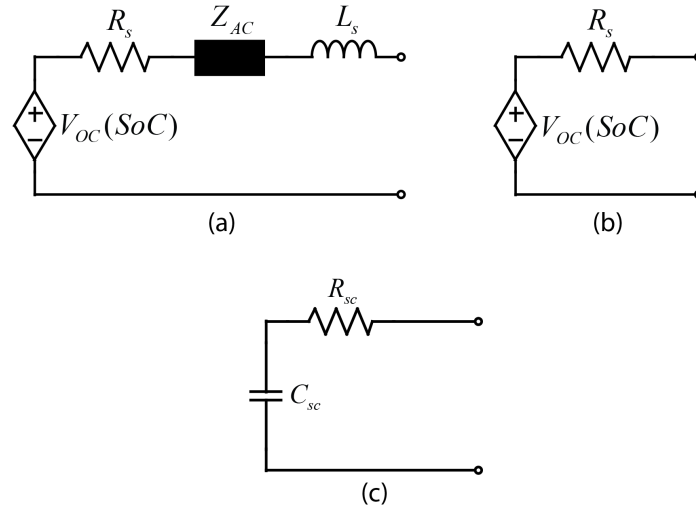


Figure 5.3: Battery and SC models (a) impedance-based model (b) simple model and (c) SC model.

### 5.1.1 Cooperation in a DC Microgrid

To integrate various sources in a DC microgrid, a cooperating controller such as master-slave or droop controller is normally required. In general, droop control is more popular for DC microgrids because of its advantage of decentralization without a communication interface. The current sharing in droop control is based on the virtual resistance or the droop coefficient, and the higher droop coefficient is, the lower the shared current is. In a DC microgrid, at least one RES unit is operated with the droop control to regulate the DC bus voltage. In this study, the DC microgrid is controlled by droop control to share power between the sources.

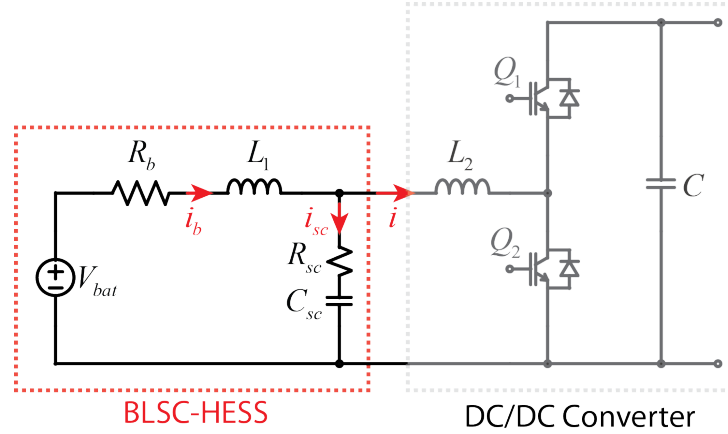


Figure 5.4: Proposed HESS Configuration.

### 5.1.2 Battery and Supercapacitor Models

Fig. 5.3 shows the battery and supercapacitor models, which are used as equivalent models to evaluate the performance of the HESS. There are many models of battery such as simple battery model [70, 71], Thevenin based electrical model [72], Impedance-based model [73], and Dual Polarization (DP) model [74]. Fig. 5.3(a) is the impedance-based model, which is widely used in battery design, SoC estimation or real-time battery simulation [75]. In this chapter, because the battery is used only for charging or discharging in HESS application, the model in Fig. 5.3(b) is used to analyze the battery which operates at low frequency [76]. In Fig. 5.3(b), the battery is regarded as a voltage source  $V_{bat}$  with a series resistor  $R_b$  at a specific SoC::

$$\begin{cases} V_{bat} = V_{OC}(SoC) \\ R_b = R_s \end{cases} \quad (5.1)$$

where  $V_{OC}(SoC)$  is the open circuit voltage of the battery at specific SoC, and  $R_s$  is internal equivalent resistance.

The supercapacitor has much higher power density and lower internal resistance and can be modeled as shown in Fig. 5.3(b) [65]. The values of  $C_{sc}$  and  $R_{sc}$  are provided in the datasheet by the manufacturer.

## 5.2 Proposed BLSC-HESS Configuration

The proposed BLSC-HESS configuration is shown in Fig. 5.4. The BLSC-HESS is constructed by inserting an inductor between the battery and the supercapacitor, which are connected to a common DC bus through a DC-DC converter. As shown in Fig. 5.4, the construction of the inductor and supercapacitor is regarded as a low pass filter for the

battery. The output current of the BLSC-HESS is decoupled into two parts: the battery current and the supercapacitor current based on the frequency domain. The low-frequency current is handled by the battery, while the high-frequency current is handled by the supercapacitor. The BLSC-HESS parameters were investigated to analyse the performance of this low pass filter.

### 5.2.1 BLSC-HESS Parameters

To design the parameters of the BLSC-HESS properly, there are two main points to consider: the current coupling frequency between the battery and the supercapacitor, and the voltage level of the supercapacitor. The currents on the BLSC-HESS can be analyzed by using the transfer function  $G_{i_{BLSC}}(s)$  of the ratio between the battery current and the supercapacitor current. The supercapacitor voltage level can be calculated by using the transfer function  $G_{v_{BLSC}}(s)$  of the supercapacitor voltage level over the battery voltage level. The battery  $V_{bat}$  is assumed to be constant in this analysis as it changes very slow.

From Fig. 5.4, we can obtain the battery current  $i_b$  and the supercapacitor current  $i_{sc}$  as:

$$\begin{cases} i_b = (V_{bat} - v_{sc}) / (R_b + Z_{L_1}) \\ i_{sc} = v_{sc} / (R_{sc} + Z_{C_{sc}}) \end{cases}, \quad (5.2)$$

where  $Z_{L_1}$  and  $Z_{C_{sc}}$  are the impedance of  $L_1$  and  $C_{sc}$ , respectively. In the frequency domain of small signal modeling, equation (5.2) is rewritten as in (5.3) as small signal disturbance of  $V_{bat}$  is zero:

$$\begin{cases} i_b = v_{sc}(s) / (R_b + L_1 s) \\ i_{sc} = v_{sc}(s) / (R_{sc} + 1 / (C_{sc} s)) \end{cases}. \quad (5.3)$$

The total current of the HESS is the sum of the battery current and the supercapacitor current:

$$i = i_b - i_{sc}. \quad (5.4)$$

Then,  $G_{i_{BLSC}}(s)$ , can be obtained as

$$G_{i_{BLSC}}(s) = \frac{i_b}{i} = \frac{1 + R_{sc} C_{sc} s}{1 + (R_{sc} + R_b) C_{sc} s + L_1 C_{sc} s^2}. \quad (5.5)$$

From (5.5),  $G_{i_{BLSC}}(s)$  has one zero and two poles when  $L_1$  is greater than zero

$$\begin{cases} z_1 = -\frac{1}{R_{sc}C_{sc}} \\ p_1 = -\frac{(R_{sc} + R_b)C_{sc} - \sqrt{(R_{sc} + R_b)^2C_{sc}^2 - 4L_1C_{sc}}}{2L_1C_{sc}} \\ p_2 = -\frac{(R_{sc} + R_b)C_{sc} + \sqrt{(R_{sc} + R_b)^2C_{sc}^2 - 4L_1C_{sc}}}{2L_1C_{sc}} \end{cases} \quad (5.6)$$

In the case of a conventional battery and supercapacitor connection,  $L_1$  is zero and  $G_{i_{BLSC}}(s)$  becomes:

$$G_{i_{BSC}}(s) = G_{i_{BLSC}}(s)|_{L_1=0} = \frac{i_b}{i} = \frac{1 + R_{sc}C_{sc}s}{1 + (R_{sc} + R_b)C_{sc}s} \quad (5.7)$$

From (5.7),  $G_{i_{BSC}}(s)$  has one zero and one pole:

$$\begin{cases} z_1 = -\frac{1}{R_{sc}C_{sc}} \\ p_1 = -\frac{1}{(R_{sc} + R_b)C_{sc}} \end{cases} \quad (5.8)$$

As one pole is missing, the conventional configuration has a weak point in that the gain of  $G_{i_{BSC}}(s)$  at high frequency is high due to its zero. To analyse the effects of the BLSC-HESS parameters, each parameter was swept, and the Bode diagram of the BLSC-HESS was shown to examine the performance.

### 5.2.2 Supercapacitor $C_{sc}$

Fig. 5 shows the Bode diagram of  $G_{i_{BLSC}}(s)$  and  $G_{i_{BSC}}(s)$  when the value of  $C_{sc}$  changes from 10 to 30F. The remaining parameters are  $L_1 = 0.5mH$ ,  $R_{sc} = 15m\Omega$ , and  $R_b = 0.1\Omega$ . As shown in Fig. 5.5, the cut-off frequency of  $G_{i_{BLSC}}(s)$  decreases when  $C_{sc}$  increases. Theoretically, the decoupling frequency of  $G_{i_{BLSC}}(s)$  is determined by the first pole  $p_1$  in (5.6) as follows:

$$f_c = -\frac{p_1}{2\pi} = \frac{(R_{sc} + R_b)C_{sc} - \sqrt{(R_{sc} + R_b)^2C_{sc}^2 - 4L_1C_{sc}}}{4\pi L_1C_{sc}}. \quad (5.9)$$

$L_1$  is very small compared with  $C_{sc}$ , so the value of the first pole  $p_1$  is almost the same as  $p_{10}$  in (5.8) because the cut-off frequencies of  $G_{i_{BLSC}}(s)$  and  $G_{i_{BSC}}(s)$  are the same, as

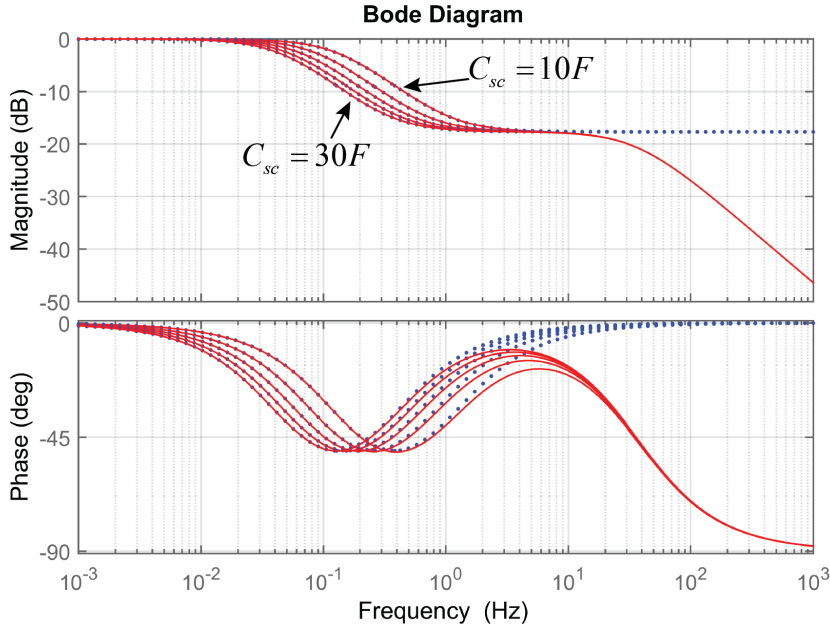


Figure 5.5: Bode diagram of  $G_{i_{BLS_C}}(s)$  (solid lines) and  $G_{i_{BSC}}(s)$  (dotted line) according to  $C_{sc}$  with  $L_1 = 0.5 \text{ mH}$ ,  $R_{SC} = 15 \text{ m}\Omega$ , and  $R_b = 0.1 \Omega$ .

shown in Fig. 5.5. Finally, the decoupling frequency  $f_c$  can be rewritten as:

$$f_c \approx -\frac{p_{10}}{2\pi} = \frac{1}{2\pi(R_{sc} + R_b)C_{sc}}. \quad (5.10)$$

The capacitance of supercapacitor does not affect the gain of  $G_{i_{BLS_C}}(s)$  at high frequency, as shown in Fig. 5.5. Therefore, increasing the capacitance of the supercapacitor will not help to reduce the high-frequency current component on the battery side.

### 5.2.3 The Battery's Internal Resistance $R_b$

The battery's internal resistance is predefined, and its effect was analyzed to examine the performance of the BLSC-HESS in different systems. The Bode diagrams of  $G_{i_{BLS_C}}(s)$  and  $G_{i_{BSC}}(s)$  are shown in Fig. 5.6 with  $R_b$  changing from 0.1 to 0.5  $\Omega$ . The remaining parameters are  $L_1 = 0.5 \text{ mH}$ ,  $R_{SC} = 15 \text{ m}\Omega$ , and  $C_{sc} = 28 \text{ F}$ .

With the conventional configuration, a battery with high internal resistance can reduce the effect of the high-frequency current component on the battery side because the gain of  $G_{i_{BSC}}(s)$  is very small, as shown in Fig. 5.6. However, when increasing the battery capacity by increasing the number of parallel battery cells, the internal resistance becomes smaller. Therefore, the gain of  $G_{i_{BSC}}(s)$  becomes higher, which means that the high-frequency current can flow to the battery side.

As the value of  $R_b$  is much larger than  $R_{sc}$ , its effect on the performance of BLSC-HESS

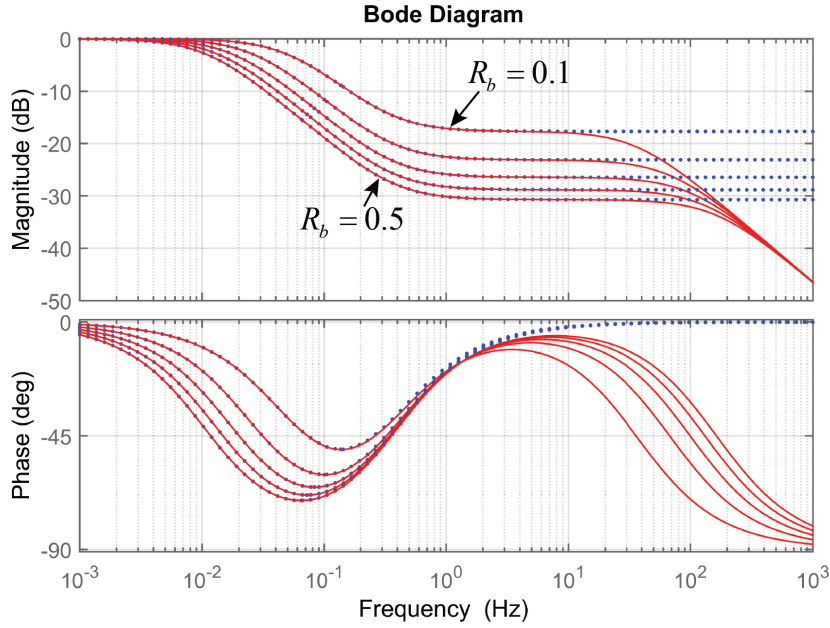


Figure 5.6: Bode diagram of  $G_{iBLSC}(s)$  (solid lines) and  $G_{iBSC}(s)$  (dotted line) according to  $R_b$  while  $L_1 = 0.5 \text{ mH}$ ,  $R_{SC} = 15 \text{ m}\Omega$ , and  $C_{sc} = 28 \text{ F}$ .

is dominant compare with  $R_{sc}$ . The internal resistor of battery  $R_b$  acts as a damping resistor the LSC circuit, and stabilizes the source.

#### 5.2.4 Inductance $L_1$

To evaluate the effect of the inserted inductor, the Bode diagrams of  $G_{iBLSC}(s)$  and  $G_{iBSC}(s)$  are shown in Fig. 5.7 for when  $L_1$  changes from 0.5 to 2.5  $\text{mH}$ . The remaining parameters are  $R_b = 0.1 \Omega$ ,  $R_{SC} = 15 \text{ m}\Omega$  and  $C_{sc} = 28 \text{ F}$ . The gain of  $G_{iBSC}(s)$  becomes constant at high frequency and is higher than  $-20 \text{ dB}$  when the internal battery resistance is small ( $R_b = 0.1$ ). As a result, currents with high frequency such as ripple current, harmonic current, or switching current can flow from the supercapacitor to the battery, which greatly reduces the battery lifetime. On the other hand, the performance of the BLSC-HESS is the same as that of the conventional configuration in the low-frequency range. However, in a general DC microgrid, harmonic current can appear due to the various types of loads. With a load such as variable motor driver, the harmonic is double the fundamental frequency (100  $\text{Hz}$  or 120  $\text{Hz}$ ). As shown in Fig. 5.7, the gain of  $G_{iBSC}(s)$  is constant and higher than  $-20 \text{ dB}$  when the frequency is greater than 1  $\text{Hz}$ . However, the gain of  $G_{iBLSC}(s)$  becomes significantly smaller compared with  $G_{iBSC}(s)$  because of the inserted inductor  $L_1$ . Therefore, to effectively reduce the high-frequency current component on the battery side, the value of  $L_1$  is calculated so that the gain of

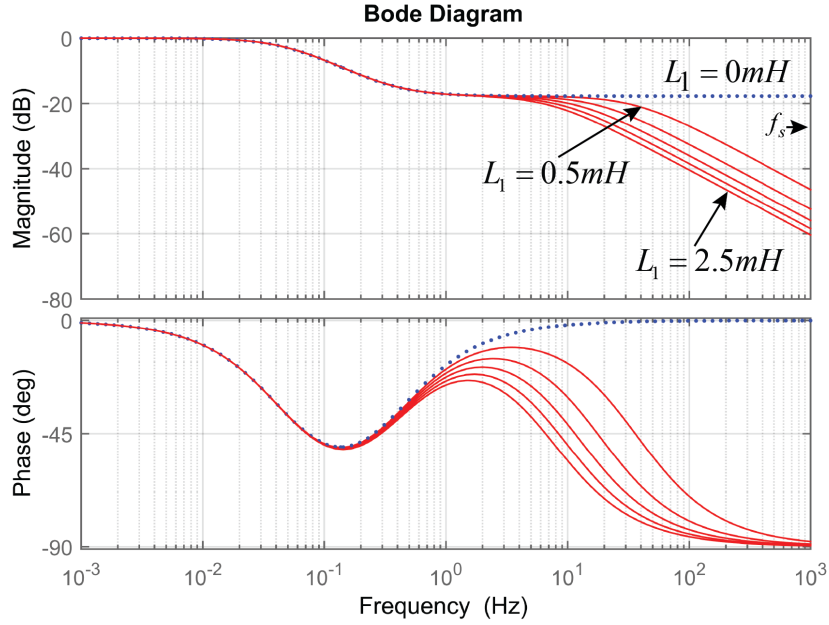


Figure 5.7: Bode diagram of  $G_{i_{BLSC}}(s)$  (solid lines) and  $G_{i_{BSC}}(s)$  (dotted line) according to  $L_1$  with  $R_b = 0.1 \Omega$ ,  $R_{SC} = 15 \text{ m}\Omega$ , and  $C_{sc} = 28 \text{ F}$

$G_{i_{BLSC}}(s)$  at 100 Hz is less than  $-20 \text{ dB}$ .

$$G_{i_{BLSC}}(s)|_{f=100\text{Hz}} < -20 \text{ dB} \quad (5.11)$$

### 5.2.5 SC Voltage

To analyze the supercapacitor voltage variation, the transfer function of the supercapacitor voltage over the battery voltage is obtained from Fig. 5.4:

$$G_{v_{sc}}(s) = \frac{v_{sc}}{V_{bat}} = \frac{R_c + \frac{1}{C_{sc}s}}{R_c + \frac{1}{C_{sc}s} + L_1s}. \quad (5.12)$$

From (5.12),  $G_{v_{sc}}(s)$  becomes unity as  $L_1s$  becomes very small because it is hard for battery voltage to change quickly. As a result, the output voltage of the supercapacitor is equal to the battery output voltage in steady state. By choosing the rated voltage of the supercapacitor to be higher than the operation voltage of the battery, the task of controlling the supercapacitor voltage can be neglected in the BLSC-HESS.

### 5.2.6 Settling Time

The settling time of BLSC-HESS is defined as the time required for the response of the BLSC-HESS to reach and stay within a range of 10 of its final output current in this

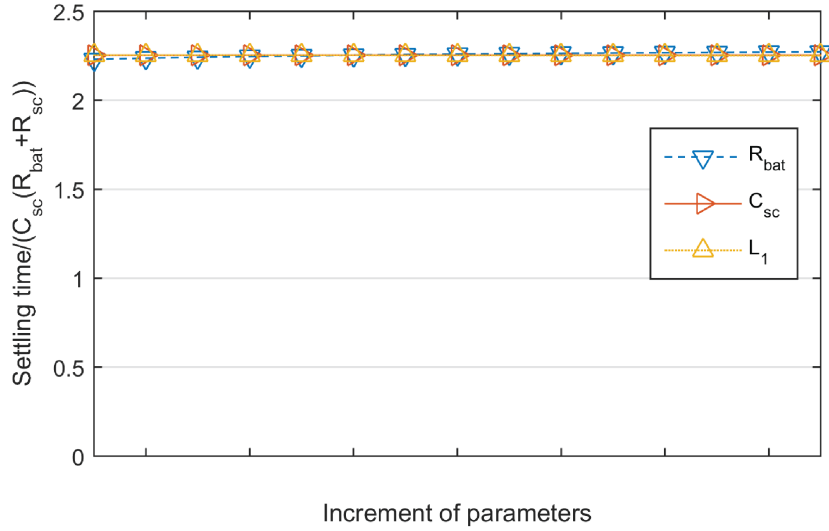


Figure 5.8: Ratio between settling time and  $C_{sc}(R_{bat} + R_{sc})$ .

study. To evaluate the settling time, a unit step of  $R(s) = 1/s$  was used as the input of the  $G_{i_{BLSC}}(s)$ , and the output becomes the following:

$$F(s) = R(s)G_{LCS}(s) = \frac{1}{s} \times \frac{1 + R_{sc}C_{sc}s}{1 + (R_{sc} + R_b)C_{sc}s + L_1C_{sc}s^2}. \quad (5.13)$$

Using the MATLAB symbolic toolbox, the output signal is expressed in the time domain as follows:

$$F(t) = 1 - \exp\left(-\frac{t(R_b + R_{sc})}{2L_1}\right). \quad (5.14)$$

Because of the complicated  $F_{sub}(t)$ , a statistical method was used to estimate the settling time. The decoupling frequency is decided by the first pole  $p_1$ , so the settling time  $t_s$  was calculated by MATLAB and compared with the value of the first pole to find out the relationship between them. The parameters of the BLSC-HESS were swept to evaluate the ratio  $t_s / ((R_{sc} + R_b)C_{sc})$ . The parameter ranges are from 0.1 to 0.54  $\Omega$  for  $R_b$ , from 10 to 40  $F$  for  $C_{sc}$ , and from 0.1 to 1.5  $mH$  for  $L_1$ . The calculated ratio of  $t_s / ((R_{sc} + R_b)C_{sc})$  is plotted in Fig. 5.8, where the ratio is approximately constant at 2.25. Therefore, the settling time can be estimated as:

$$t_s \approx 2.25C_{sc}(R_b + R_{sc}). \quad (5.15)$$

Finally, design guidelines for the BLSC-HESS are briefly summarized:

Step 1: Select the settling time  $t_s$  in (5.15) or in (5.16), which is calculated based on



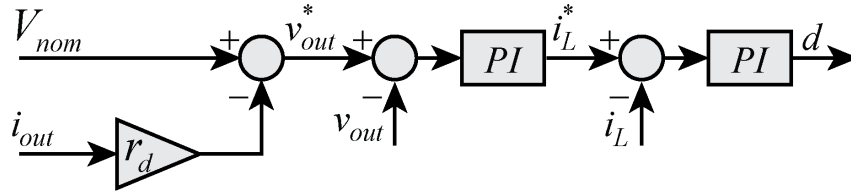


Figure 5.9: Control diagram of BLSC-HESS.

the decoupling frequency  $f_c$  of the BLSC-HESS.

$$t_s = \frac{2.25}{2\pi} \frac{1}{f_c} \quad (5.16)$$

Step 2: Calculate the capacitance of the supercapacitor:

$$C_{sc} = \frac{t_s}{2.25 (R_{sc} + R_b)}. \quad (5.17)$$

Step 3: Calculate the value of the inductor, which helps to reduce the ripple current on the battery side by reducing the gain of  $G_{i_{BLSC}}(s)$  at high frequency. As described in (5.11), the value of the inductor is chosen so that the gain of  $G_{i_{BLSC}}(s)$  at 100 Hz is smaller than  $-20$  dB.

### 5.2.7 HESS Control Scheme

The BLSC-HESS is controlled easily without any concern about the SoC of the supercapacitor or its voltage restoration. Fig. 5.9 shows the HESS control diagram. From Fig. 5.9, the droop controller is described as:

$$v_{out}^* = V_{nom} - r_d i_{out}, \quad (5.18)$$

where  $V_{nom}$  is the nominal DC bus voltage,  $v_{out}^*$  and  $i_{out}$  are reference output voltage and output current of the HESS, respectively, and  $r_d$  is the droop coefficient or virtual impedance.

The droop coefficient is calculated based on the HESS's rated current as:

$$r_d = \frac{V_{nom} - V_{min}}{i_{rated}}, \quad (5.19)$$

where  $V_{min}$  is the minimum allowable voltage of the DC bus, and  $i_{rated}$  is the rated current of the HESS converter. The HESS's output voltage is regulated by the inductor current, and the inductor current reference  $i_L^*$  is obtained from the PI controller of the voltage

Table 5.1: Comparison between HESS Configurations

Configuration	Volume	Cost	High frequency compensation performance	Efficiency
5.1(a)	+ +	+ +	-	+ +
5.1(b)	-	-	+ + +	+
5.1(c)	- -	- -	+ + +	+
Proposed	+	+	+ +	+ +

Note: - Negative point + Positive point

control loop

$$i_L^* = \left( k_{Pv} + \frac{k_{Iv}}{s} \right) (v_{out}^* - v_{out}), \quad (5.20)$$

where  $k_{Pv}$  and  $k_{Iv}$  are the PI gains of the voltage control loop. Another PI controller is then used to control the inductor current:

$$d = \left( k_{Pi} + \frac{k_{Ii}}{s} \right) (i_L^* - i_L), \quad (5.21)$$

where  $k_{Pi}$  and  $k_{Ii}$  are the PI gains of the current control loop. The cut-off frequency of the current loop is selected to be 1/10 of the switching frequency of the HESS converter, and that of the voltage control loop is chosen as 1/10 of the current loop's cut-off frequency.

### 5.2.8 HESS Size and Efficiency Discussion

The proposed configuration uses only one additional inductor instead of DC-DC converter. Even though its volume becomes slightly larger compared with the configuration in Fig. 5.1(a), it is much smaller than the configuration in Fig. 5.1(b) or Fig. 5.1(c); the inductor volume is much smaller with cheaper price compared with DC-DC converter because small inductance is enough to decouple the high frequency current between battery and SC. Because the cut-off decoupling frequency is depended on the hardware parameters, it needs to be changed when the battery or inductor is replaced. Some HESS topologies are compared in Table 5.1. From Table 5.1, we can say that the proposed configuration has superior performance from price and volume.

## 5.3 Simulation Results

The DC microgrid shown in Fig. 5.2 was modeled using PSIM simulation software to evaluate the proposed BLSC-HESS with the parameters in table 5.2. The nominal DC bus voltage in the microgrid is 48 V with a load of 20 Ω, and two distributed generation

Table 5.2: Parameters used in simulation and experiment.

Parameter	Symbol	Value
<b>DC Microgrid</b>		
DC Bus voltage	$V_{nom} - V_{min}$	45 – 48 V
Droop coefficient of HESS	$r_d$	0.3
DGs output current		0 – 8 A
Load		20 $\Omega$
<b>BLSC-HESS Converter</b>		
Inductor	$L_2$	0.5 mH
Output Capacitor	$C$	2200 $\mu F$
Switching frequency	$f_s$	20 kHz
Battery open circuit voltage	$V_{OC}$	24 V
SC nominal voltage		24 V

sources are controlled as a current source to imitate renewable energy sources. The BLSC-HESS is connected to the DC bus through a bidirectional converter, as shown in Fig. 5.4.

To evaluate the effectiveness of the BLSC-HESS, three case studies were investigated. Case I shows the normal operation, case II shows the effect of the BLSC-HESS parameters on the settling time, and case III evaluates the cooperation of two BLSC-HESSs.

Case I: Only one BLSC-HESS is activated, and the parameters of BLSC-HESS are  $L_1 = 0.47$  mH,  $C_{sc} = 4$  F,  $R_{sc} = 25$  m $\Omega$ , and  $R_b = 0.1$   $\Omega$ . In Fig. 5.10, when the distributed generation current suddenly increases from 0 to 5A, the BLSC-HESS changes from charge to discharge mode to balance the system power flow according to the change of the injected current from the distributed generation. As shown in Fig. 5.10(a), even though the HESS changes from charge to discharge mode, the battery output current  $i_{BAT1}$  changes smoothly thanks to the pulse current  $i_{SC1}$  supplied by SC1.

Fig. 5.10(b) shows the output current  $i_{HESS1}$  of the HESS1 converter to regulate the output voltage, which is calculated by the droop equation in (18). Therefore, the DC bus voltage  $v_{bus}$  is regulated very well, as shown in Fig. 5.10(c). Moreover, the battery and supercapacitor voltages are always the same, as shown in Fig. 5.10(d), which confirms the relationship in (5.12) with normal battery voltage variation. Fig. 5.10 shows that the BLSC-HESS effectively decouples the current for the battery and supercapacitor under load variation.

Case II: Fig. 5.11 shows the output currents  $i_{BAT1}$  and  $i_{SC1}$  of the battery and supercapacitor when changing the parameters. For the same parameters used in the case I, the output current is shown in Fig. 5.11(a) for performance comparison, and the settling time is 1 s which is calculated from (5.15). When the supercapacitor capacitance is doubled to 8 F, the settling time becomes 2 s. Fig. 5.11(b) shows that the battery current response

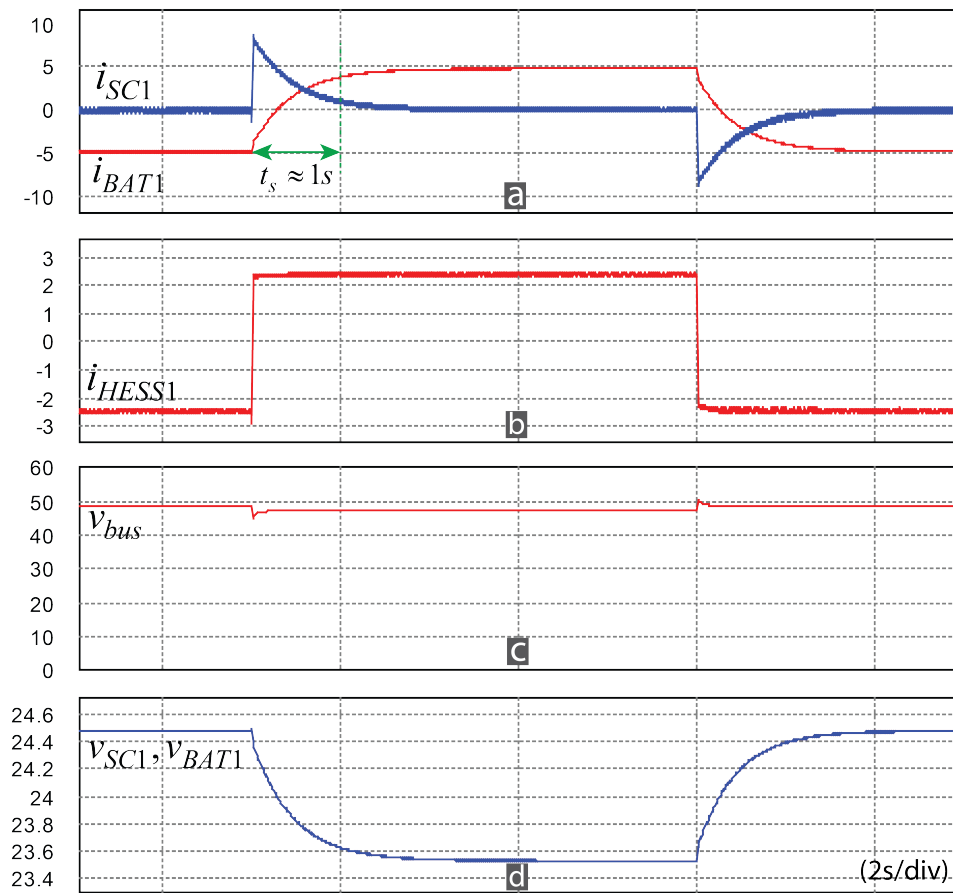


Figure 5.10: Case I: Performance simulation result of a single HESS.

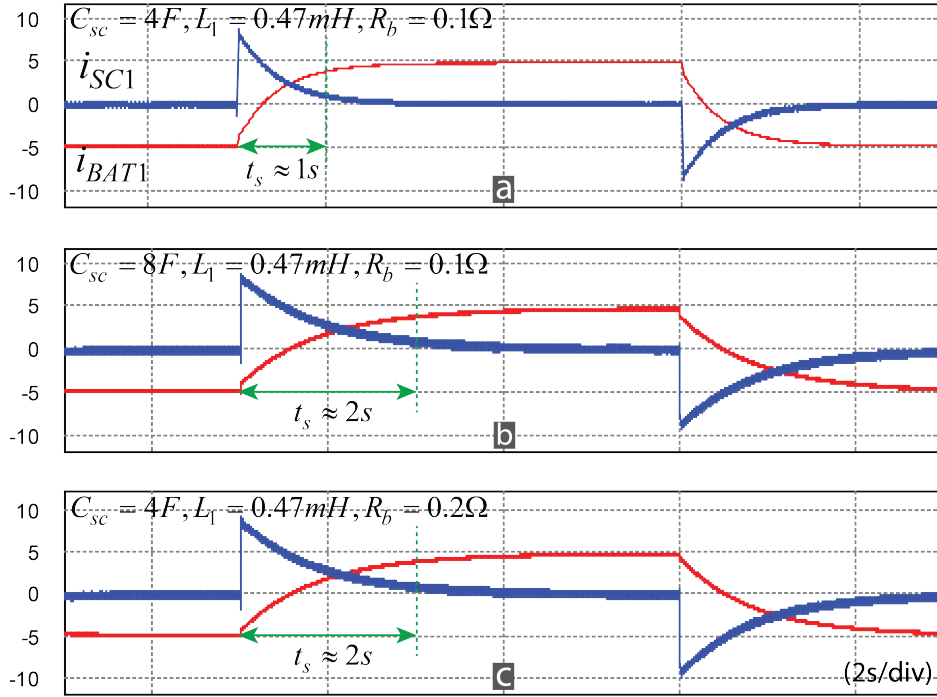


Figure 5.11: Case II: Impacts of SC capacity  $C_{sc}$  and battery internal resistance  $R_b$  on simulation results.

becomes slower due to the decreased decoupling frequency  $f_c$  of  $G_{i_{BLSC}}(s)$  with the increased capacitance. In Fig. 5.11(c), the internal resistance of the battery is increased to  $R_b = 0.2 \Omega$ , while  $C_{sc}$  is kept at  $4 F$ . The settling time of the BLSC-HESS is same ( $2 s$ ) as in Fig. 5.11(b). Case II proves the theoretical analysis to find the settling time in (5.15).

To investigate the effect of the inductance in the BLSC-HESS, the inductance  $L_1$  was changed from  $0 mH$  in Fig. 5.12(a) to  $0.12 mH$  in Fig. 5.12(b) and  $0.47 mH$  in Fig. 5.12(c). The other parameters were kept the same ( $C_{sc} = 4 F$ ,  $R_b = 0.1 \Omega$ ). To simulate the high-frequency fluctuation in the system, a high-frequency current  $i_{DG1}$  of  $100 Hz$  was injected into the DC bus, which caused the ripple in the output current  $i_{HESS1}$  of the HESS1 converter. With the conventional configuration ( $L_1 = 0 mH$ ), the gain of  $G_{i_{BSC}}(s)$  at  $100 Hz$  is higher than  $-20 dB$ , as shown in Fig. 5.7. The battery current  $i_{BAT1}$  has high fluctuation, as shown in Fig. 5.12a. When  $L_1 = 0.12 mH$ , the gain of  $G_{i_{BLSC}}(s)$  at  $100 Hz$  is reduced, which results in lower current fluctuation in Fig. 5.12b. With a much higher inductance of  $L_1 = 0.47 mH$  in Fig. 5.12c, the battery current fluctuation is reduced as the gain of  $G_{i_{BLSC}}(s)$  is around  $-28 dB$ .

Case III: To evaluate the proposed BLSC-HESS configuration in parallel operation, two BLSC-HESSs and two distributed generators were used. Two distributed generators inject

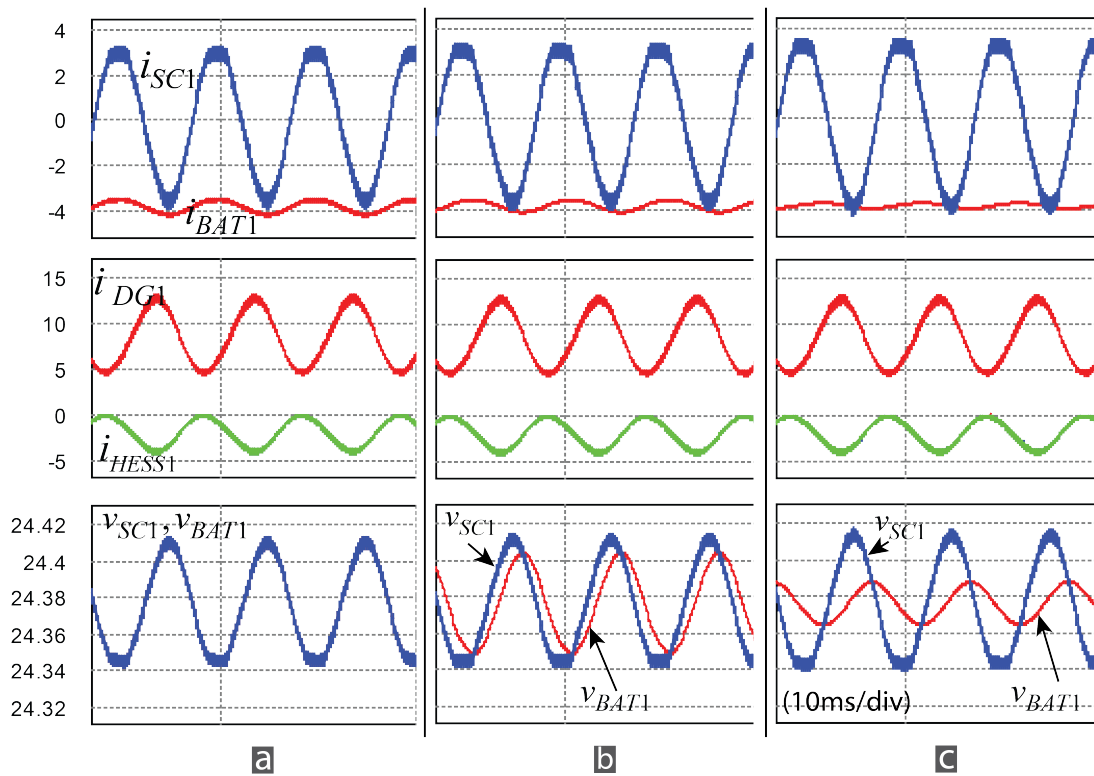


Figure 5.12: Case II: Impact of the inductance  $L_1$  on simulation results. (a) Without  $L_1$ , (b)  $L_1 = 0.12 \text{ mH}$ , (c)  $L_1 = 0.47 \text{ mH}$ .

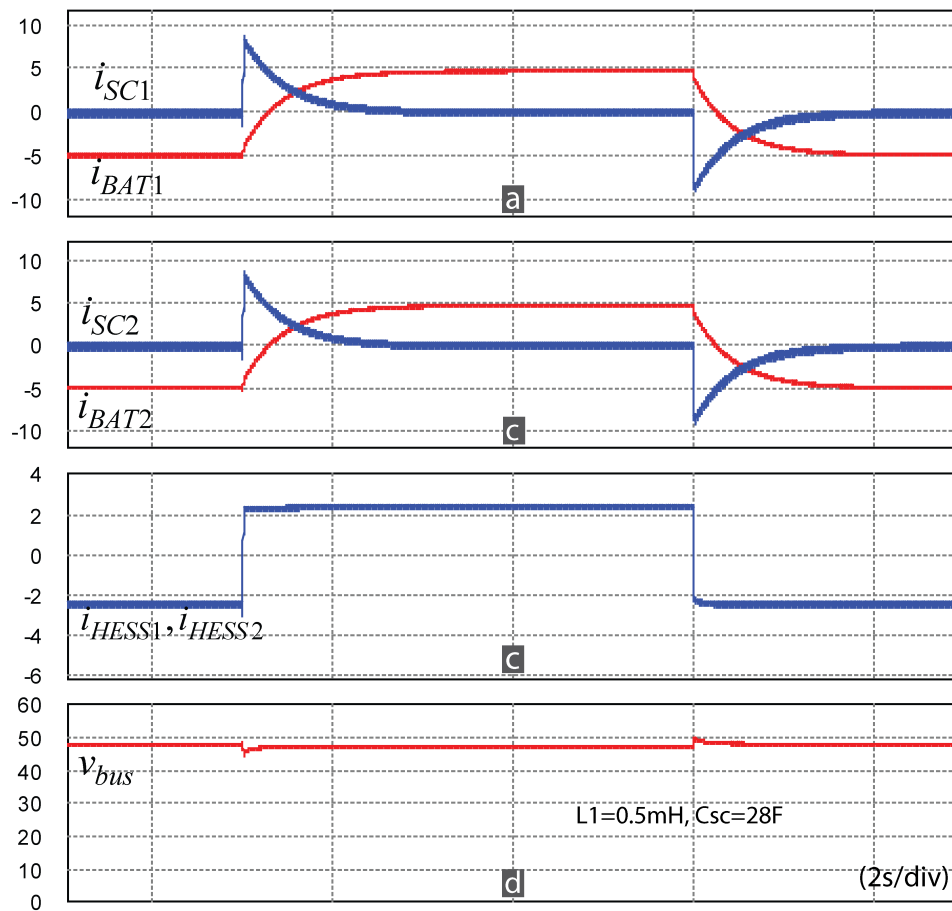


Figure 5.13: Case III: Simulation result of cooperation of two HESSs in the system.

a total current of 10 A into the DC bus, which is connected to a load of 10  $\Omega$ . The power sharing between HESSs is ensured by the droop controller. Good power sharing is achieved with the same battery output currents  $i_{BAT1}$  and  $i_{BAT2}$ , as shown in Fig. 5.13. Moreover, the current sharing between the battery and supercapacitor in two HESSs shows good performance with the same settling time  $t_s$ . As a result, the proposed HESS configuration effectively operates in parallel when using the conventional droop control. The simulation results show that the proposed BLSC-HESS configuration is applicable with advantages of lower cost and a simple control scheme. It can operate with the conventional droop control method or any advanced coordinating methods in a DC microgrid.

## 5.4 Experimental Results

To validate the proposed BLSC-HESS configuration, the DC microgrid in Fig. 5.2 with two HESSs and one distributed generator was implemented in the laboratory. The two BLSC-HESS converters in Fig. 5.4 were controlled by a TMS320F28379D DSP controller board, and another DSP control board was used for the distributed generator's converters. The parameters of the DC microgrid are the same as those used in the simulation. The distributed generation converter is controlled to inject a current of 4.5 A into a DC bus that is connected to a load of 8  $\Omega$ . The internal resistance of the battery is 0.3  $\Omega$ , and it can be changed by adding a serial resistor to the battery. Three case studies were carried out to evaluate the characteristics of the proposed HESS configuration.

Case I: Only one BLSC-HESS is activated, and the parameters of the BLSC-HESS are  $L_1 = 0.47$  mH and  $C_{sc} = 28$  F. When the load is connected to the DC bus, the HESS changes mode from charge to discharge mode. As shown in Fig. 5.14(a), the battery current  $i_{BAT1}$  smoothly changes from charge to discharge mode thanks to the pulsed supercapacitor current  $i_{SC1}$ . Figs. 5.14(b) and (c) show the waveforms of the HESS converter output current  $i_{HESS1}$  and DC bus voltage  $v_{bus}$ , which are regulated by the droop controller. In Fig. 5.14(d), the supercapacitor voltage is equal to the battery voltage in charge and discharge mode, so it is always kept in a safe operation range.

Case II: With the same setup conditions as case I, only the parameters of the BLSC-HESS are changed to evaluate its performance. The internal battery resistance normally changes when the battery parameters change, but in our experiment, it is changed by adding an external serial resistor. Fig. 5.15 shows the impacts of the supercapacitor  $C_{sc}$  and battery internal resistance  $R_b$ . Fig. 5.15(a) shows the supercapacitor and battery currents of case I, for which the settling time is 20 s. When the internal battery resistance is changed by adding an external resistance of 0.1  $\Omega$ , the settling time becomes longer in



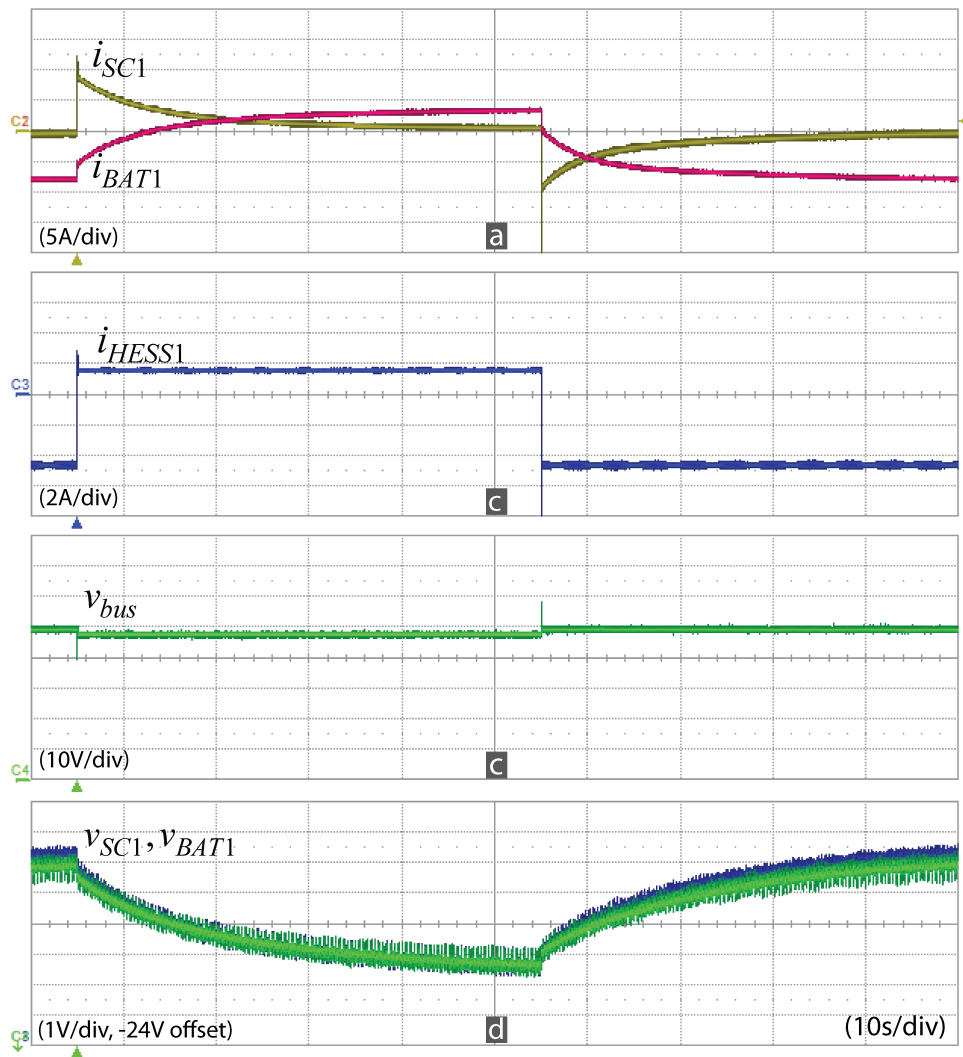


Figure 5.14: Case I: Experimental results with single HESS in system.

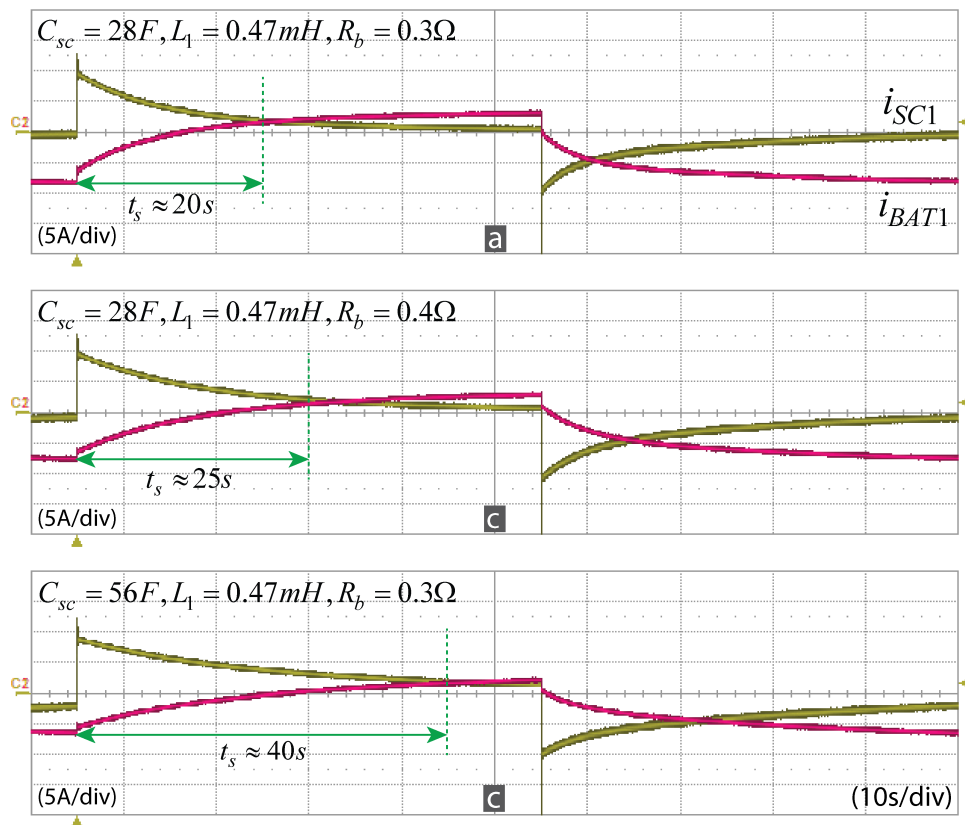


Figure 5.15: Case II: Impacts of SC capacity  $C_{sc}$  and battery internal resistance  $R_b$  on experimental results.

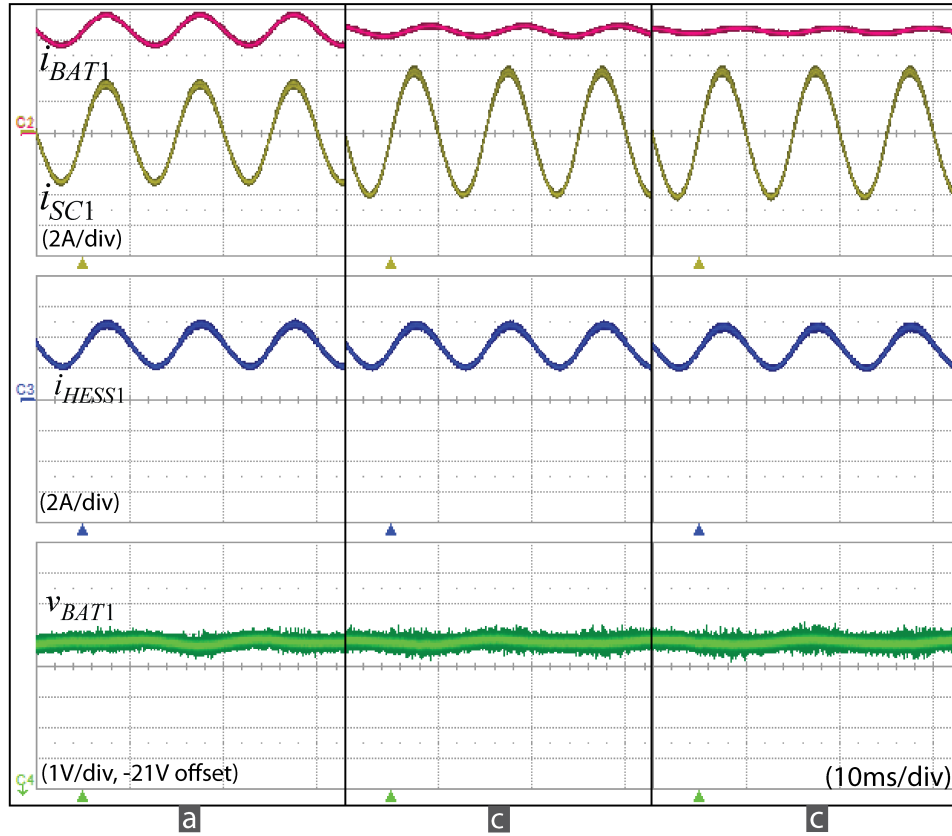


Figure 5.16: Case II: Impact of the inductance  $L_1$  on experimental results. (a) Without  $L_1$ , (b)  $L_1 = 0.47 \text{ mH}$ , (c)  $L_1 = 1.12 \text{ mH}$ .

Fig. 5.15(b) than in Fig. 5.15(a). The settling time is increased from 20 s to 25 s as the internal resistance is increased from  $0.3 \Omega$  to  $0.4 \Omega$ , which coincides with the calculation in (16). When the supercapacitor  $C_{sc}$  is increased from 28 F to 56 F, the settling time is increased from 20 s to 40 s, as shown in Fig. 5.15(c).

Under an unbalanced AC load of the inverter in a DC microgrid, harmonic and high-frequency current is generated on the DC bus. To evaluate the effectiveness of the BLSC-HESS configuration in a high frequency range, a harmonic current  $i_{DG1}$  of 100 Hz was injected into DC microgrid through the distributed generation converter. As a result, the output current  $i_{HESS1}$  fluctuated to regulate the DC bus. In Fig. 5.16, all three tested cases have the same amount of injection current. The inductance  $L_1$  was increased to investigate the effect on the BLSC-HESS. Fig. 5.16(a) shows the output currents of the supercapacitor and battery without inductor  $L_1$ . The supercapacitor cannot help to reduce the fluctuation in the output current  $i_{BAT1}$  of the battery. By adding an inductance of  $0.47 \mu\text{H}$ , the fluctuation of the battery current  $i_{BAT1}$  is reduced, as shown in Fig. 5.16(b). In Fig. 5.16(c), the fluctuation of the battery current  $i_{BAT1}$  is much

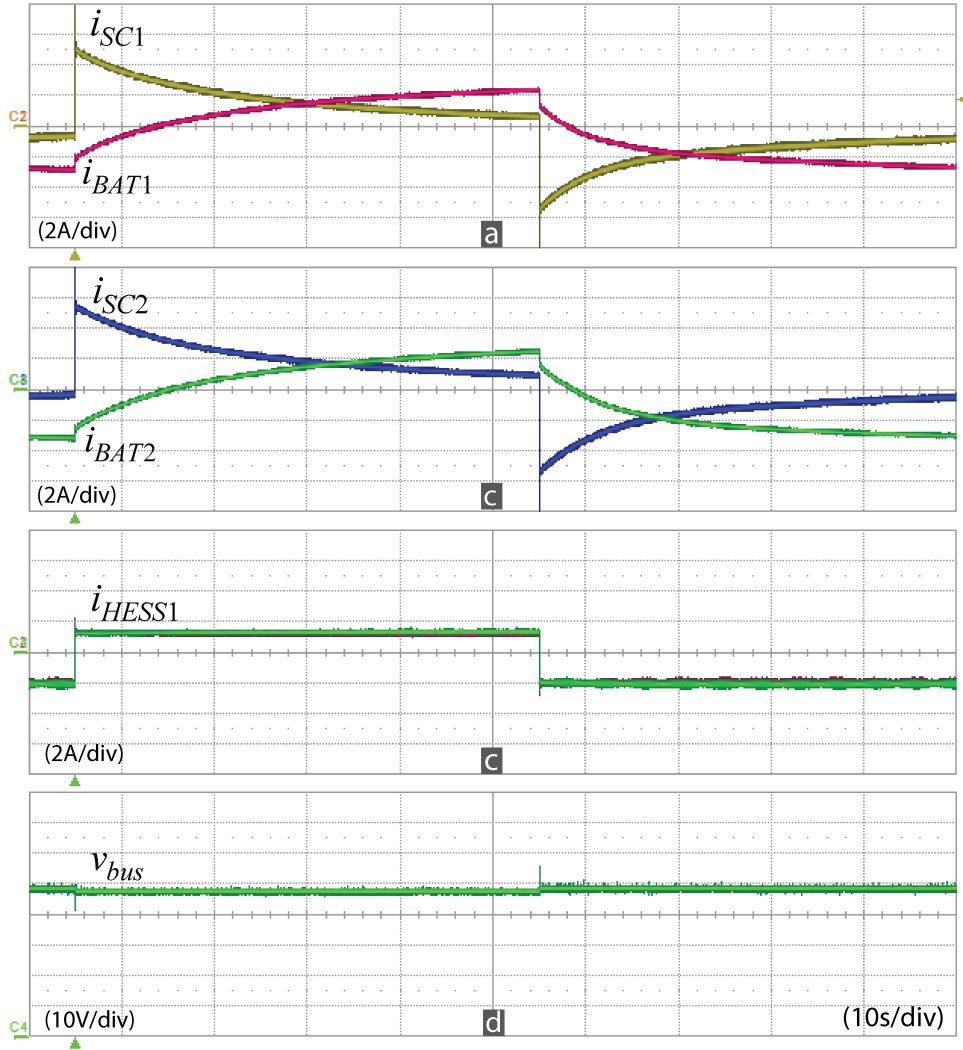


Figure 5.17: Case III: Experimental result of cooperation of two HESSs in the system.

smaller when the inductance is increased to  $1.12\text{ mH}$ . The results in Fig. 5.16 show that the battery current is smoothed by inserting the inductor.

Case III: HESS1 and HESS2 were used to observe the performance of the BLSC-HESS in parallel operation. Two HESSs are controlled by droop control to share the load power and regulate the DC bus voltage. The output currents of the battery and supercapacitor of the BLSC-HESSs are shown in Figs. 5.17(a) and (b) for HESS1 and HESS2. Because both HESSs have similar system parameters, the output currents of their batteries ( $i_{BAT1}$ ,  $i_{BAT2}$ ) and supercapacitors ( $i_{SC1}$ ,  $i_{SC2}$ ) are almost the same. Good sharing performance is shown by the matching of the HESS output currents  $i_{HESS1}$  and  $i_{HESS2}$  in Fig. 5.17(c). A stable DC bus voltage  $v_{bus}$  under load variation is shown in Fig. 5.17(d).

The experimental results show the effectiveness of the BLSC-HESS in smoothing the battery current with both low and high frequency currents. The results also prove the the-

oretical analysis and design guidelines. The simplicity of the configuration and controller make it easy to apply and practical.

## **5.5 Summary**

This chapter presented a simple BLSC-HESS configuration with reduced control complexity and cost. By inserting an inductor between the battery and supercapacitor, the demand current is effectively decoupled into low and high frequency current components. Therefore, the battery only handles the low-frequency current, while the supercapacitor handles the high-frequency current. The battery life is extended thanks to the reduced magnitude fluctuation of the battery current, and the lifetime of the supercapacitor is also increased because its voltage is ensured to be within a safe operating range. The proposed BLSC-HESS configuration is easily controlled by a conventional droop controller, so it can be directly applied to a DC microgrid with extendable capabilities and is easily adaptable to new or old systems. This study also offered a design process for the proposed BLSC-HESS, and the performance and effectiveness of the system were verified by a simulation and experimental results.

# Chapter 6

## Conclusions and Future Works

### 6.1 Conclusions

This thesis introduces power quality problems in DC microgrid by analyzing the effect of droop control, line impedance and load variation. It also proposed advanced control methods and configuration of the system to improve the power management and quality. The performance of proposed control method and configuration is validated under various load conditions and system parameters. From the achieved results by the proposed control methods and configuration, the main conclusions of this thesis are summarized as below:

- First, the DC bus voltage deviation, unbalanced power sharing, transient current, and pulsed load problems are investigated; and recent researches to overcome these problems are also reviewed. However, these recent researches still have some limitations in controlling and cost. Therefore, this thesis develops new control methods to improve power quality in DC microgrid such as better DC bus voltage regulation, balanced power sharing between DGs in microgrid, compensate the transient current for DGs and support the system under pulsed load.
- Distributed control is a suitable control architecture to overcome the voltage deviation and unbalanced power sharing problem in DC microgrid. Moreover, it only requires a low bandwidth communication interface to interact with other units in the system. A novel distributed control method is proposed based on voltage shift technique, it helps to compensate the voltage drop caused by droop control and achieve accurate proportional load power sharing. The design guideline and stability analysis is carried out to implement a reliable performance DC microgrid.
- The SC unit with a DC-DC converter is more flexible in controlling the sharing current between SC units and DG units. The previous control methods need additional control loop to restore the SC voltage in order to keep SC unit can operate

continuously. This thesis proposed an adaptive virtual impedance control method to seamlessly restore the SC voltage without an additional control loop. By actively adjusting the virtual impedance according to the SC voltage level, the proposed method smoothly restores the SC voltage at the same time with compensating the transient current. Based in virtual capacitance method, the SC units can operate in parallel to sharing the pulsed current; by recovering the SC voltage, the SC units in DC microgrid will always have same SC voltage level to maximize the availability of the system.

- By considering the pulsed load condition in the DC microgrid, this thesis proposed a droop based control method for the SC converter to compensate the transient normal load current as well as the pulsed load current together with the automatic SoC restoration. By using the droop control concept, the parallel operation of multi SC units is guaranteed, and the power sharing ratio is manipulated by the droop coefficient. A small signal model of SC converter is carried out in this thesis to properly design the SC controller for the proposed method. Moreover, the comparison with conventional virtual capacitance method shows the advantage of proposed control method under pulsed load condition.
- Compensating the transient current is importance when the DGs cannot quickly response to the load demand. An additional SC unit is integrated into DC microgrid to compensate the transient current in the system. This thesis presented a low-cost and compact configuration of HESS to compensate the transient current for the battery in a DC microgrid, it is called a battery-inductor-supercapacitor HESS (BLSC-HESS). It splits power between a battery and SC based on the frequency: the low frequency current is supplied by battery , while the high frequency current is supplied by the SC. A complete guidelines to design the parameters of the BLSC-HESS are also presented.

Finally, all the proposed control methods and configuration are verified by simulation and experimental results. The simulations are implemented by using PSIM software, and they all verified by using a DC microgrid prototype in laboratory, which is controlled by DSP from Texas Instruments. The parameters of experiments are provided in Appendix A together with experimental setup.

## **6.2 Future works**

The power quality problems in DC microgrid can be extended from study in this thesis, there are some possible problems that need to be consider in the future research. They can be suggested as:

- The fault protection in DC microgrid such as: short circuit protection, overload protection, fault override capability of DC-DC converter.
- Investigate the causes of circulating current between DGs in MC microgrid and solution to neglect the circulating current.
- Develop the Bipolar DC Distribution System and its related topics such as: bipolar dc-dc converter, voltage balancer, and power sharing.



# Bibliography

- [1] R Lasseter, A Akhil, C Marnay, J Stevens, J Dagle, R Guttromson, A S Meliopoulos, R Yinger, and J Eto, “White Paper on Integration of Distributed Energy Resources - The MicroGrid Concept”, *Consort. Electr. Reliab. Technol. Solut. April*, , no. October, pp. 1–27, 2002.
- [2] S.R. Bull, “Renewable energy today and tomorrow”, *Proc. IEEE*, vol. 89, no. 8, pp. 1216–1226, 2001.
- [3] Per Karlsson and Jörgen Svensson, “DC Bus Voltage Control for a Distributed Power System”, *IEEE Trans. Power Electron.*, vol. 18, no. 6, pp. 1405–1412, 2003.
- [4] M. Barnes, J. Kondoh, H. Asano, J. Oyarzabal, G. Ventakaramanan, R. Lasseter, N. Hatziargyriou, and T. Green, “Real-World MicroGrids-An Overview”, in *2007 IEEE Int. Conf. Syst. Syst. Eng.*, apr 2007, pp. 1–8.
- [5] Sandeep Anand and B. G. Fernandes, “Optimal voltage level for DC microgrids”, in *IECON Proc. (Industrial Electron. Conf.)*, 2010, pp. 3034–3039.
- [6] Hiroaki Kakigano, Yushi Miura, and Toshifumi Ise, “Low-voltage bipolar-type dc microgrid for super high quality distribution”, *IEEE Trans. Power Electron.*, vol. 25, no. 12, pp. 3066–3075, dec 2010.
- [7] Josep M. Guerrero, Juan C. Vasquez, José Matas, Luis García De Vicuña, and Miguel Castilla, “Hierarchical control of droop-controlled AC and DC microgrids - A general approach toward standardization”, *IEEE Trans. Ind. Electron.*, vol. 58, no. 1, pp. 158–172, 2011.
- [8] Tine L. Vandoorn, Bart Meersman, Lieven Degroote, Bert Renders, and Lieven Vandevelde, “A control strategy for islanded microgrids with DC-link voltage control”, *IEEE Trans. Power Deliv.*, vol. 26, no. 2, pp. 703–713, 2011.
- [9] B. K. Johnson, R. H. Lasseter, F. L. Alvarado, and R. Adapa, “Expandable Multi-terminal DC Systems Based on Voltage Droop”, *IEEE Trans. Power Deliv.*, vol. 8, no. 4, pp. 1926–1932, oct 1993.

- [10] Dong Chen and Lie Xu, “Autonomous DC voltage control of a DC microgrid with multiple slack terminals”, *IEEE Trans. Power Syst.*, vol. 27, no. 4, pp. 1897–1905, 2012.
- [11] Vahidreza Nasirian, Ali Davoudi, Frank L. Lewis, and Josep M. Guerrero, “Distributed adaptive droop control for DC distribution systems”, *IEEE Trans. Energy Convers.*, vol. 29, no. 4, pp. 944–956, dec 2014.
- [12] Amir Khorsandi, Mojtaba Ashourloo, and Hossein Mokhtari, “A decentralized control method for a low-voltage dc microgrid”, *IEEE Trans. Energy Convers.*, vol. 29, no. 4, pp. 793–801, 2014.
- [13] Yunjie Gu, Xin Xiang, Wuhua Li, and Xiangning He, “Mode-Adaptive Decentralized Control for Renewable DC Microgrid With Enhanced Reliability and Flexibility”, *IEEE Trans. Power Electron.*, vol. 29, no. 9, pp. 5072–5080, 2014.
- [14] Fang Chen, Rolando Burgos, Dushan Boroyevich, and Wei Zhang, “A nonlinear droop method to improve voltage regulation and load sharing in DC systems”, in *2015 IEEE 1st Int. Conf. Direct Curr. Microgrids, ICDCM 2015*, 2015, pp. 45–50.
- [15] Reza Iravani, Amir Khorsandi, Mojtaba Ashourloo, and Hossein Mokhtari, “Automatic droop control for a low voltage DC microgrid”, *IET Gener. Transm. Distrib.*, vol. 10, no. 1, pp. 41–47, 2016.
- [16] Hiroaki Kakigano, Yushi Miura, and Toshifumi Ise, “Distribution voltage control for DC microgrids using fuzzy control and gain-scheduling technique”, *IEEE Trans. Power Electron.*, vol. 28, no. 5, pp. 2246–2258, may 2013.
- [17] Ali Maknouninejad, Zhihua Qu, Frank L. Lewis, and Ali Davoudi, “Optimal, non-linear, and distributed designs of droop controls for DC microgrids”, *IEEE Trans. Smart Grid*, vol. 5, no. 5, pp. 2508–2516, 2014.
- [18] Lexuan Meng, Tomislav Dragicevic, Juan C. Vasquez, and Josep M. Guerrero, “Tertiary and Secondary Control Levels for Efficiency Optimization and System Damping in Droop Controlled DC-DC Converters”, *IEEE Trans. Smart Grid*, vol. 6, no. 6, pp. 2615–2626, nov 2015.
- [19] L. Meng Guerrero, T. Dragicevic, J. Roldán-Pérez, J. C. Vasquez, and J. M., “Modeling and Sensitivity Study of Consensus Algorithm-Based Distributed Hierarchical Control for DC Microgrids”, *IEEE Trans. Smart Grid*, vol. 7, no. 3, pp. 1504–1515, may 2016.

- [20] Daniel Salomonsson, Lennart Soder, and Ambra Sannino, “An adaptive control system for a DC microgrid for data centers”, *IEEE Trans. Ind. Appl.*, vol. 44, no. 6, pp. 1910–1917, 2008.
- [21] Xiaonan Lu, Josep M. Guerrero, Kai Sun, and Juan C. Vasquez, “An improved droop control method for dc microgrids based on low bandwidth communication with dc bus voltage restoration and enhanced current sharing accuracy”, *IEEE Trans. Power Electron.*, vol. 29, no. 4, pp. 1800–1812, 2014.
- [22] Tomislav Dragičević, Josep M. Guerrero, and Juan C. Vasquez, “A distributed control strategy for coordination of an autonomous LVDC microgrid based on power-line signaling”, *IEEE Trans. Ind. Electron.*, vol. 61, no. 7, pp. 3313–3326, jul 2014.
- [23] Chi Jin, Peng Wang, Jianfang Xiao, Yi Tang, and Fook Hoong Choo, “Implementation of hierarchical control in DC microgrids”, *IEEE Trans. Ind. Electron.*, vol. 61, no. 8, pp. 4032–4042, aug 2014.
- [24] Kai Sun, Li Zhang, Yan Xing, and Josep M. Guerrero, “A distributed control strategy based on DC bus signaling for modular photovoltaic generation systems with battery energy storage”, *IEEE Trans. Power Electron.*, vol. 26, no. 10, pp. 3032–3045, oct 2011.
- [25] Sandeep Anand, Baylon G. Fernandes, and Josep M. Guerrero, “Distributed control to ensure proportional load sharing and improve voltage regulation in low-voltage DC microgrids”, *IEEE Trans. Power Electron.*, vol. 28, no. 4, pp. 1900–1913, 2013.
- [26] Qobad Shafiee, Tomislav Dragičević, Juan C. Vasquez, and Josep M. Guerrero, “Hierarchical control for multiple DC-microgrids clusters”, *IEEE Trans. Energy Convers.*, vol. 29, no. 4, pp. 922–933, dec 2014.
- [27] T A Smith, J P Mars, and G A Turner, “Using supercapacitors to improve battery performance”, in *2002 IEEE 33rd Annu. IEEE Power Electron. Spec. Conf. Proc. (Cat. No.02CH37289)*, 2002, vol. 1, pp. 124–128 vol.1.
- [28] Wei Li and Géza Joós, “A power electronic interface for a battery supercapacitor hybrid energy storage system for wind applications”, in *PESC Rec. - IEEE Annu. Power Electron. Spec. Conf.*, jun 2008, pp. 1762–1768.
- [29] Peng Wang, Jianfang Xiao, and Leonary Setyawan, “Hierarchical Control of Hybrid Energy Storage System in DC Microgrids”, *IEEE Trans. Ind. Electron.*, vol. PP, no. 99, pp. 1–1, 2015.

- [30] Po Hsu Huang, Po Chun Liu, Weidong Xiao, and Mohamed Shawky El Moursi, “A Novel Droop-Based Average Voltage Sharing Control Strategy for DC Microgrids”, *IEEE Trans. Smart Grid*, vol. 6, no. 3, pp. 1096–1106, 2015.
- [31] Ahmed Mohamed, Vahid Salehi, and Osama Mohammed, “Real-Time Energy Management Algorithm for Mitigation of Pulse Loads in Hybrid Microgrids”, *IEEE Trans. Smart Grid*, vol. 3, no. 4, pp. 1911–1922, dec 2012.
- [32] Jingdong Li, Yang Liu, Shu Wang, Jing Shi, Li Ren, Kang Gong, and Yuejin Tang, “Design and advanced control strategies of a hybrid energy storage system for the grid integration of wind power generations”, *IET Renew. Power Gener.*, vol. 9, no. 2, pp. 89–98, 2015.
- [33] Narsa Reddy Tummuru, Mahesh K. Mishra, and S. Srinivas, “Dynamic Energy Management of Renewable Grid Integrated Hybrid Energy Storage System”, *IEEE Trans. Ind. Electron.*, vol. 62, no. 12, pp. 7728–7737, dec 2015.
- [34] Xin Zhao, Xuezhi Wu, Yunwei Wei Li, Hao Tian, Xin Zhao, Yunwei Wei Li, Hao Tian, and Xuezhi Wu, “Energy Management Strategy of Multiple Supercapacitors in a DC Microgrid Using Adaptive Virtual Impedance”, *IEEE J. Emerg. Sel. Top. Power Electron.*, vol. 4, no. 4, pp. 1–8, 2016.
- [35] Yuru Zhang and Yunwei Li, “Energy management strategy for supercapacitor in autonomous DC microgrid using virtual impedance”, in *IEEE Appl. Power Electron. Conf. Expo.*, 2015, pp. 725–730.
- [36] Yuru Zhang, Yun Wei Li, and Y W Li, “Energy management strategy for supercapacitor in droop-controlled dc microgrid using virtual impedance”, *IEEE Trans. Power Electron.*, vol. 32, no. 99, pp. 1, apr 2017.
- [37] Yunjie Gu, Wuhua Li, and Xiangning He, “Frequency-Coordinating Virtual Impedance for Autonomous Power Management of DC Microgrid”, *IEEE Trans. Power Electron.*, vol. 30, no. 4, pp. 2328–2337, apr 2015.
- [38] Mohsen Hamzeh, Mohsen Ghafouri, Houshang Karimi, Keyhan Sheshyekani, and Josep M. Guerrero, “Power Oscillations Damping in DC Microgrids”, *IEEE Trans. Energy Convers.*, vol. 31, no. 3, pp. 970–980, sep 2016.
- [39] K Bi, L Sun, Q An, and J Duan, “Active SOC Balancing Control Strategy for Modular Multilevel Super Capacitor Energy Storage System”, *IEEE Trans. Power Electron.*, p. 1, 2018.

- [40] Vladimir Yuhimenko, Chaim Lerman, and Alon Kuperman, “DC Active Power Filter-Based Hybrid Energy Source for Pulsed Power Loads”, *IEEE J. Emerg. Sel. Top. Power Electron.*, vol. 3, no. 4, pp. 1001–1010, 2015.
- [41] M. Milad Hoseini Ahmadi, Salman Haji Aghasi, and Ahmad Salemnia, “Hybrid Energy Storage for DC Microgrid Performance Improvement Under Nonlinear and Pulsed Load Conditions”, in *2018 Smart Grid Conf.* nov 2018, pp. 1–6, IEEE.
- [42] Duy-Hung Dam and Hong-Hee Lee, “An adaptive power distributed control method to ensure proportional load power sharing in DC microgrid considering equivalent line impedances”, *ECCE 2016 - IEEE Energy Convers. Congr. Expo. Proc.*, pp. 1–6, sep 2016.
- [43] J. M. Crider and S. D. Sudhoff, “Reducing impact of pulsed power loads on microgrid power systems”, *IEEE Transactions on Smart Grid*, vol. 1, no. 3, pp. 270–277, Dec 2010.
- [44] Mustafa Farhadi and Osama A. Mohammed, “Performance Enhancement of Actively Controlled Hybrid DC Microgrid Incorporating Pulsed Load”, *IEEE Trans. Ind. Appl.*, vol. 51, no. 5, pp. 3570–3578, 2015.
- [45] T Ma, M H Cintuglu, and O A Mohammed, “Control of a Hybrid AC/DC Microgrid Involving Energy Storage and Pulsed Loads”, *IEEE Trans. Ind. Appl.*, vol. 53, no. 1, pp. 567–575, jan 2017.
- [46] M. M. Mardani, M. H. Khooban, A. Masoudian, and T. Dragičević, “Model predictive control of dc–dc converters to mitigate the effects of pulsed power loads in naval dc microgrids”, *IEEE Transactions on Industrial Electronics*, vol. 66, no. 7, pp. 5676–5685, July 2019.
- [47] D Dam, S Choi, and H Lee, “A Droop Based Controller for Super-Capacitor to Compensate the Transient Current and Pulsed Load in DC Microgrid”, in *2018 IEEE Energy Convers. Congr. Expo.*, 2018, pp. 4771–4775.
- [48] Liping Guo, John Y. Hung, and R. M. Nelms, “Evaluation of DSP-based PID and fuzzy controllers for DC-DC converters”, *IEEE Trans. Ind. Electron.*, 2009.
- [49] Alexis Kwasinski and Chimaobi N. Onwuchekwa, “Dynamic behavior and stabilization of DC microgrids with instantaneous constant-power loads”, *IEEE Trans. Power Electron.*, vol. 26, no. 3, pp. 822–834, 2011.

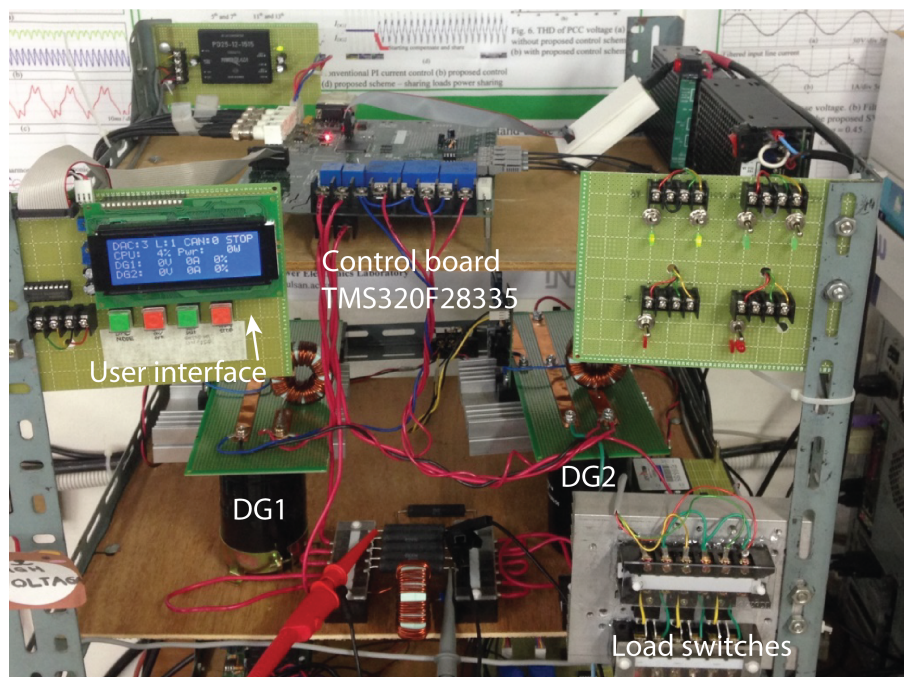
- [50] Nelson L. Diaz, Tomislav Dragicevic, Juan C. Vasquez, and Josep M. Guerrero, “Intelligent distributed generation and storage units for DC microgrids - A new concept on cooperative control without communications beyond droop control”, *IEEE Trans. Smart Grid*, vol. 5, no. 5, pp. 2476–2485, sep 2014.
- [51] John Schönberger, Richard Duke, and Simon D. Round, “DC-bus signaling: A distributed control strategy for a hybrid renewable nanogrid”, *IEEE Trans. Ind. Electron.*, 2006.
- [52] Gilsung Byeon, Taeyoung Yoon, Seaseung Oh, and Gilsoo Jang, “Energy management strategy of the DC distribution system in buildings using the EV service model”, *IEEE Trans. Power Electron.*, 2013.
- [53] Liang Che and Mohammad Shahidehpour, “DC microgrids: Economic operation and enhancement of resilience by hierarchical control”, *IEEE Trans. Smart Grid*, 2014.
- [54] Vahidreza Nasirian, Seyedali Moayedi, Ali Davoudi, and Frank L. Lewis, “Distributed cooperative control of dc microgrids”, *IEEE Trans. Power Electron.*, vol. 30, no. 4, pp. 2288–2303, apr 2015.
- [55] Ali Bidram, Ali Davoudi, Frank L. Lewis, and Zhihua Qu, “Secondary control of microgrids based on distributed cooperative control of multi-agent systems”, *IET Gener. Transm. Distrib.*, 2013.
- [56] Lexuan Meng, Tomislav Dragicevic, Josep M. Guerrero, and Juan C. Vasquez, “Dynamic consensus algorithm based distributed global efficiency optimization of a droop controlled DC microgrid”, in *ENERGYCON 2014 - IEEE Int. Energy Conf.*, 2014.
- [57] “Ieee recommended practice for 1 kv to 35 kv medium-voltage dc power systems on ships”, *IEEE Std 1709-2010*, pp. 1–54, Nov 2010.
- [58] F A Inthamoussou, J Pegueroles-Queralt, and F D Bianchi, “Control of a Supercapacitor Energy Storage System for Microgrid Applications”, *IEEE Trans. Energy Convers.*, vol. 28, no. 3, pp. 690–697, sep 2013.
- [59] Qianwen Xu, Xiaolei Hu, Peng Wang, Jianfang Xiao, Pengfei Tu, Changyun Wen, Meng Yeong Lee, and Lee Meng Yeong, “A Decentralized Dynamic Power Sharing Strategy for Hybrid Energy Storage System in Autonomous DC Microgrid”, *IEEE Trans. Ind. Electron.*, vol. 64, no. 99, pp. 1, jul 2016.

- [60] Sathish Kumar Kollimalla, Mahesh Kumar Mishra, and N. Lakshmi Narasamma, “Design and Analysis of Novel Control Strategy for Battery and Supercapacitor Storage System”, *IEEE Trans. Sustain. Energy*, vol. 5, no. 4, pp. 1137–1144, oct 2014.
- [61] Sathish Kumar Kollimalla, Mahesh K. Mishra, Abhisek Ukil, and Hoay Beng Gooi, “DC Grid Voltage Regulation Using New HESS Control Strategy”, 2016.
- [62] Robert David Middlebrook, “Input filter design considerations in design and applications of switching regulators”, in *Ieee Ias*, oct 1976, pp. 366–382.
- [63] Amir M. Rahimi and Ali Emadi, “Active damping in DC/DC power electronic converters: A novel method to overcome the problems of constant power loads”, *IEEE Trans. Ind. Electron.*, vol. 56, no. 5, pp. 1428–1439, 2009.
- [64] Valentin A. Boicea, “Energy Storage Technologies: The Past and the Present”, *Proc. IEEE*, vol. 102, no. 11, pp. 1777–1794, nov 2014.
- [65] R A Dougal, S Liu, and R E White, “Power and life extension of battery-ultracapacitor hybrids”, *IEEE Trans. Components Packag. Technol.*, vol. 25, no. 1, pp. 120–131, mar 2002.
- [66] Yuan Chuan Liu and Yaow Ming Chen, “A systematic approach to synthesizing multi-input DC-DC converters”, *IEEE Trans. Power Electron.*, vol. 24, no. 1, pp. 116–127, jan 2009.
- [67] Hamid Behjati and Ali Davoudi, “A multiple-input multiple-output DC-DC converter”, *IEEE Trans. Ind. Appl.*, vol. 49, no. 3, pp. 1464–1479, may 2013.
- [68] Andrew Hintz, Udupi R. Prasanna, and Kaushik Rajashekara, “Novel Modular Multiple-Input Bidirectional DC-DC Power Converter (MIPC) for HEV/FCV Application”, *IEEE Trans. Ind. Electron.*, vol. 62, no. 5, pp. 3163–3172, may 2015.
- [69] Qianwen Xu, Jianfang Xiao, Xiaolei Hu, Peng Wang, and Meng Yeong Lee, “A Decentralized Power Management Strategy for Hybrid Energy Storage System with Autonomous Bus Voltage Restoration and State of Charge Recovery”, *IEEE Trans. Ind. Electron.*, vol. 0046, no. 9, pp. 7098–7108, sep 2017.
- [70] Jean Paul Cun, Jean Noel Fiorina, Michel Fraisse, and Henri Mabboux, “Experience of a UPS company in advanced battery monitoring”, in *INTELEC, Int. Telecommun. Energy Conf.*, 1996.

- [71] H. L. Chan and D. Sutanto, “A new battery model for use with battery energy storage systems and electric vehicles power systems”, in *2000 IEEE Power Eng. Soc. Conf. Proc.*, 2000.
- [72] Min Chen and Gabriel A. Rincón-Mora, “Accurate electrical battery model capable of predicting runtime and I-V performance”, *IEEE Trans. Energy Convers.*, 2006.
- [73] Stephan Buller, Marc Thele, Rik W A A De Doncker, and Eckhard Karden, “Impedance-based simulation models of supercapacitors and li-ion batteries for power electronic applications”, *IEEE Trans. Ind. Appl.*, 2005.
- [74] Hongwen He, Rui Xiong, Xiaowei Zhang, Fengchun Sun, and Jinxin Fan, “State-of-charge estimation of the lithium-ion battery using an adaptive extended Kalman filter based on an improved Thevenin model”, *IEEE Trans. Veh. Technol.*, 2011.
- [75] Min Chen, G A Rincon-Mora, and Gabriel A. Rincón-Mora, “Accurate electrical battery model capable of predicting runtime and I-V performance”, *IEEE Trans. Energy Convers.*, vol. 21, no. 2, pp. 504–511, jun 2006.
- [76] Junyi Shen and Alireza Khaligh, “A Supervisory Energy Management Control Strategy in a Battery/Ultracapacitor Hybrid Energy Storage System”, *IEEE Trans. Transp. Electrif.*, vol. 1, no. 3, pp. 223–231, oct 2015.

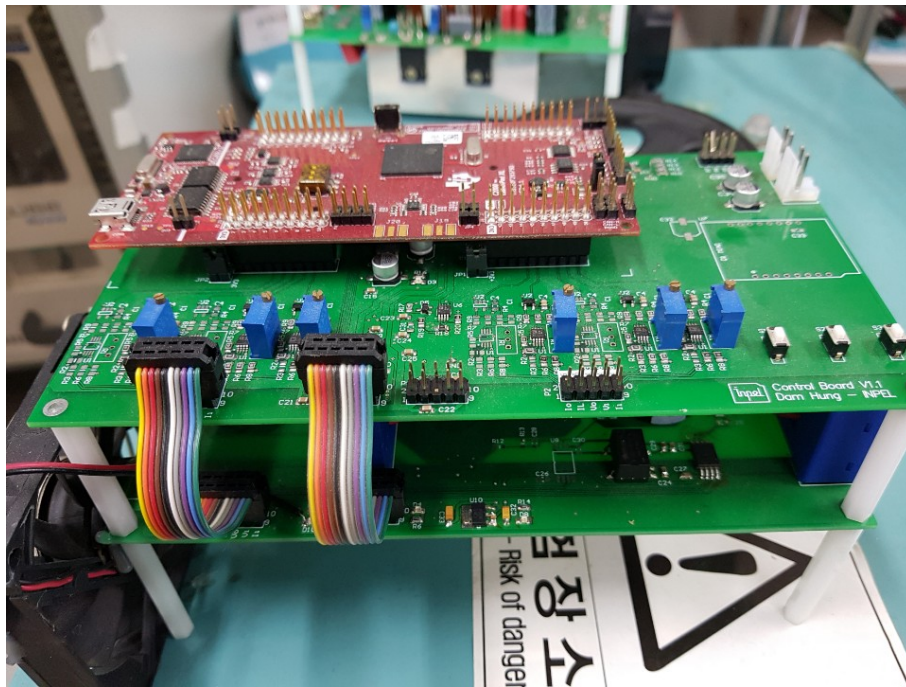


## Appendix A - Experimental Setup

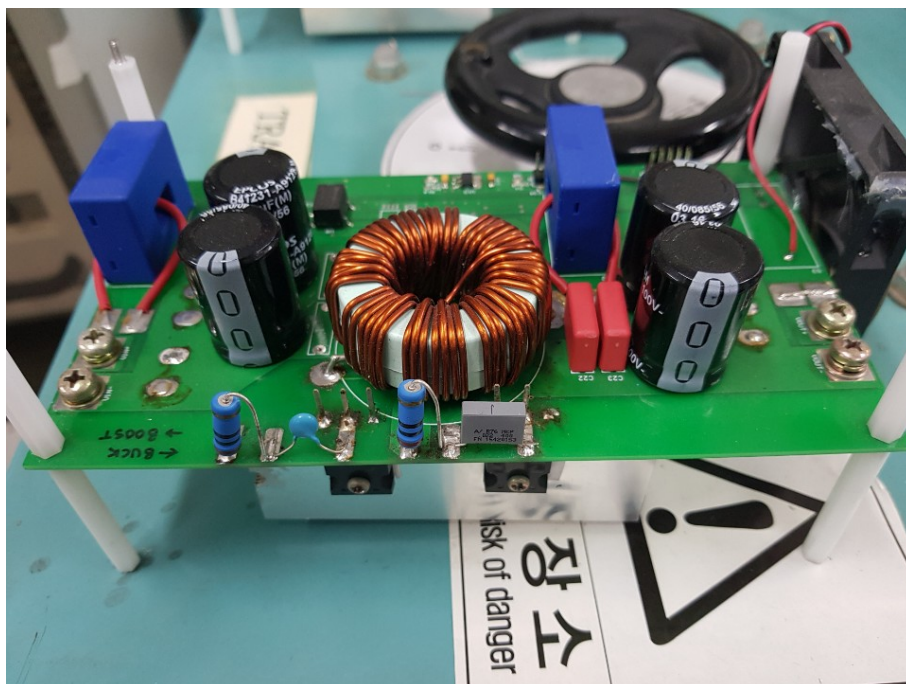


Experimental setup of 2.7kW DC microgrid test-bed

Parameters	Value
Microcontroller	TMS320F28335
Input/output voltage	300/200V
Input/output capacitor	2200 $\mu$ F
Inductor	0.5mH
Switching frequency	20kHz
Sampling frequency	10kHz
Rated current	10A
Loads	10, 30 $\Omega$



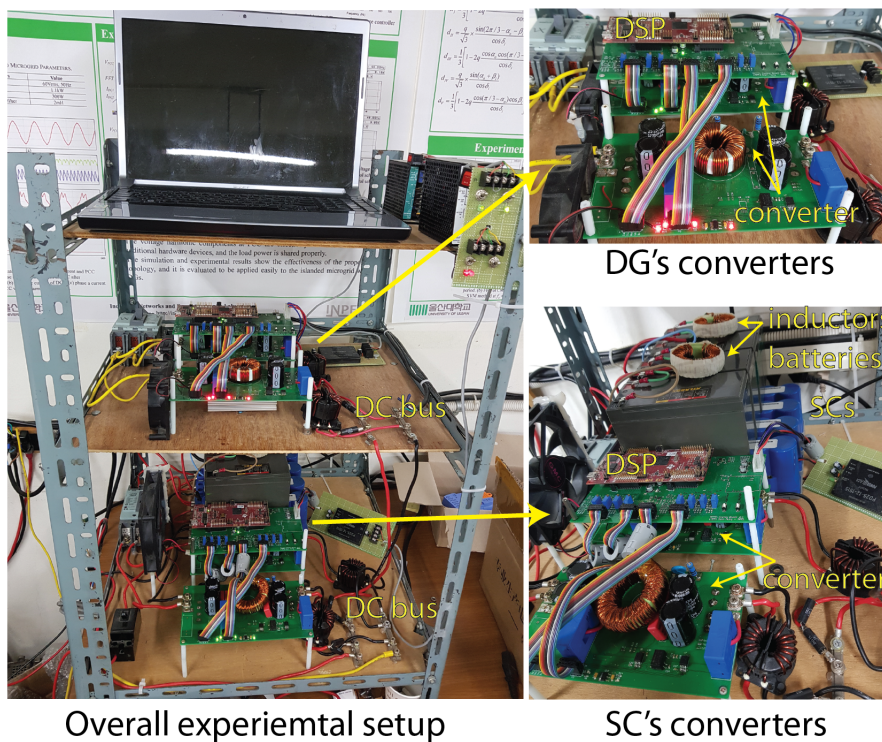
DC-DC converter for SC units - DSP control board.



DC-DC converter for SC units - Converter board.

Appendix A - Experimental Setup

Parameters	Value
Microcontroller	TMS320F28379D
Input/output voltage	24/48V
Input/output capacitor	2200 $\mu$ F
Inductor	0.5mH
Switching frequency	20kHz
Sampling frequency	10kHz
Rated current	10A
Loads	5, 10 $\Omega$





# Appendix B - Publications

## Journal Articles

1. Dam Duy-Hung, Lee Hong-Hee: 'Effective Voltage Quality Control under Nonlinear Loads in Islanded Microgrid' *Korean Inst. Power Electron.*, 2016, 21, (6), pp. 465–472.
2. Dam Duy-Hung, Lee Hong-Hee: 'A Seamless Control Method for Supercapacitor to Compensate Pulsed Load in DC Microgrid' *Korean Inst. Power Electron.*, 2018, 23, (4), pp. 265–272.
3. Dam Duy-Hung, Lee Hong-Hee: 'A Power Distributed Control Method for Proportional Load Power Sharing and Bus Voltage Restoration in a DC Microgrid' *IEEE Trans. Ind. Appl.*, 2018, pp. 1–1.
4. Dam Duy-Hung, Lee Hong-Hee: 'A Battery-Inductor-Supercapacitor Hybrid Energy Storage System for DC Microgrids' *Journal of Power Electronics*, (Be public in Jan. 2020).

## Conferences

1. D. Dam, S. Choi and H. Lee, "A Droop Based Controller for Super-Capacitor to Compensate the Transient Current and Pulsed Load in DC Microgrid," *2018 IEEE Energy Conversion Congress and Exposition (ECCE)*, Portland, OR, 2018, pp. 4771-4775. doi: 10.1109/ECCE.2018.8557749
2. D. Dam, D. Hoang, T. Chun and H. Lee, "A hybrid energy storage system for transient load and its multiple operation in DC microgrid," *2018 IEEE International Conference on Industrial Electronics for Sustainable Energy Systems (IESES)*, Hamilton, 2018, pp. 314-319. doi: 10.1109/IESES.2018.8349895
3. D. Dam and H. Lee, "An adaptive power distributed control method to ensure proportional load power sharing in DC microgrid considering equivalent line impedances,"

*2016 IEEE Energy Conversion Congress and Exposition (ECCE)*, Milwaukee, WI, 2016, pp. 1-6. doi: 10.1109/ECCE.2016.7854837

4. Duy-Hung Dam, Hong-Hee Lee and Heung-Geun Kim, "Effective output voltage quality control under nonlinear loads in islanded microgrid," *2015 IEEE 2nd International Future Energy Electronics Conference (IFEEEC)*, Taipei, 2015, pp. 1-6. doi: 10.1109/IFEEEC.2015.7361497